PHOTOPRODUCTION OF THE $D^{*\pm}$

BY

PAUL RALPH AVERY

B.S., Canisius College, 1973
M.S., University of Illinois, 1975

THESIS

Submitted in partial fulfillment of the requirements
for the degree of Doctor of Philosophy in Physics
in the Graduate College of the
University of Illinois at Urbana-Champaign, 1980

Urbana, Illinois

PHOTOPRODUCTION OF THE $D^{*\pm}$

Paul Ralph Avery, Ph.D
Department of Physics
University of Illinois at Urbana-Champaign, 1980

Using the broad band beam at FNAL, we have observed the photoproduction of the D^{*+} (and D^{*-}) meson, where $D^{*+} \rightarrow D^0\pi^+$ and $D^0 \rightarrow K^-\pi^+$ (143 ± 20 events) or $D^0 \rightarrow K_s\pi^+\pi^-$ (35 ± 11 events). The observation exploited the small D^{*+}-D^0 mass difference to reduce the combinatoric background by 3 orders of magnitude. A variety of analysis techniques are presented to demonstrate that the D^{*+} is created by a diffractive pair production mechanism, with a cross section given by

$$\sigma(\gamma + N \rightarrow D^0\ ) = 160 \pm 70 \text{ nb/nucleon}$$

Finally we discuss the data in terms of a QCD production mechanism, photon gluon fusion, and attempt to fix certain parameters in the theory by using the D^* P_t distribution.

ACKNOWLEDGEMENTS

It gives me great pleasure to publicly acknowledge the efforts of the people who helped me during my graduate career at Illinois.

Much of the success of experiment 87A reflects in no small way on the Accelerator Division personnel, who have made Fermilab one of the leading High Energy physics laboratories in the world. I also want to thank the people in the Proton Department for maintaining the neutral beam and providing the technical support necessary to successfully run our experiment.

Additional technical expertise was provided by Ken Gray of Columbia and Leonard Seward of Illinois. I am especially grateful to Lenny both for the practical information he passed on to me and for the many enjoyable trips I made with him to Fermilab. Lenny's sense of humor and great reservoir of stories always seemed to make the time go faster.

It has long been a fact that most of the work in High Energy physics requires the extensive use of sophisticated computers. I have been particularly fortunate to have had access to excellent computer facilities at Fermilab and at the University of Illinois. The staffs of the Fermilab Computing Department and the University of Illinois Computing Services Office are to be commended for maintaining their respective CYBER 175's, which enabled the analysis for our experiment to be completed in a reasonable amount of time. My most heartfelt thanks, however, go to the staff of the High Energy Physics DEC-10 facility at Illinois. Thanks to the efforts of Dick Brown and Jerry Wray, the informal "open shop" policy has made computing here a very productive - yet enjoyable - experience. I am also indebted to Jerry, Keith Nater, and Dave Lesny for their time spent answering my questions on software and programming .

I owe a special debt of thanks to my fellow collaborators on experiment

87A: Joel Butler, Gary Gladding, Maury Goodman, Tom O'Halloran, Jim Russell, Al Wattenberg, Jim Wiss, Morris Binkley, John Cumalat, Irwin Gaines, Mike Gormley, Bob Loveless, John Peoples, Maged Atiya, Steve Holmes, Bruce Knapp, Wonyong Lee, and Bill Wisniewski. Wonyong Lee deserves special praise for his foresight and work in making charm photoproduction a reality.

Several people at Illinois helped me a great deal during the course of the experiment and subsequent analysis. I am thankful to Al Wattenberg for taking his time to teach me some of the tricks of the trade. Jim Russell and Maury Goodman collaborated closely with me during many phases of the analysis, and I owe them both a debt of gratitude for their timely help and gracious hospitality. I also wish to thank Tom O'Halloran for his advice during the analysis.

Much of the work on the Photon Gluon Fusion model is a result of long discussions with Lorella Jones, whose ready accessibility should be a model for experimentalist - theorist relationships.

I want to thank the secretaries in the High Energy Physics office - particularly Dorothy Schoeps - for their timely help in arranging transportation and housing for my many trips to Fermilab.

I am very pleased to have had Gary Gladding as my advisor. My development as a physicist is a result of his careful tutelage and eye for exactness. The wide range of problems I worked on under his guidance provided me with the experience neccessary to carry out the analysis performed in this thesis.

I have been extremely fortunate to have worked on the E-87A analysis in collaboration with Jim Wiss. Certainly much of the work presented in this thesis would not have been possible without Jim's exceptional insight, and I am grateful for the opportunity to have worked closely with him. I also wish

to thank him for carefully reading this manuscript as well as for making numerous suggestions to improve its readability.

A special vote of thanks goes to the D*-D mass difference for being just the right size to enable the observation of the D* signal. To paraphrase Chico Esquela, "D*-D mass difference be verry, verry, good to me".

Finally, I want to dedicate this thesis to my wife, Linda, for the love and support she gave me during the long and sometimes difficult graduate student years. The words, "No man is an island, entire of itself", were never more truly spoken.

This research was supported in part by the U.S. Department of Energy under Contract DE-AC02-76ER01195.

TABLE OF CONTENTS

1. INTRODUCTION AND THEORY..... 1

2. THE DETECTOR..... 11

Section A. The Neutral Beam..... 11
Section B. The Detector..... 14
Section C. The Trigger..... 26
Section D. Data Acquisition System..... 38

3. ANALYSIS TECHNIQUES..... 42

Section A. Data Reduction..... 42
Section B. Track Reconstruction..... 43
Section C. Edit Analysis..... 44
Section D. Cerenkov Identification..... 52
Section E. Analysis Programs..... 53

4. DETECTOR PERFORMANCE..... 59

Section A. Cerenkov Identification..... 59
Section B. Trigger Study..... 73

5. MONTE CARLO..... 83

6. THE D* SIGNAL..... 85

Section A. Observation of Signal..... 85
Section B. D^0-$\bar{D}^0$ Mixing..... 91
Section C. How is the D* Produced?..... 94
Section D. Cross Section..... 111
Section E. Inclusive D^0 Signal..... 118

7. MODEL DEPENDENCE..... 121

Section A. The Photon Gluon Fusion Model..... 121
Section B. Comparison with P_t Distribution..... 128
Section C. Comparison with Other Distributions..... 137
Section D. Total Photoproduced Charm Cross Section..... 147

8. SUMMARY AND CONCLUSIONS..... 150

REFERENCES..... 158

VITA..... 161

CHAPTER 1

INTRODUCTION AND THEORY

The existence of a fourth quark carrying a new quantum number was postulated in the early 1960's {1} as a means of achieving some sort of lepton hadron symmetry. At the time, this hypothesis represented a straightforward extension of the SU(3) quark model which had already been proven remarkably successful in elucidating meson and baryon spectroscopy. However the 3 quark theory ran into serious difficulties within the context of the Weinberg-Salam (W-S) gauge theory of the weak and electromagnetic interactions. A bold prediction of this theory, and one that was verified in 1973 {2}, was the existence of weak neutral currents which mediate processes such as $\nu P \rightarrow \nu + X$. Unfortunately the W-S model, in its 3 quark formulation, also predicted strangeness changing neutral currents, in contradiction to the experimentally determined small upper limits on such processes, particularly $K_L \rightarrow \mu^+\mu^-$. The addition of a fourth "charmed" quark in the manner proposed by Glashow, Illiopoulos, and Maiani (GIM) {3} not only removes this anamolous current but leads to a neutral current that is flavor conserving.

The most striking prediction of the charmed quark model is of course the existence of a rich new spectroscopy containing hadrons of non-zero charm as well as $c\bar{c}$ states (see Table 1.1). This spectroscopy has been spectacularly confirmed in recent years. Two groups working independently at SPEAR {4} and BNL {5} reported in 1974 the existence of a narrow resonance at 3.095 GeV coupled electromagnetically to leptons. Strong evidence mounted over the next few months to identify this particle, the $\psi(3095)$, as a vector meson containing a $c\bar{c}$ quark pair. Later searches at SPEAR revealed a whole spectrum of these so-called "charmonium" states. Some of these, e.g. the

CHARM SPECTROSCOPY

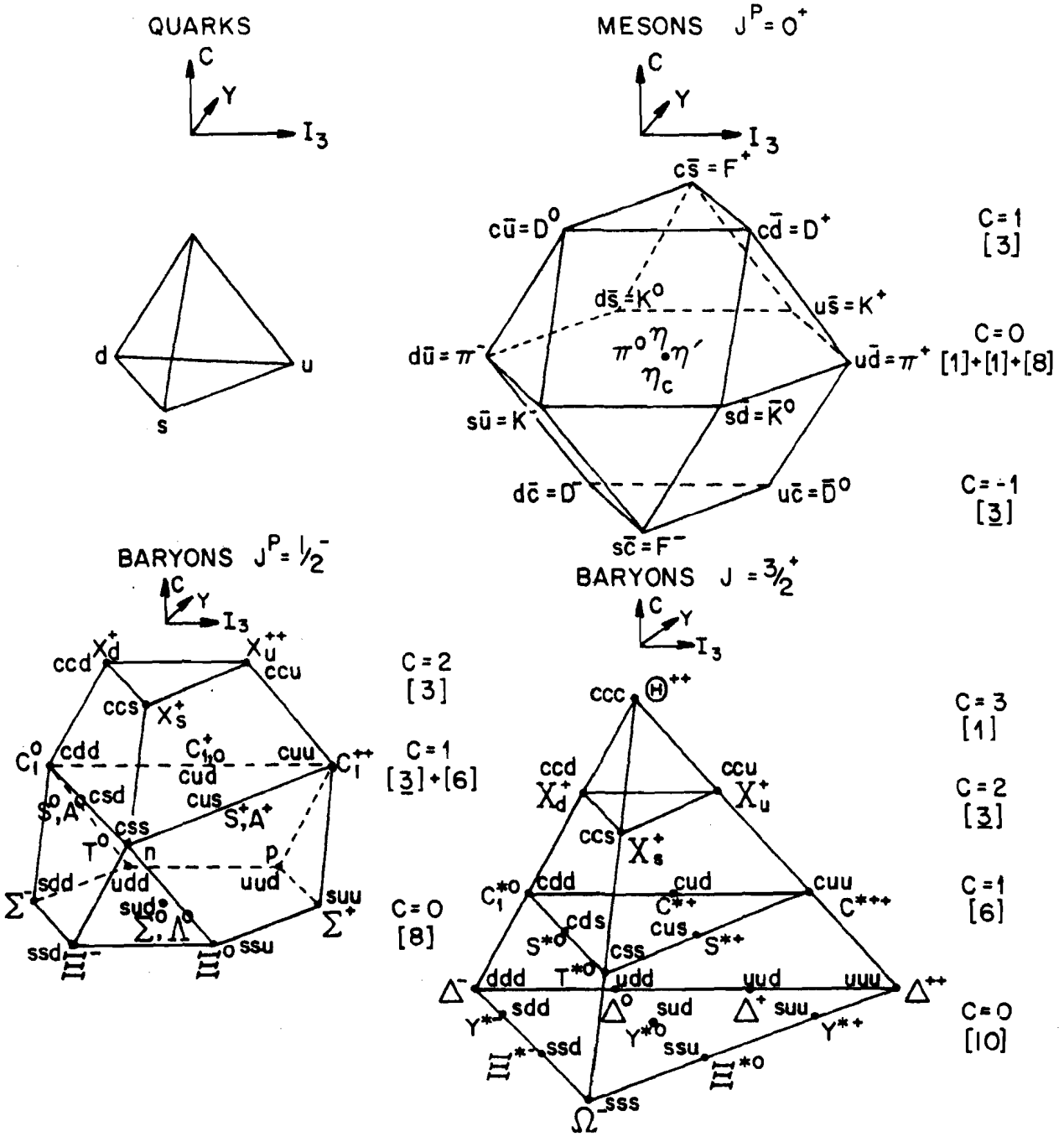

Table 1.1

$\psi(3685)$, $\psi(3770)$, and $\psi(4415)$, were found to be $J^{PC}=1^{--}$ states like the $\psi(3095)$, whereas the $\chi(3415)$, $\chi(3508)$, and $\chi(3555)$ have been identified with the J=0,1,2 members of the ^3P_J series.

Impressive as this evidence might seem, it did not constitute a crucial test of the GIM mechanism because none of the above particles carry non-zero charm or decay weakly. However in 1976 the isodoublet D mesons were discovered through the decays $D^0 \to K^-\pi^+$, $K^-\pi^+\pi^+\pi^-$ and $D^+ \to K^-\pi^+\pi^+$ {6}. The pair production of these new particles plus the direct observation of parity violation {7} in the $D^+ \to K^-\pi^+\pi^+$ decay provided overwhelming evidence in favor of a new quantum number conserved in strong and electromagnetic interactions and violated in weak processes. The strong preference for kaons in D decays in particular lent great support to the GIM mechanism which predicts that the weak cs quark coupling should be favored over the cd coupling by the Cabibbo factor $\cot^2(\theta_c) \simeq 20$.

In 1977, the D^{*+} and D^{*0} were found at SPEAR {8} and shown to be the vector meson analogs of the D^+ and D^0 {7}. Because of the limited phase space, the expected strong decays to their pseudoscaler counterparts are greatly suppressed, with the result that these particles have very narrow natural widths. In particular, the decay $D^{*+} \to \pi^+ D^0$ has a Q value of only 5 MeV, a result that will be exploited in our own search for charm.

The evidence for the other charmed mesons in table 1.1, namely the η_c, F^+, and F^{*+}, is not quite on the same footing as the D and D^* observations. The Crystal Ball group appears to have some recent solid evidence {9,10} for an $\eta_c(2970)$ decaying into two photons, but the situation with regard to the F meson is still unclear {11,12,13}. Charmed baryon signals have been reported by several groups {14,15,16,17}, but the best evidence comes from Mark II {18},which has a $PK\pi$ signal at 2.285 GeV, and our own experiment {19}, which

reports a PK_S enhancement at 2.285 GeV. This state is identified with the isosinglet baryon C , better known in the high energy physics community as the Λ_c.

Production of Charm

Because e+e- colliding beams have proven to be a reliable and clean way of producing charm, the question naturally arises: why look for charm in hadron, photon, or neutrino interactions? The answer is that the charm production mechanism can be used as a tool to probe the structure of both the strong and weak interactions. This can be seen naively because the mass of the charmed quark, estimated to be 1.5-1.8 GeV {20}, is so large that it should be very difficult to make charm out of the general hadronic sea in the same way that u, d, and s quarks are created to clothe the final state. Consequently we would expect charm to be created directly by a quark-quark or gluon-gluon interaction calculable by QCD for strong processes, or by a quark-intermediate vector boson interaction in weak processes. The final state charmed quarks would then clothe themselves in this picture by combining with lighter quarks to form the standard hadrons of charm spectroscopy.

For strong interactions charm production is an especially useful tool because Q^2, the invariant mass squared of an associatively produced $c\bar{c}$ pair, is always large enough so that the fundamental QCD coupling constant α_s, which depends on Q^2 as $(1+25\log(Q^2/\Lambda^2)/12\pi)^{-1}$, is expected to be around .25, i.e. small enough to minimize higher order corrections to the more easily calculated first order effects.

Several QCD type charm mechanisms involving quark and/or gluon interactions have appeared in the literature in the last few years. The

quark-antiquark annihilation diagram in fig. 1.1(a) is based on the very successful Drell-Yan 21 model (where the gluon and $c\bar{c}$ quarks are replaced by a photon and two leptons). The 3 diagrams in fig. 1.1(B) represent the central interaction in the gluon fusion model, first proposed by Einhorn and Ellis in 1975 {22}. This latter process might be an especially important source of charm in light of the observation, inferred from deep inelastic electron scattering {23}, that gluons carry roughly half of the nucleon momentum and should therefore be plentiful within the nucleon. Both models have the feature that the charmed quarks emerge from the interaction carrying net color, in spite of the fact that observable hadrons in this theory are required to be color singlets. The point of view taken by many people {22}, and especially the authors of these models, is that there is already so much final state readjustment necessary to produce observable hadrons from free quarks that emission of soft gluons to balance color does not represent a significant perturbation of this process. If we let the color rearrangement takes care of itself and assume that the charmed quarks "dress" themselves into hadrons with unit probability without changing direction significantly, we can make definite predictions for inclusive charmed particle production within these models. The word "definite" here is taken to mean that there are no arbitrary parameters to vary, save perhaps those defining the gluon distribution within the hadron. This is usually considered to be of the form {24}

$$G_i(x) = (n+1)(1-x)^n/16x \qquad i = 1....8$$

where x is the fraction of longitudinal momentum carried by the gluon and the normalization is taken to allow the 8 types of gluons to carry half the hadron momentum. The Brodsky-Farrar counting rules {24} predict n=5 for

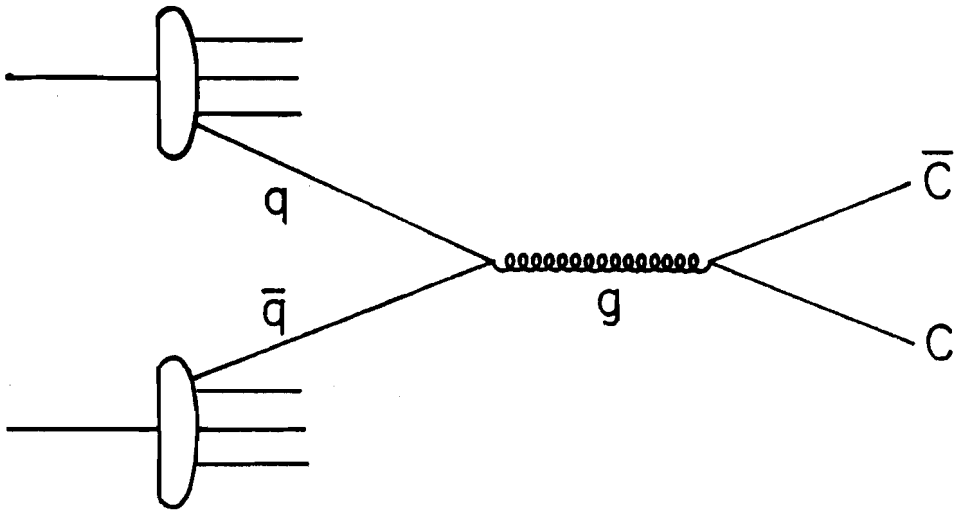

(a)

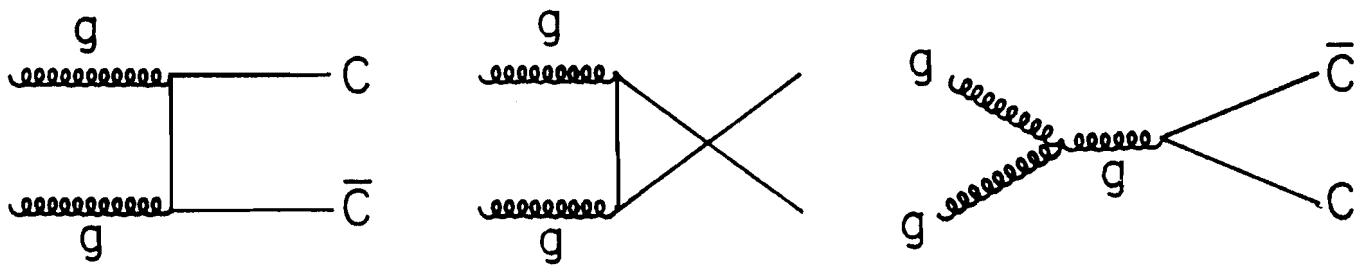

(b)

Some Charm Hadroproduction Diagrams

Figure 1.1

nucleons while Buras and Gaemers {25} slightly prefer n=10 using fits to ep and μp deep inelastic scattering.

It is possible to make contact with experimental data within the context of these models if we make the further assumption {21} that all bound $c\bar{c}$ production takes place in the region $4M_c^2 < Q^2 < 4M_D^2$, with the ψ(3095) accounting for some constant fraction of this part of the cross section. All unbound charm would presumably be relegated to the region $Q^2 > 4M_D^2$. This simplifying approach, which is taken because the ψ is easy to see experimentally through its decay mode into leptons, has been adopted by, e.g., Gluck, Owens, and Reya {26} in calculating ψ hadroproduction from the diagrams in figs. 1.1(a) and 1.1(b) for both πp and pp collisions. Their calculations indicate that, in spite of uncertainties in the quark and gluon distributions, a combination of both $q\bar{q}$ and gg processes is needed to fit the available πp and pp ψ production data. In particular, the counting rule values n=3, n=5, describing the pion and nucleon gluon functions respectively, account for the data rather well.

A somewhat different approach to gluon fusion has been adopted by Carlson and Suaya {27} to explain ψ hadroproduction. They take seriously the color leakage problem discussed previously and note that at least 3 gluons must interact directly to form a ψ, leading to a rather small production cross section. The alternative mechanism they propose is one in which 2 gluons fuse together to form one of the ^3P_J states, which then subsequently decays into a ψ. No predictions are made for unbound charm production. They are able to obtain absolute rates for χ production using the χ --> gg decay rate calculated from the $c\bar{c}$ L=1 wavefunctions for a linear potential, although the resulting ψ cross sections appear to be rather small. Evidence from several experiments {28} indicate that roughly 20 to 40% of all

hadroproduced ψ's do indeed come from χ decay, although one group reports that all its secondary ψ's appear to come from the axial vector state $\chi(3508)$, which cannot couple directly to 2 gluons because of spin and parity.

The preceding discussion on the hadronic production of charm has great significance for photoproduction experiments. From a consideration of vector meson dominance arguments applied to ψ photoproduction, one expects the total photon induced charm cross section to be about 1 μb. Although this figure is a factor of 10 smaller that measured for hadron collisions {29}, the great disparity in total cross sections between the processes (40 mb for hadrons and .1 mb for photons) demonstrates that photoproduction should be approximately 40 times more efficient than hadron collisions for generating charm.

Charm production in QCD can proceed via the diagrams in fig. 1.2(a) involving the fusion of a photon and a gluon to form a $c\bar{c}$ final state {30,31}. Because the gluon x distribution peaks at low values of x and has low average P_t, the $c\bar{c}$ pair emerges from the interaction carrying most of the incident photon energy and little transverse momentum, features commonly associated with diffractive production. The photon gluon mechanism appears to work very well in explaining the energy dependence of ψ photoproduction. Weiler {32} obtains n=5.6 ± 1 for the nucleon gluon distribution using ψ photoproduction data from s=20 to s=400. The asymptotic cross section for total charm production in this model is about 1 μb.

The Drell-Yan type diagram of fig. 1.2(b) can also contribute to charm photoproduction but is suppressed by a factor α_s relative to the gluon fusion graph. This mechanism predicts a relatively slow (x=0) $c\bar{c}$ system which should make its energy dependence easily distinguishable experimentally from that of fig. 1.2(a).

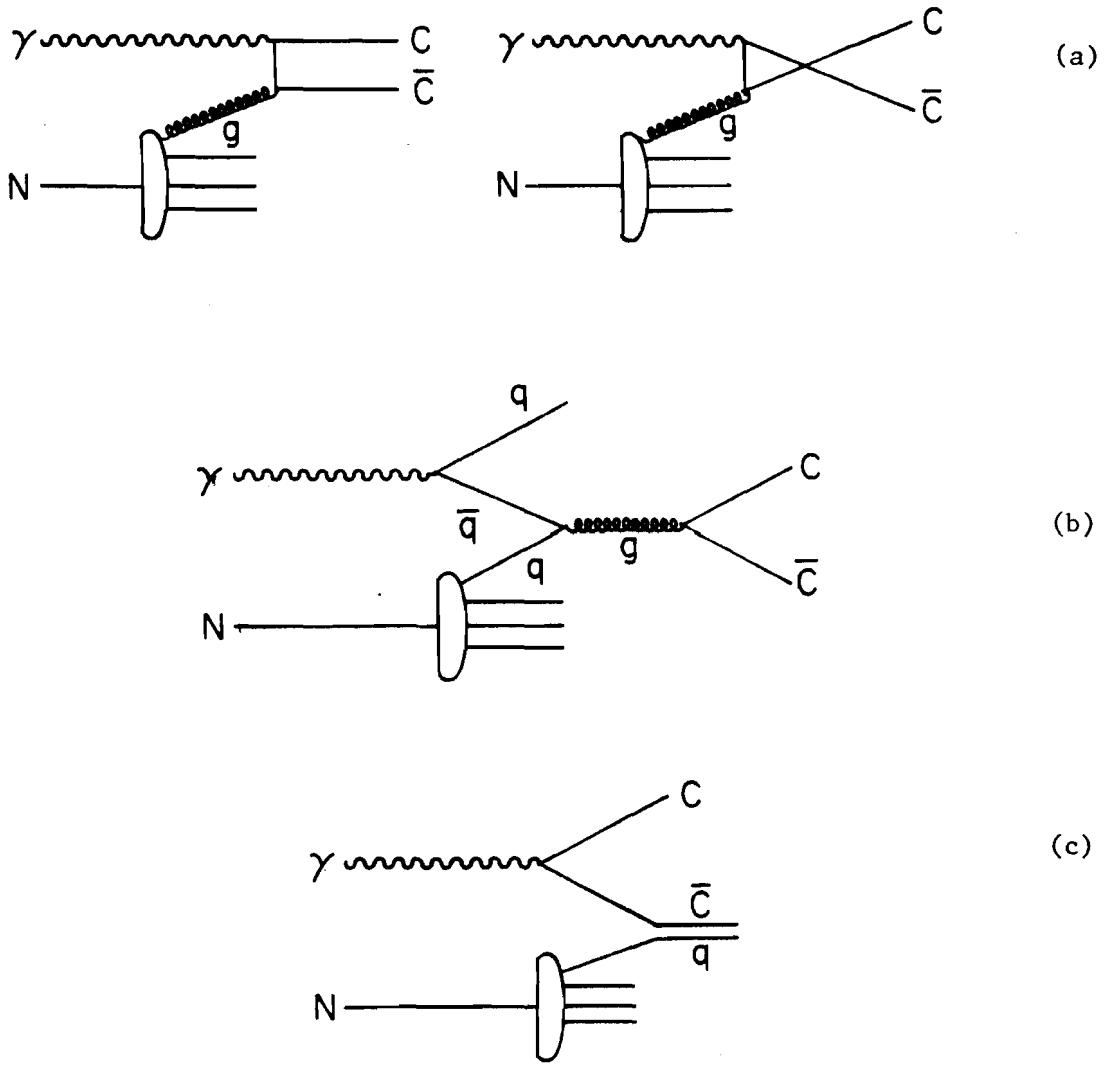

Some Charm Photoproduction Diagrams

Figure 1.2

The diagram of fig. 1.2(c) has been estimated by Halzen and Scott {33} to contribute anywhere from 2 to 4 μb to the charm photoproduction cross section. A particularly striking feature of this diagram is the dramatic asymmetry predicted for the momentum distributions of the 2 charmed particles. Specifically, the C=-1 and C=1 particles should have momentum distributions peaked near x=0 and x=1 respectively, behavior that should easily differentiate this diagram from the other two.

Summary

We have seen in the preceding paragraghs that photoproduction should be one of the most effective tools for producing charm outside of e+e- colliding beams. A measurement of photo-induced charm would constitute an important test of QCD and, given enough statistics, could allow a direct determination of the nucleon gluon distribution and the coupling strengths of the interaction. Measurement of the energy distributions of the charm particles should also provide information on which of the diagrams of fig. 1.2 will dominate.

CHAPTER 2

THE DETECTOR

Experiment 87A was performed at the Fermi National Accelerator Laboratory in the Proton East area from December 1977 to May 1978. We will describe in this chapter all of the relevant aspects of data taking, including the beam, target, and data acquisition system. Because much of this material has been discussed by other people connected with this experiment or its predecessor {19,34,35,36}, we will limit our discussion of certain details and provide appropriate references when needed.

Section A The Neutral Beam

The incident beam consisted mainly of photons resulting from the decay of π^0's produced by collisions of 400 GeV protons on a beryllium target located 450 feet upstream from the detector. Non-interacting protons and charged secondaries were swept into a tungsten dump while the neutrals, at this point mainly neutrons, drifted into the neutral beamline (fig. 2.1). The beam then passed through 2 deuterium filters, with lengths 11m and 23m respectively, which improved the photon/neutron ratio by approximately a factor of 200. The filters, along with the attendant sweeping magnets and collimators, produced a 2" x 2" photon beam having a 1% hadronic contamination due to residual K_L's and neutrons. We studied the effects of the hadron induced background by taking 40% of our data with 6 radiation lengths of lead inserted into the beamline between the two deuterium filters (fig. 2.1). This effectively eliminated interactions from high energy photons, leaving only the hadronic contribution.

Figure 2.2 shows the photon spectrum as measured during special runs in which a 6" x 6" lead glass block was inserted into the beam near the lead glass array. We find that approximately 20% of the photons in our data have

NEUTRAL BEAMLINE

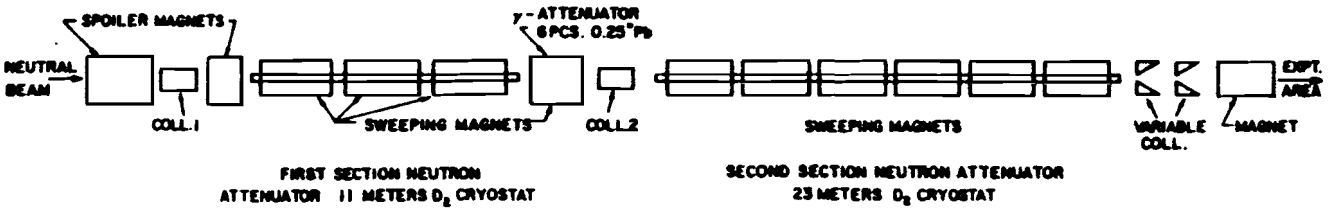

Figure 2.1

E-87 Photon Spectrum

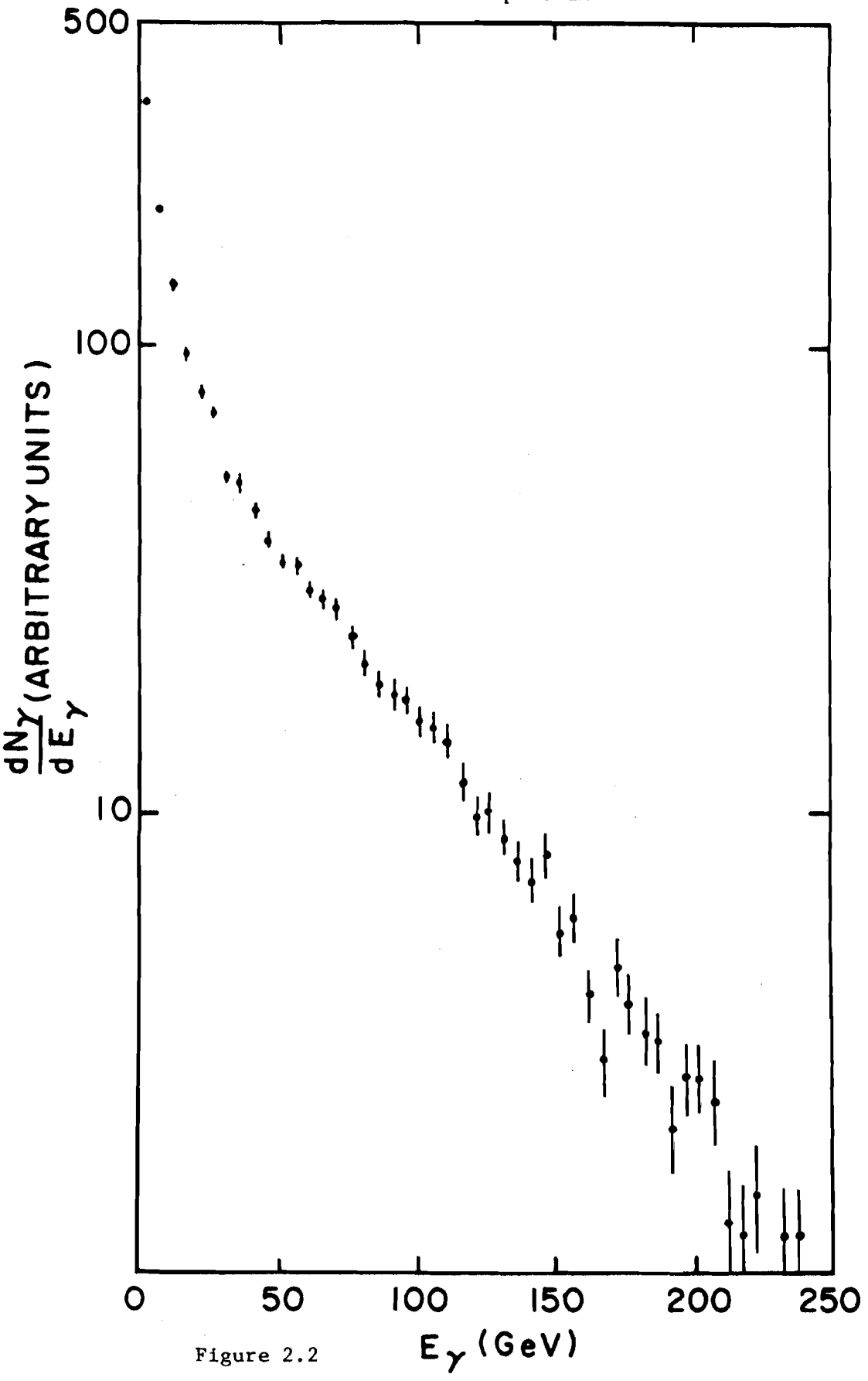

Figure 2.2

an energy greater than 50 GeV. Overall normalization was provided by a small Wilson type quantameter located downstream of the hadron calorimeter. Details of this device can be found in refs. 34 and 35.

Section B The Detector

The layout of the experiment is depicted in fig. 2.3. A system of 5 multiwire proportional chambers (P0-P4), in conjunction with 2 vertical bending magnets (M1 and M2), provided track position and momentum information for particles emerging from a 3" x 3" X 1" scintillator target located upstream of M1. Two threshold Cerenkov counters (C1 and C2) aided in identifying charged hadrons while a lead glass array (LG) provided shower information for photons and electrons. Hadronic particles making it this far deposited most of their energy in a steel-scintillator sandwich hadron calorimeter (HC) while muons passed relatively unhindered to two planes of counters (μH, μV) shielded behind 6 feet of steel for improved hadron rejection.

B1 Target

The target consisted of 20 3" x 3" x 1/24" thick pieces of scintillator individually wrapped in thin aluminum foil (.003") for optical isolation and separately viewed by 2" RCA 8575 phototubes. The composition and thickness correspond to 6.6% of a radiation length and 3.5% of a nucleon absorption length. We chose a "live" target to exploit the belief that D and F mesons might have long enough lifetimes to travel an appreciable distance - say several millimeters - before decaying. In that event the device should note an increase in the number of minimum ionizing particles downstream of the main interaction vertex. Two problems, however, significantly compromised the performance of the target: the presence of slow nuclear fragments which, because of their low velocity and high charge, dump large amounts of

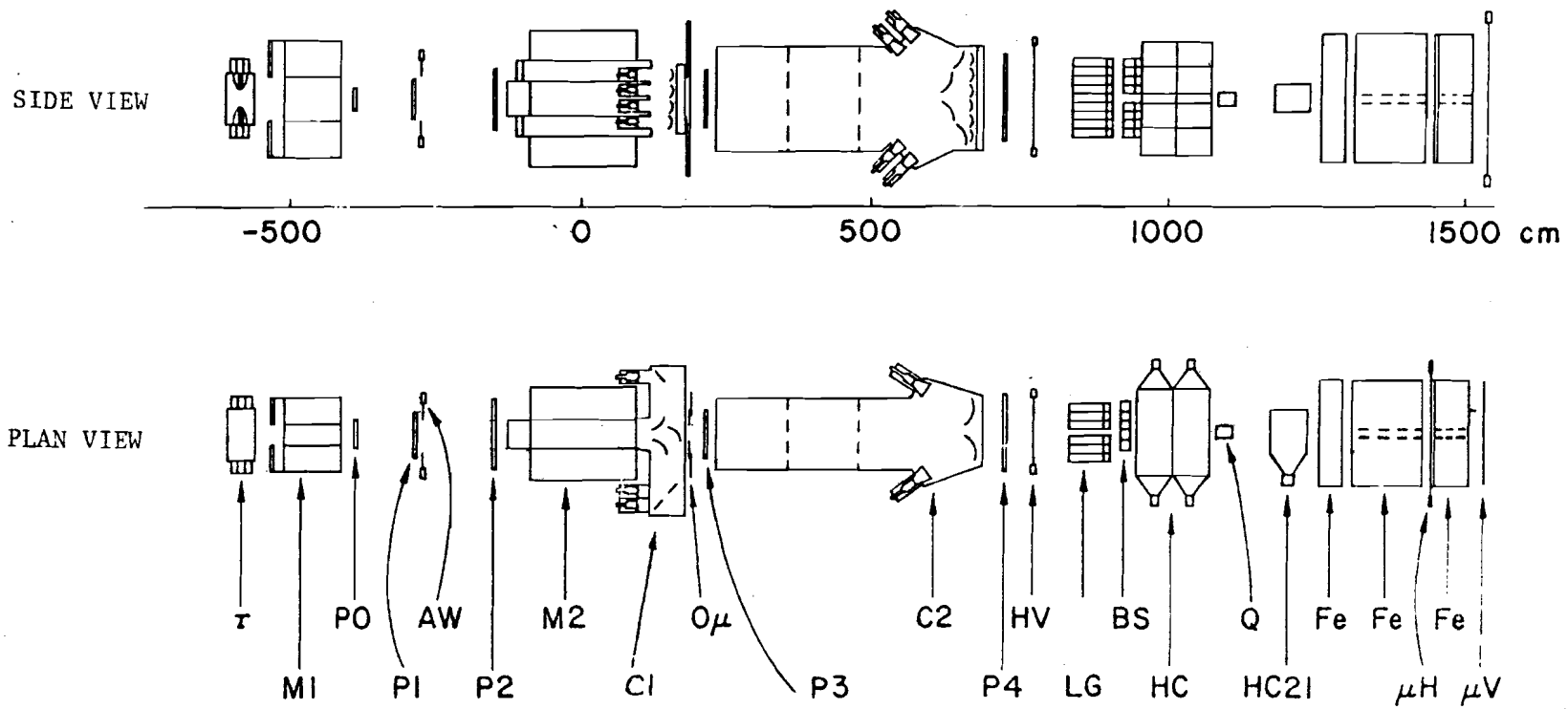

Layout of Experimental Apparatus.

Figure 2.3

ionization energy into the scintillator, and statistical (Landau) fluctuations of the individual pulse heights. Both of these effects hampered pattern recognition.

B2 MWPC System

Each of the 5 multiwire proportional chambers (P0-P4 in fig. 2.3) was made up of 3 planes of wires, labeled X,V, and U. The X wires were vertical and measured coordinates in the non-bend plane while the V and U wires were inclined to the horizontal by an angle of 11.31^0 ($Tan^{-1}.2$). Table 2.1 summarizes the geometrical information of the MWPCs; the reader can find a detailed exposition of the physical construction in ref. 35.

TABLE 2.1
MWPC DATA

Chamber	Aperture	Distance from M2	Number wires		Wire spacing
P0	11.7" x 16.6"	-155.7"	288	X	.04"
			416	V	.04"
			416	U	.04"
P1	20.4" x 30.0"	-112.1"	256	X	.08"
			384	V	.08"
			384	U	.08"
P2	30.8" x 45.2"	-61.4"	384	X	.08015"
			576	V	.08015"
			576	U	.08015"
P3	32.8" x 44.4"	82.6"	416	X	.07874"
			576	V	.07863"
			576	U	.07863"
P4	39.8" x 60.1"	292.1"	336	X	.11895"
			768	V	.08"
			768	U	.08"

In addition to the raw wire information, the MWPCs provided fast signals suitable for incorporation into a trigger. To that end the wires were

grouped together 8,16,24, or 32 at a time depending on the individual plane and distance of the wire from the center, with the single electronic OR of the group (or band) sent to a logic rack. There, fast logic combined the signals into a crude multiplicity trigger which discriminated heavily against the copiously produced e+e- pairs and $\rho \rightarrow \pi\pi$ events. These features are more fully described in section C and in refs. 19 and 35.

In addition to providing trigger information, the band signals for P1 - P4 improved the intrinsic position information of these MWPC's. The signal arrival time, which measures the drift time of the charges generated by a minimum ionizing particle, was digitized by a so-called Time Recording Module (TRM) and encoded as a number between 0 and 31, each count representing 2.5 nsec.

B3 Cerenkov System

Two Cerenkov counters, C1 and C2, provided the bulk of the particle identification capability of our experiment. We will summarize below the physical information about the counters, reserving a discussion of their performance for chapter 4.

C1 is a multi-celled threshold Cerenkov device which has a pure nitrogen gas fill at one atmosphere, a π/K/P threshold of 5.85/21.2/39.2 GeV, and an average yield of 8 photons per β=1 particle (see table 2.2) Because of the limitations of space imposed by the multi-purpose detector, the gas radiator was located in the aperture of the second magnet (see fig. 2.3), leading to a rather interesting light distribution at the mirror plane due to the bending of tracks in the magnetic field of M2. The primary mirrors were composed of .007" mylar (.1% radiation length) coated with aluminum and were tilted at 45° to the beam axis as viewed from above (fig. 2.4) in order to

C_1 Physical Construction

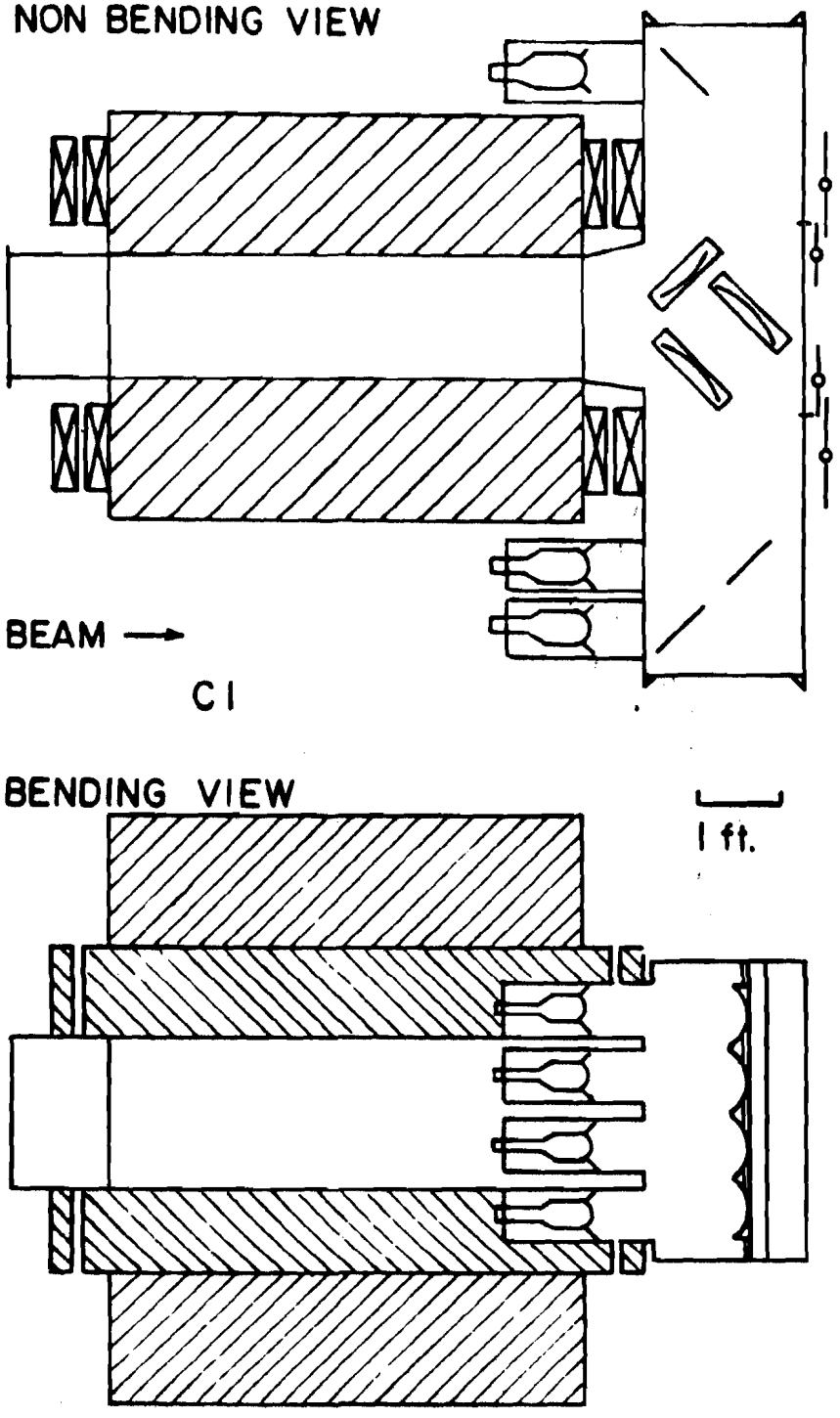

Figure 2.4

bounce the light to a second set of mirrors which focussed it onto the 12 phototubes.

The technical - indeed topological - problem of forcing mylar into a sperical shape was bypassed by performing the horizontal focussing with the primary mirrors and the vertical focussing with the secondary mirrors. The effective geometry, including the extra 50" drift in the vertical dimension, is shown in fig. 2.5.

The second Cerenkov counter, C2, is a multi-celled threshold device (see fig. 2.6) with a 20% Nitrogen - 80% Helium mixture at one atmosphere that provides a π/K/P threshold of 10.7/37.8/70.9 GeV and an approximate yield of 6 photons per β=1 particle. Other data are compiled in table 2.2. The 16 mirrors are composed of thin glass ground to a spherical shape to facilitate focussing to the 3 banks of phototubes mounted on the frame. The mirror geometry is depicted in fig. 2.7. A 7" x 3" hole was left in the center of the counter to enable non-interacting photons and e+e- pairs, which are focussed to a small area near the mirror plane, to pass through.

TABLE 2.2
CERENKOV INFORMATION

	C1	C2
Gas	N2	20% N2-80% He
π/K/P Threshold	5.85/21.2/39.2	10.7/38.7/70.9 GeV/c
Max yield (photons)	8	6
Radiator length	100"	180"
Max cone angle	24mr	13mr
Cone size at mirror	2.4"	2.3"
Z of mirror plane	50"	261"
Central mirror size	4.75" x 10"	7" x 16"
Side mirrors size	16" x 10"	23" x 11"
Number of tubes	12	16
Phototube type	RCA 4452	RCA 8854 (Quanticon)

C_1 Mirror Plane

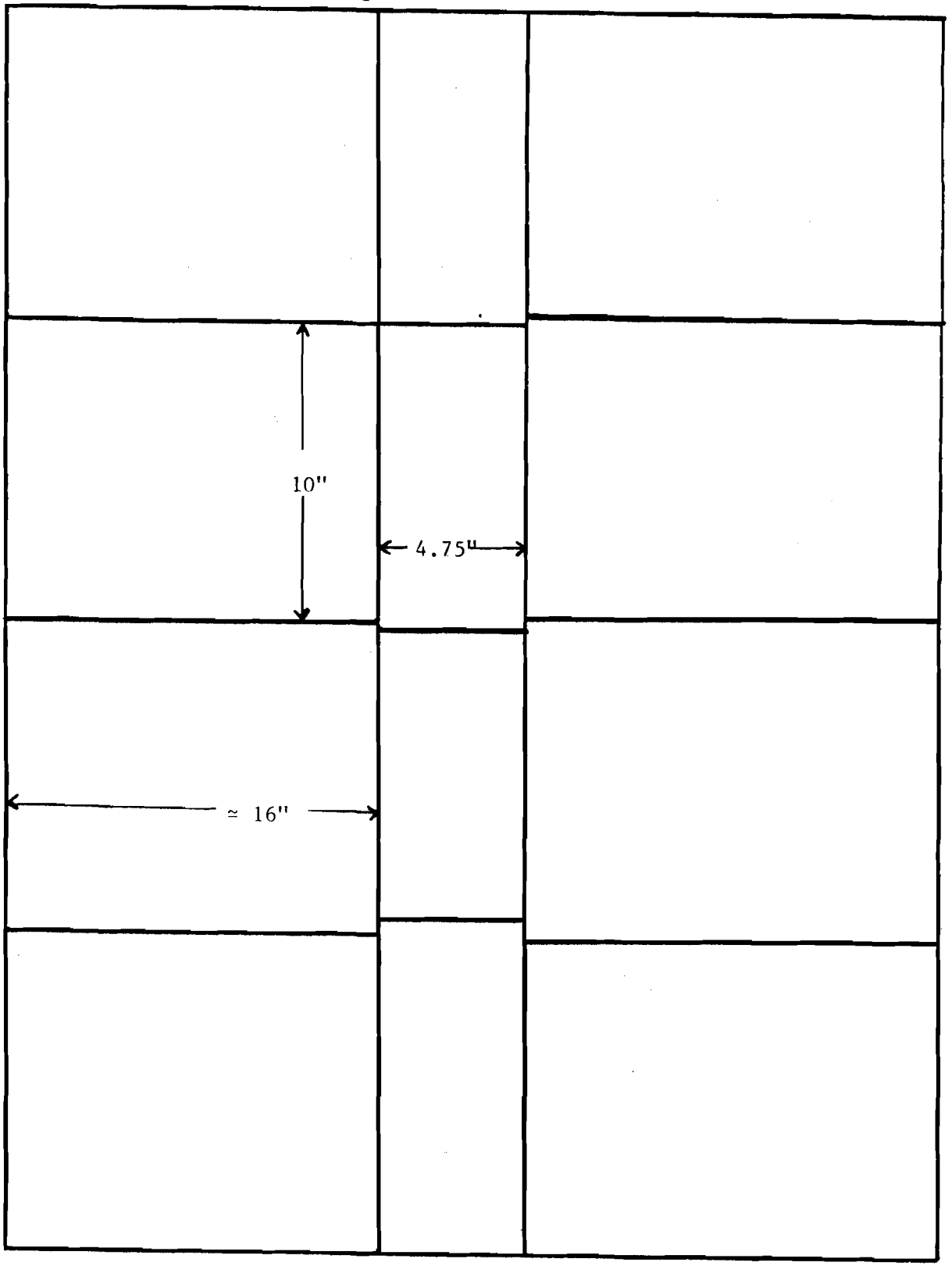

Figure 2.5

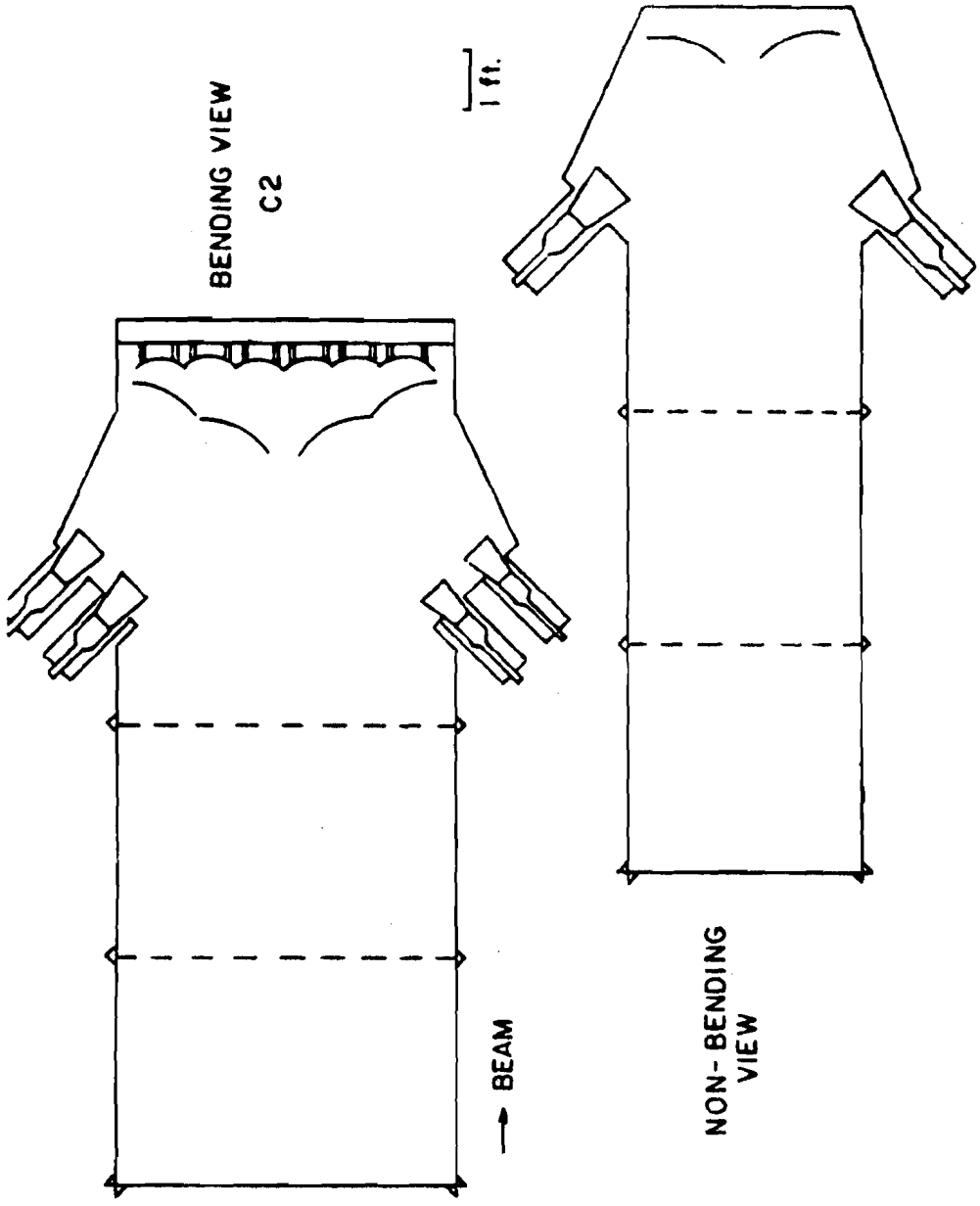

Figure 2.6

B4 Lead Glass Array

The lead glass system was located in back of P4 (fig. 2.3) and was composed of a central array of 42 2.5" x 2.5" x 23" blocks (SF2) surrounded by an outer array of 48 6" x 6" x 18" blocks (SF5) as pictured in fig. 2.8. A 4" vertical gap was left in the middle of the arrangement to facilitate the passage of non-interacting photons and e+e- pairs. Because the lead glass formed part of the energy trigger, the tubes were approximately gain balanced with an average calibration constant of 10 MeV per ADC count. The gain for each block was monitored by a system of light emitting diodes on a run to run basis and by special electron beam tests performed periodically over the course of the experiment.

A bank of 8 16 radiation length shower counters sat in back of this array in order to pick up neutral energy passing through the 4" slit separating the two halves of the lead glass. Each of the shower counters measured 20" x 6" and was composed of 16 interleaved lead-scintillator sheets viewed by an Amperex 58AVP phototube. An empty 20" x 6" slot centered on the beam was left to allow non-interacting photons and e+e- pairs to pass through.

For this analysis no attempt was made to use information from the lead glass to reconstruct π^0's from showers; that problem is confronted in ref. 34.

B5 Hadron Calorimeter

Two longitudinally separated sections of 10 modules apiece form the basis of the hadron calorimeter as pictured in fig. 2.9. Each module had the same overall structure: 12 7/4" steel plates interleaved with 1/4" scintillator sheets that fanned into a mixing block viewed by a 5" Amperex 58AVP phototube. A 6" x 6" hole was left in the center to allow the

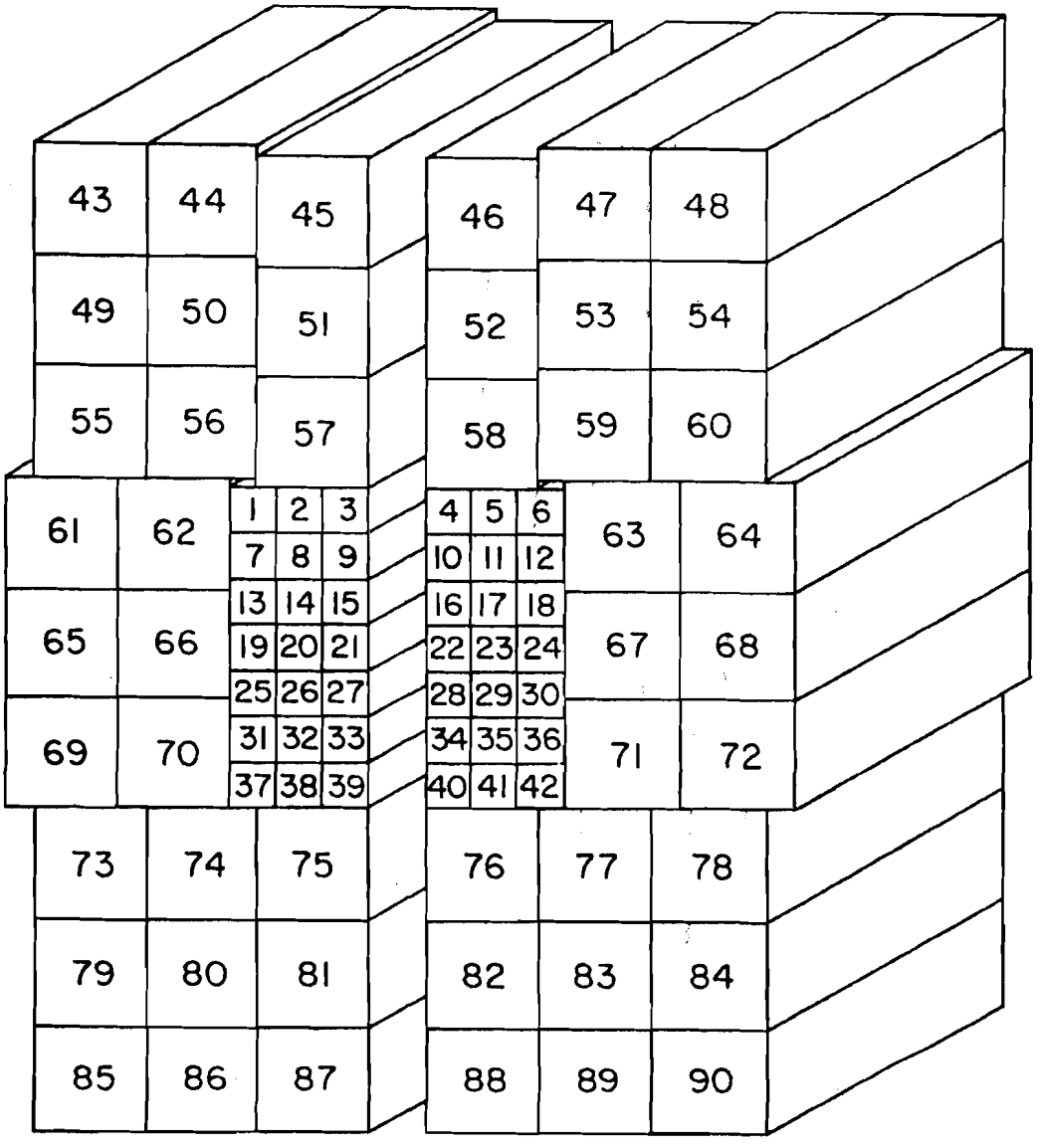

Lead Glass Array.

Figure 2.8

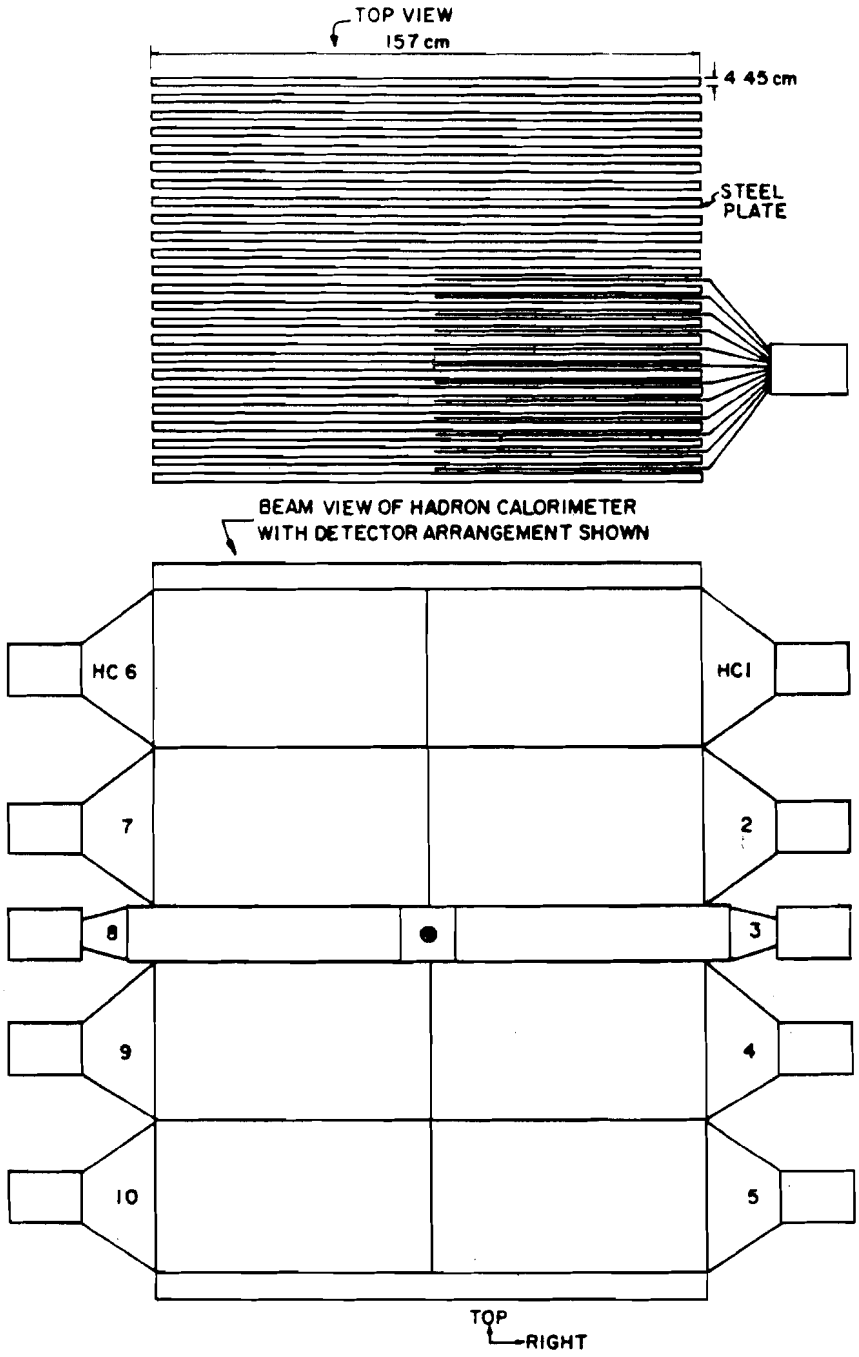
TOP VIEW
157 cm
4 45 cm
STEEL PLATE
BEAM VIEW OF HADRON CALORIMETER WITH DETECTOR ARRANGEMENT SHOWN
HC 6
HC1
7
2
8
3
9
4
10
5
TOP
RIGHT

Figure 2.9

non-interacting photon beam to deposit its energy in a quantameter directly downstream of the calorimeter. Another 33" x 18" module sat in back of the quantameter to pick up residual hadronic energy in the hole.

The presence of 10 radiation lengths of lead along an 8 inch vertical strip between the lead glass and calorimeter compromised the ability of the latter device to resolve hadronic showers. The primary purpose of the calorimeter was to trigger on events containing a large amount of hadronic energy.

B6 Muon Counters

An arrangement of 40 scintillation counters and 2 large blocks of steel (fig. 2.10) provided muon identification for this experiment. Since the analysis performed here ignores muon tagging for the most part, we refer all details of the muon reconstruction to ref. 36.

Section C The Trigger

A photon beam presents special difficulties to the experimenter because of the large numbers of e+e- pairs it produces. Because the pair cross section is 30 mb/nucleon for our scintillator target compared to the total photon cross section into hadrons of 110 μb/nucleon, pair production swamps the "interesting" part of the photon cross section by about a factor of 300 to 1. In addition, the high flux of these pairs causes a dangerously large current to flow in the proportional chambers. While the second problem can be alleviated somewhat by trip circuitry and a magnet (M1 in fig. 2.3) to sweep out low energy electrons, the first must be attacked by designing a discriminating trigger that takes advantage of the special nature of e+e- production: forward production with a characteristic angle of 10^{-4} to 10^{-5} radian from the beam.

INNER MUON DETECTOR

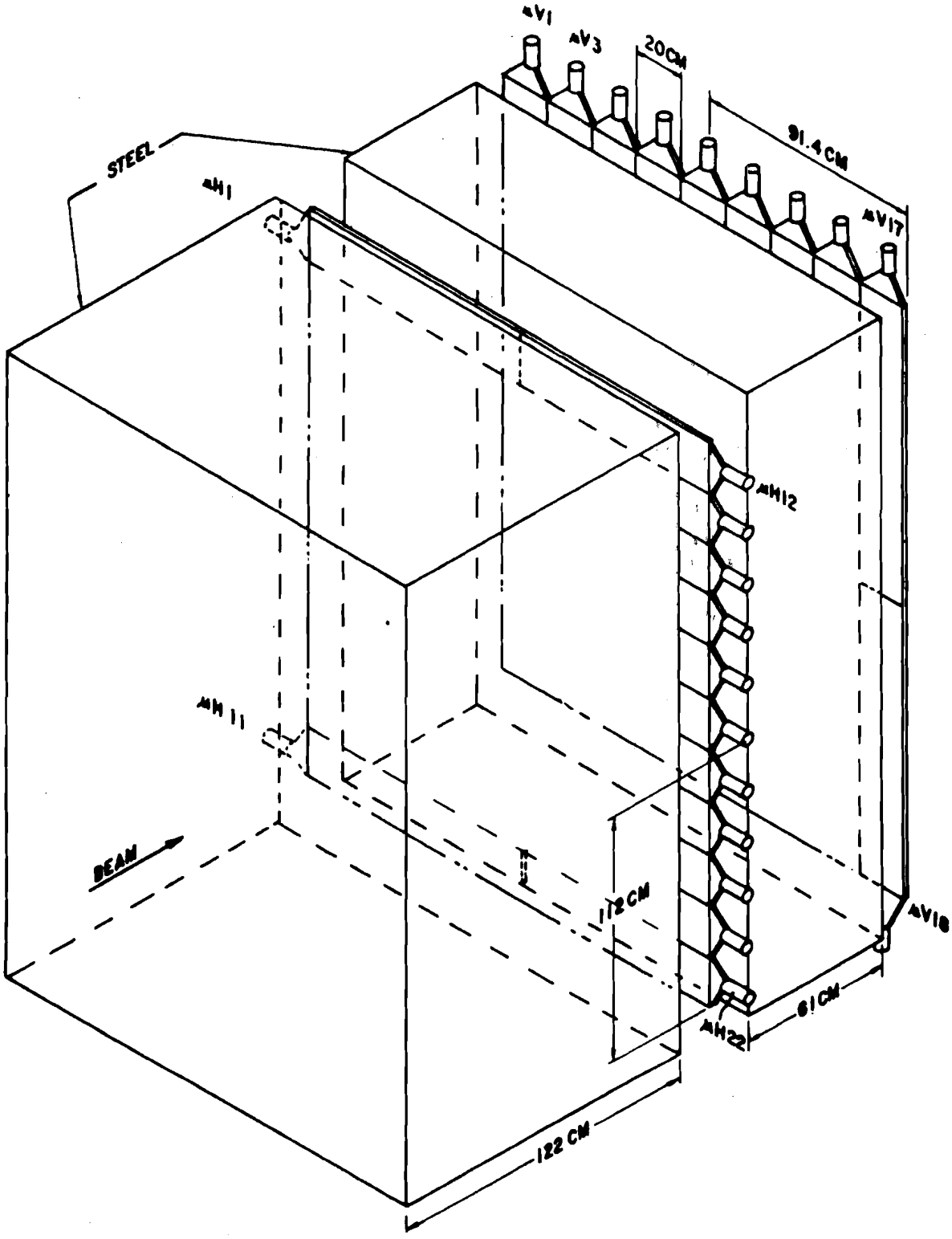

Figure 2.10

The triggering was performed in two stages. First, a Master Gate (MG) required that the last 2 segments of the active target be set in coincidence with the presence of at least one particle outside of the 2" wide beam region. The latter task was accomplished by asking for a hit in each of two scintillator planes mounted behind P4 (H and V in fig. 2.11). The master gate can then be written symbolically as

$$MG = T19 \cdot T20 \cdot H \cdot V$$

The second triggering stage, known as the DC logic, attempted to select events satisfying considerably more complex criteria than those posed by the master gate. Inputs to the DC logic included scintillation counter status, band information at various levels of organization, and the energy deposited in the lead glass, hadron calorimeter, or their sum. The DC logic encoded its output as 16 logic levels known as busslines which received their name from the fact that they were sent - or "bussed" - to several trigger modules. These modules derived triggers from logical combinations of busslines; one could demand, veto, or ignore any bussline in a logical AND operation (see the pin logic schematic in fig. 2.12). For example, the main trigger of this experiment, known as PIN 6, was generated by a single module and was equivalent to the logical equation

$$PIN\ 6 = 1 \cdot 8 \cdot 9 \cdot 12 \cdot 13 \cdot 14 \cdot \overline{16}$$

where the rhs refers to bussline numbers.

The trigger modules had the additional capability of being pre-scaled by any power of 2 up to 65536 enabling the experimenter to record samples of other kinds of data for the purpose of monitoring efficiencies. In the above example, for instance, the following triggers were simultaneously recorded:

$$PIN\ 7 = 1 \cdot 8 \cdot 9 \cdot 12 \cdot \overline{16} \qquad \text{pre-scale } 64$$
$$PIN\ 8 = 8 \cdot 13 \cdot 14 \cdot \overline{16} \qquad \text{pre-scale } 128$$

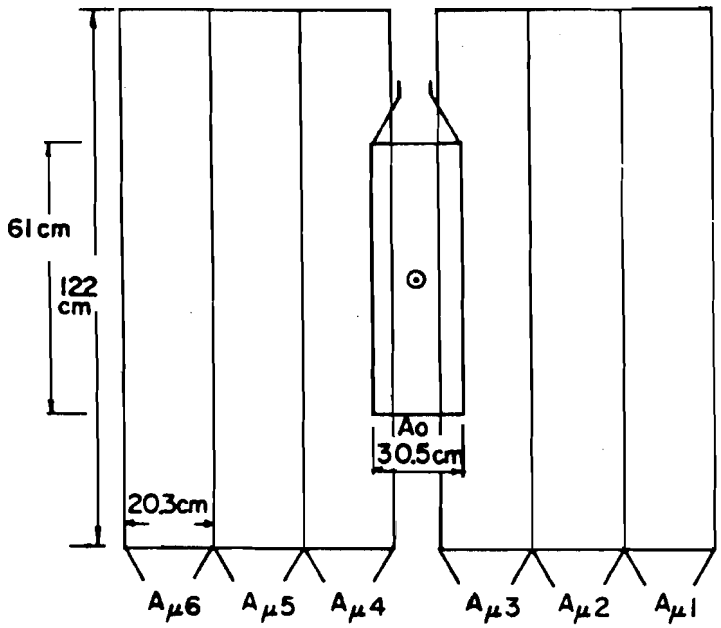

(a)

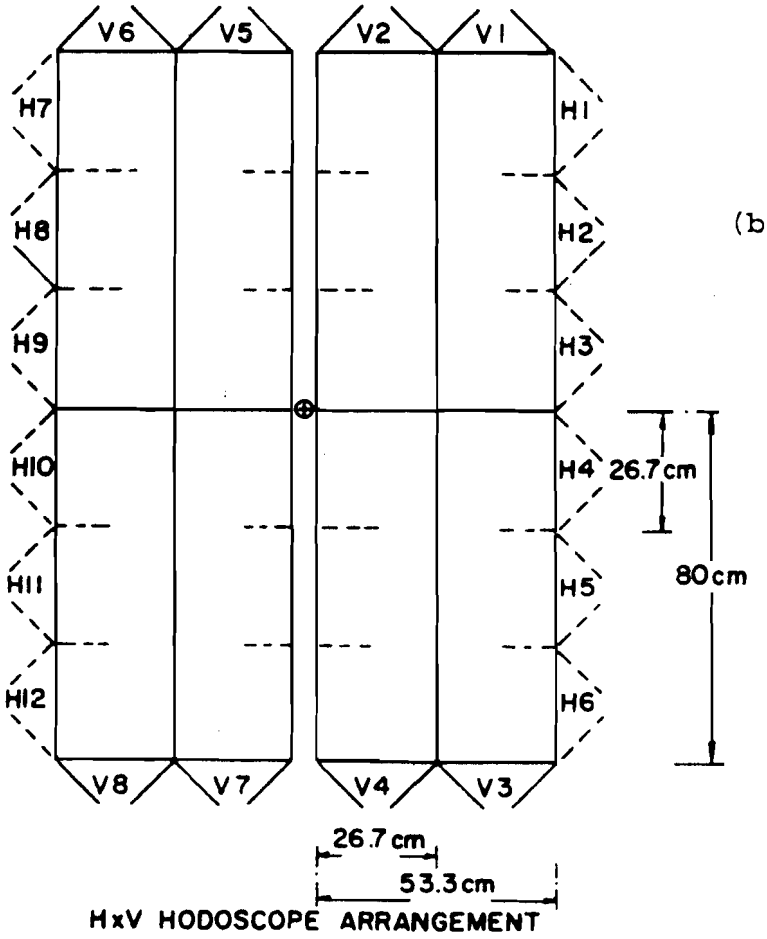

(b)

Figure 2.11

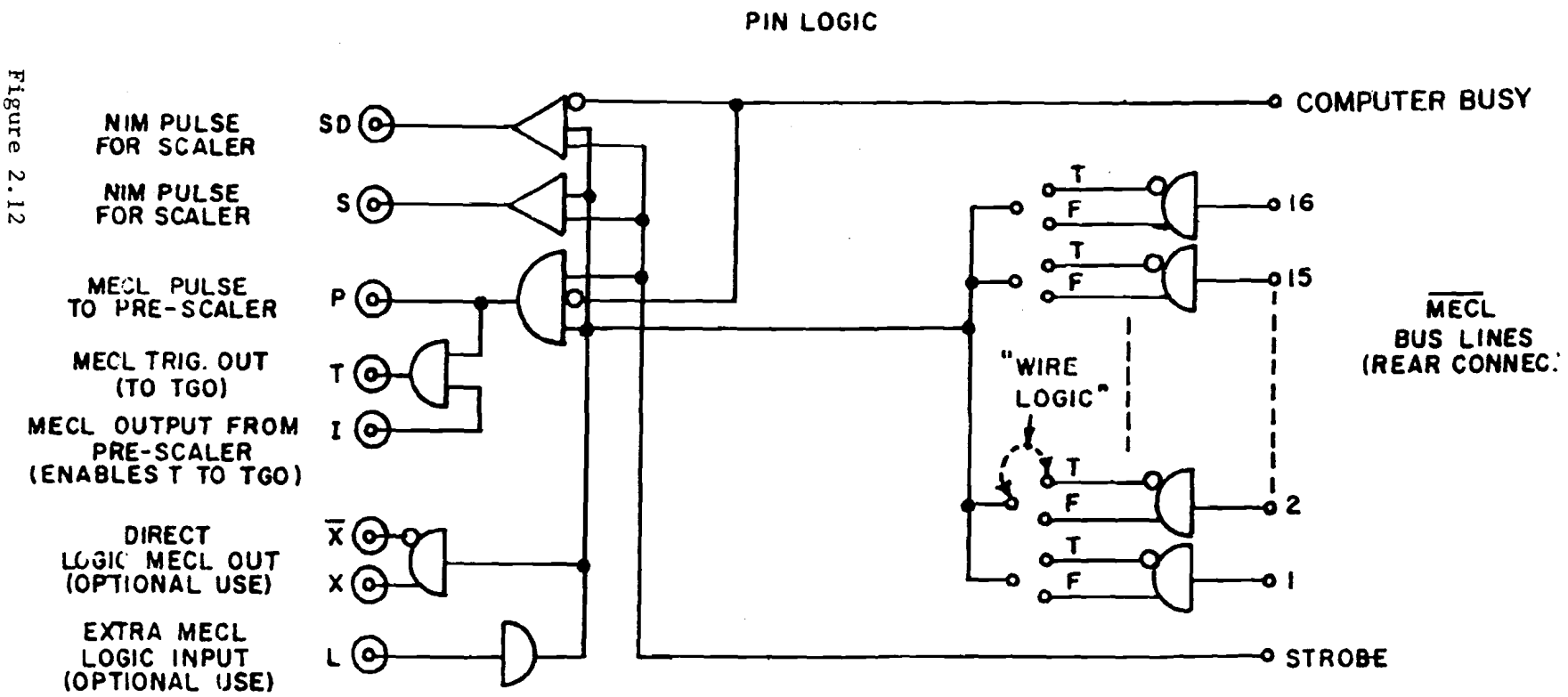

Schematic logic diagram of Pin Logic Module

Figure 2.12

These two triggers allowed us to establish the efficiency of busslines 13,14 (energy) and 1,9,12 (multiplicity) within the PIN 6 trigger.

To gain a better understanding of how the busslines were set, we must discuss the MWPC logic in some detail. As stated previously, each of the 15 planes comprising P0-P4 had a number of regions, 32 in all, which represented the OR of several adjacent wires. The signals derived from the fast ORs were then processed by a set of logic modules to provide information on the number and disposition of the tracks in the event.

The multiplicity problem was relatively straightforward and involved associating a multiplicity with every chamber according to the prescription:

$$N_i = \mathrm{MEDIAN}(P_iX, P_iV, P_iU) \qquad i = 0,1,2,3,4$$

where PiX etc. refers to the number of bands hit in that plane. The multiplicity busslines (see diagram in fig. 2.13) can then be defined as:

1. Bussline 9 MAX < 11
   Defined by MAX(N0,N1,N2,N3,N4) < 11

2. Bussline 10 2 Body IN/IN (Not used in this analysis)
   Defined by MEDIAN(N0,N1,N2) > 1 and MIN(N3,N4) > 1

3. Bussline 11 2 Body IN/OUT (Not used in this analysis)
   Defined by MEDIAN(N0,N1,N2) > 1 and MIN(N3,N4) > 0

4. Bussline 12 Multi-body
   Defined by MEDIAN(N0,N1,N2) > 2 and MIN(N3,N4) > 1

The X planes (measuring the non-bend coordinate) for P2-P4 were further organized into a system known as the X logic, composed of 3 regions: Central, a 2"-2.5" wide area where almost all of the e+e- pairs were expected to hit; Inner, comprising most of the rest of the active chamber area; and Outer, including the outermost 4 bands of P2 and P3. Table 2.3 contains a complete description of which wires were actually OR'ed together in each of the band regions. The following busslines were defined from the X logic:

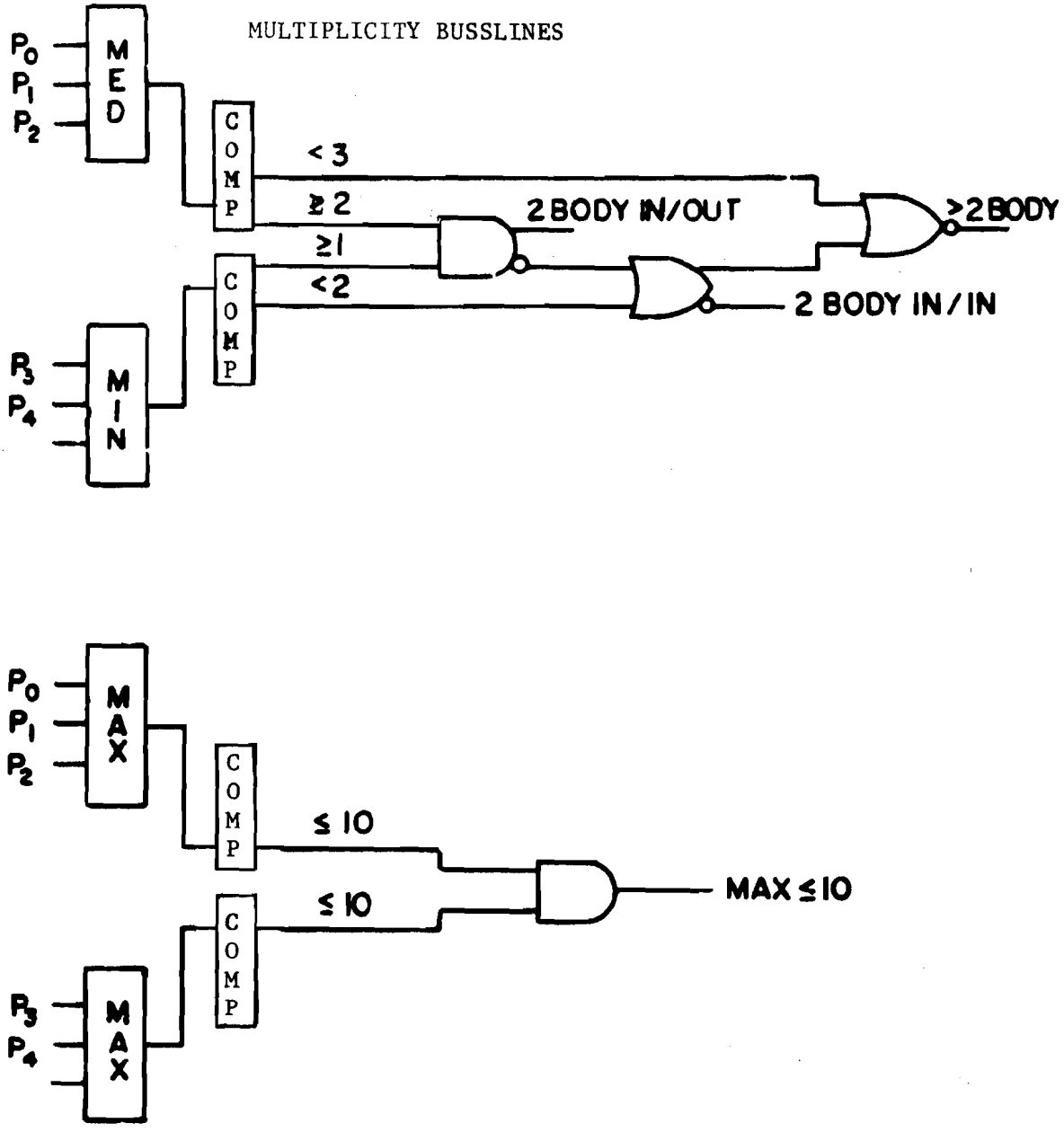
MULTIPLICITY BUSSLINES
P0
P1
P2
MED
COMP
< 3
≥ 2
2 BODY IN/OUT
≥2 BODY
≥1
<2
2 BODY IN/IN
P3
P4
MIN
COMP
P0
P1
P2
MAX
COMP
≤ 10
≤ 10
MAX ≤ 10
COMP
P3
P4
MAX

Figure 2.13

TABLE 2.3

	OFFSET	AREA 1 # BANDS WIDTH	AREA 1 START WIRE/ REGION	AREA 1 STOP WIRE/ REGION	AREA 2 # BANDS WIDTH	AREA 2 START WIRE/ REGION	AREA 2 STOP WIRE/ REGION	AREA 3 # BANDS WIDTH	AREA 3 START WIRE/ REGION	AREA 3 STOP WIRE/ REGION
P_0X	0	2/16	0/0	31/1	28/8	32/2	255/29	2/16	256/30	287/31
P_0V	0	10/16	0/0	159/9	12/8	160/10	255/21	10/16	256/22	415/31
P_0U	0	10/16	0/0	159/9	12/8	160/10	255/21	10/16	256/22	415/31
P_1X	0				32/8	0/31	255/0			
P_1V	0	8/16	0/31	127/24	16/8	128/23	255/8	8/16	256/7	383/0
P_1U	0	8/16	0/31	127/24	16/8	128/23	255/8	8/16	256/7	383/0
P_2X	1	8/16	1/31	128/24	16/8	129/23	256/8	8/16	257/7	384/0
P_2V	0	4/24	0/0	95/3	24/16	96/4	479/27	4/24	480/28	575/31
P_2U	0	4/24	0/0	95/3	24/16	96/4	479/27	4/24	480/28	575/31
P_3X	48	6/16	48/2	143/7	16/8	144/8	271/23	6/16	272/24	367/29
P_3V	80	10/16	80/31	239/22	12/8	240/21	355/10	10/16	336/9	496/0
P_3U	80	10/16	80/31	239/22	12/8	240/21	355/10	10/16	336/9	496/0
P_4X	8	4/16	8/0	71/3	24/8	72/4	263/27	4/16	264/28	327/31
P_4V	32	6/32	32/31	223/26	20/16	224/6	543/11	6/32	544/5	735/0
P_4U	32	6/32	32/31	223/26	20/16	224/6	543/11	6/32	544/5	735/0

	CENTRAL	INNER	OUTER
P_2X	14-17	7-13 18-24	0-6 25-31
P_3X	14-17	2-13 18-29	0-1 30-31
P_4X	15-16	0-14 17-31	NONE

1. Bussline 1 Xin > 1
   At least 2 tracks must be outside central region.

2. Bussline 2 Xin/Xout (Not used in this analysis)
   AT least 2 tracks must lie outside central region, one of which strikes the outer region.

3. Bussline 3 Xin > 0 (Not used in this analysis)
   At least one track must lie outside of central region.

Fig. 2.14 contains a precise pictorial definition of the X logic busslines.

Three other busslines relevant to this thesis and involving a measurement of energy deposition are summarized below:

1. Bussline 13 Hadron Calorimeter energy (EHC) > 42 GeV
2. Bussline 15 Lead Glass energy (ELG) > 11 GeV
3. Bussline 14 EHC + ELG > 75 GeV

The electronic composition of these busslines is shown in the schematic diagram in fig. 2.15. Note that the energy busslines are not all independent of each other because bussline 14 is set by the passive sum of the dynode signals coming from the lead glass and calorimeter. In chapter 4 we will develop a model of bussline behavior that will be seen to reproduce this coupling.

Finally, two busslines, both involving scintillation planes, are briefly noted:

1. Bussline 8 AW counters
   These were 4 18" x 36" scintillation counters arranged just outside of the active area of P1. The 2 side AW counters were used as a veto in 42% of the running in order to enhance the diffractive component of the cross section .

2. Bussline 16 AO
   This was a 12" x 24" counter placed just upstream of the target used to veto events with a charged particle in the initial state.

Table 2.4 summarizes the bussline information and schematically describes the composition of the triggers used in this experiment.

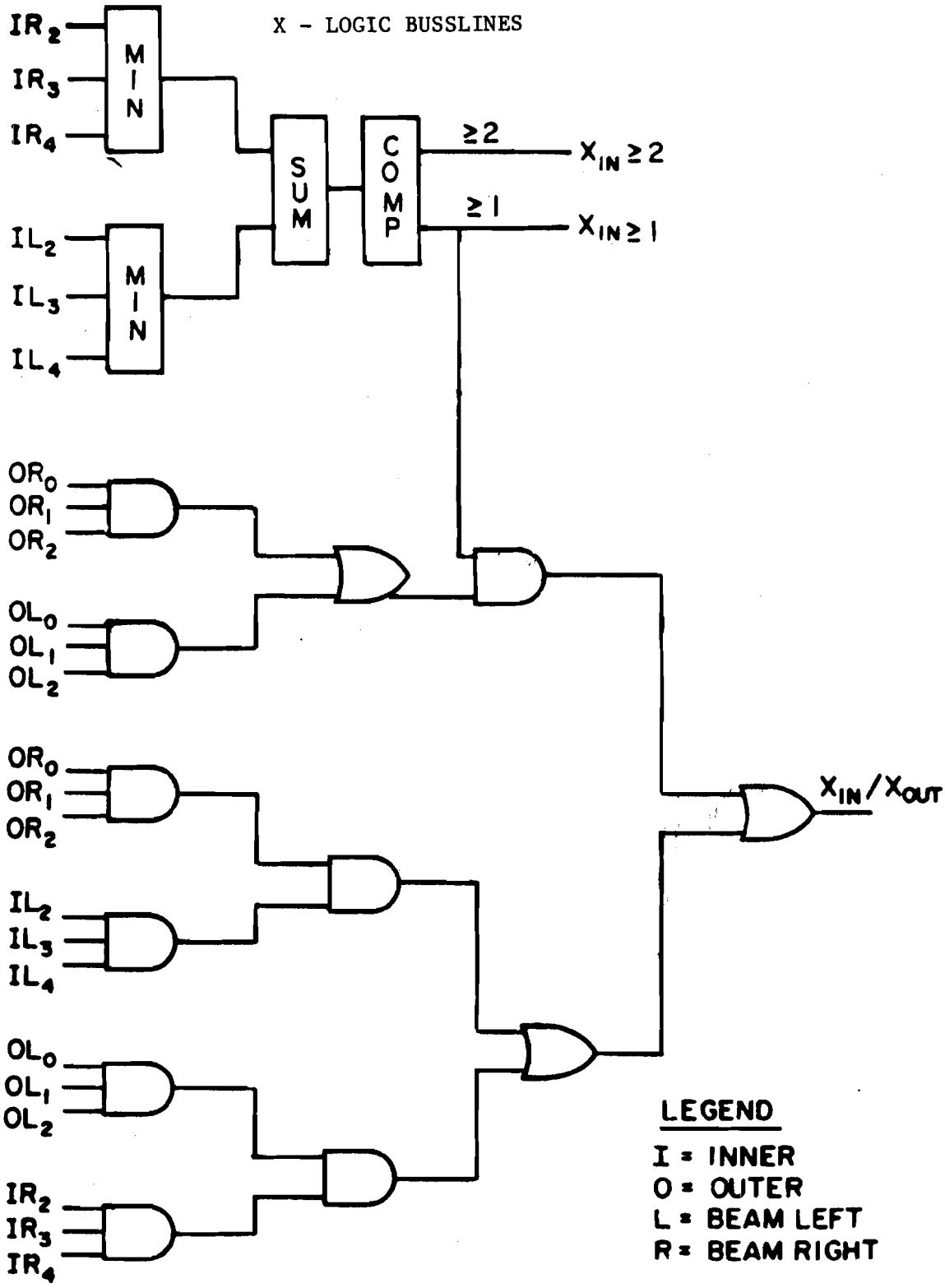
X - LOGIC BUSSLINES
IR2
IR3
IR4
MIN
IL2
IL3
IL4
MIN
SUM
COMP
≥2
≥1
XIN ≥ 2
XIN ≥ 1
OR0
OR1
OR2
OL0
OL1
OL2
OR0
OR1
OR2
IL2
IL3
IL4
OL0
OL1
OL2
IR2
IR3
IR4
XIN/XOUT
LEGEND
I = INNER
O = OUTER
L = BEAM LEFT
R = BEAM RIGHT

Figure 2.14

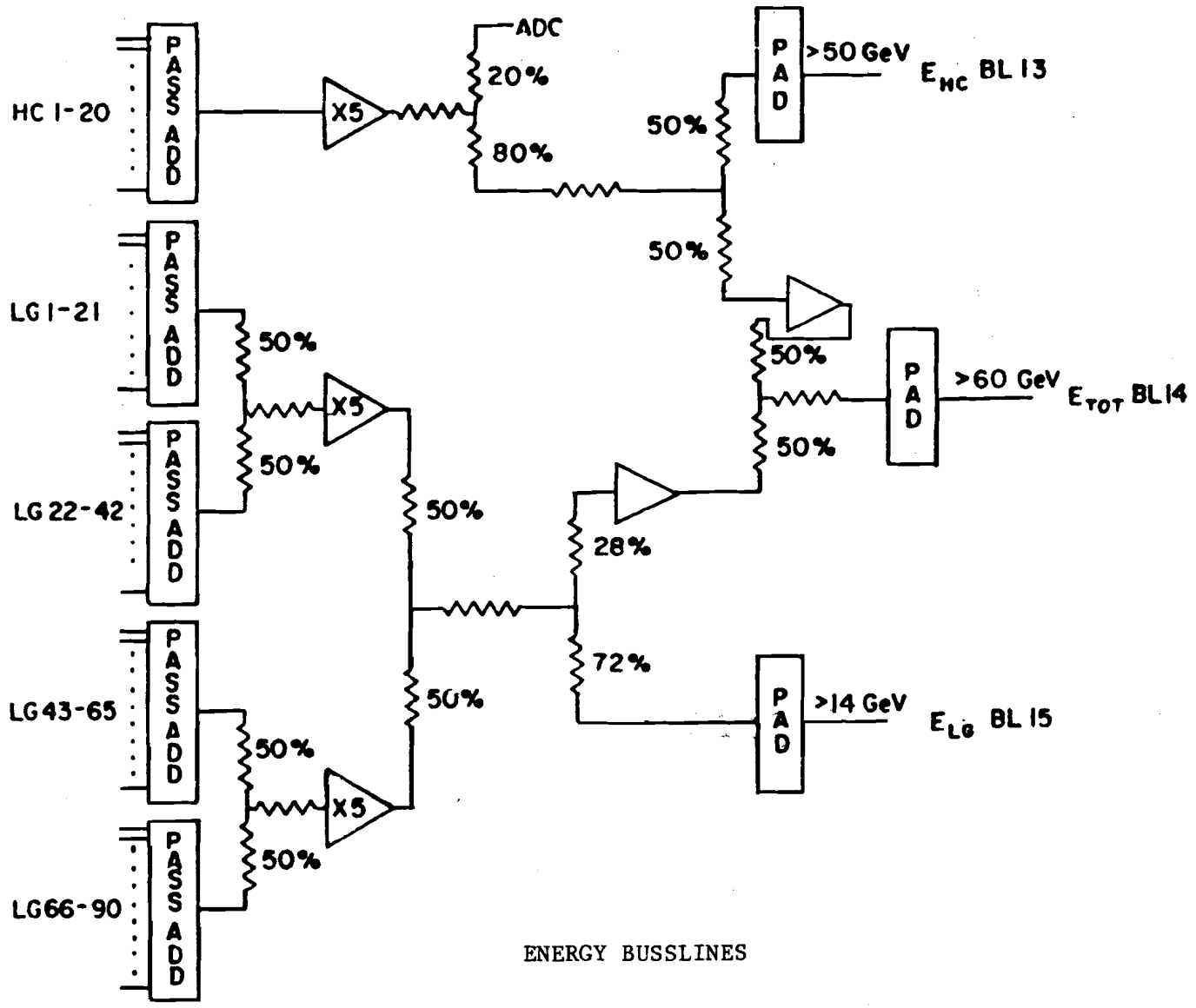
HC 1-20
LG 1-21
LG 22-42
LG 43-65
LG 66-90
PASS ADD
X5
ADC
20%
80%
50%
28%
72%
PAD
>50 GeV
E_{HC} BL 13
>60 GeV
E_{TOT} BL 14
>14 GeV
E_{LG} BL 15
ENERGY BUSSLINES

Figure 2.15

TABLE 2.4

PIN LOGIC & BUSSLINES

Bus Line \ Pin Logic		2μ in/in	2μ in/out	2e in/in		Hadrons	Mwpc	E_{TOT}	μe in/in	μe out/in
$X_{in} \geq 2$				✓		✓	✓			
X_{in}/X_{out}			✓							✓
$X_{in} \geq 1$		✓							✓	
$2\mu_{in}$		✓								
μ_{in}			✓						✓	
μ_{out}			✓							✓
AW left + right		X	X	X					X	X
Max. ≤ 10		✓	✓			✓	✓		✓	✓
2 body in / in		✓		✓					✓	
2 body in / out			✓	✓						✓
> 2 body				X		✓	✓		X	X
E_{HC}				X		✓		✓	X	X
E_{TOT}						✓		✓		
E_{LG}				✓					✓	✓
$A_0 + A_\mu$		X	X	X		X	X	X	X	X

Section D Data Acquisition System

As soon as a trigger was generated, signals were sent to initiate digitization of the ADCs and to set a computer busy signal that blocked any trigger attempting to come in while the event was being read (This could happen because the DC logic operated continuously). The event readout was handled by a system called ACE which read all relevant information generated by an event, such as MWPC, TRM, ADCs, and coincidence register latches, and stored it in a 64K buffer solid state memory at the rate of approximately 250 μsec per event.

The buffer was written out by means of an XDS Sigma 3 computer to an 800 bpi magnetic tape between beam spills, taking 7 seconds to record an average of 200 events. A tape typically containing 22000 events could be written in about 25 min. assuming a Fermilab duty cycle of 1 spill per 8 seconds. Fig. 2.16 shows the interdependence of the various components of the data acquisition system.

At the end of each spill, the computer wrote a special record preserving the many scalers used for monitoring experimental conditions. These included proton flux monitors, beam scraping monitors, singles rates, and trigger rates with and without deadtime. This deadtime arose at both the master gate and DC logic levels; average values for our run being 13% for MG and 11% for DC logic.

The origin of the deadtime needs to be discussed in some detail. The master gate module (confusion logic) blocks the generation of a master gate for 250 nsec after the generation of the previous one to allow the slower DC logic time to make its decision on whether or not to keep the event. It also blocks master gate formation for 100 nsec following any singles input (see fig. 2.17). Two outputs on the module can be used to monitor the number of

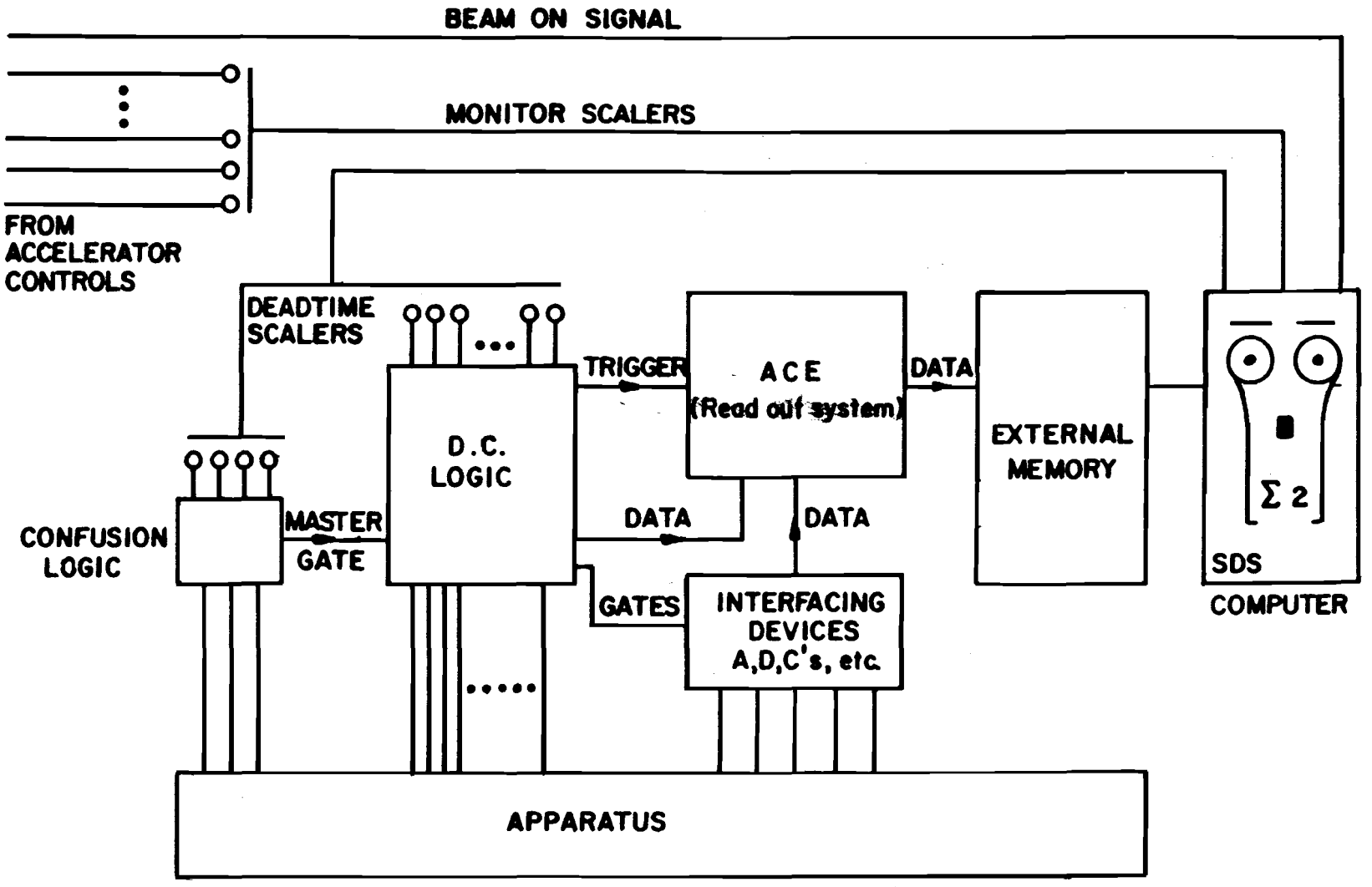
BEAM ON SIGNAL
MONITOR SCALERS
FROM
ACCELERATOR
CONTROLS
DEADTIME
SCALERS
TRIGGER
ACE
(Read out system)
DATA
EXTERNAL
MEMORY
D.C.
LOGIC
CONFUSION
LOGIC
MASTER
GATE
DATA
DATA
GATES
INTERFACING
DEVICES
A,D,C's, etc.
Σ 2
SDS
COMPUTER
APPARATUS

Figure 2.16

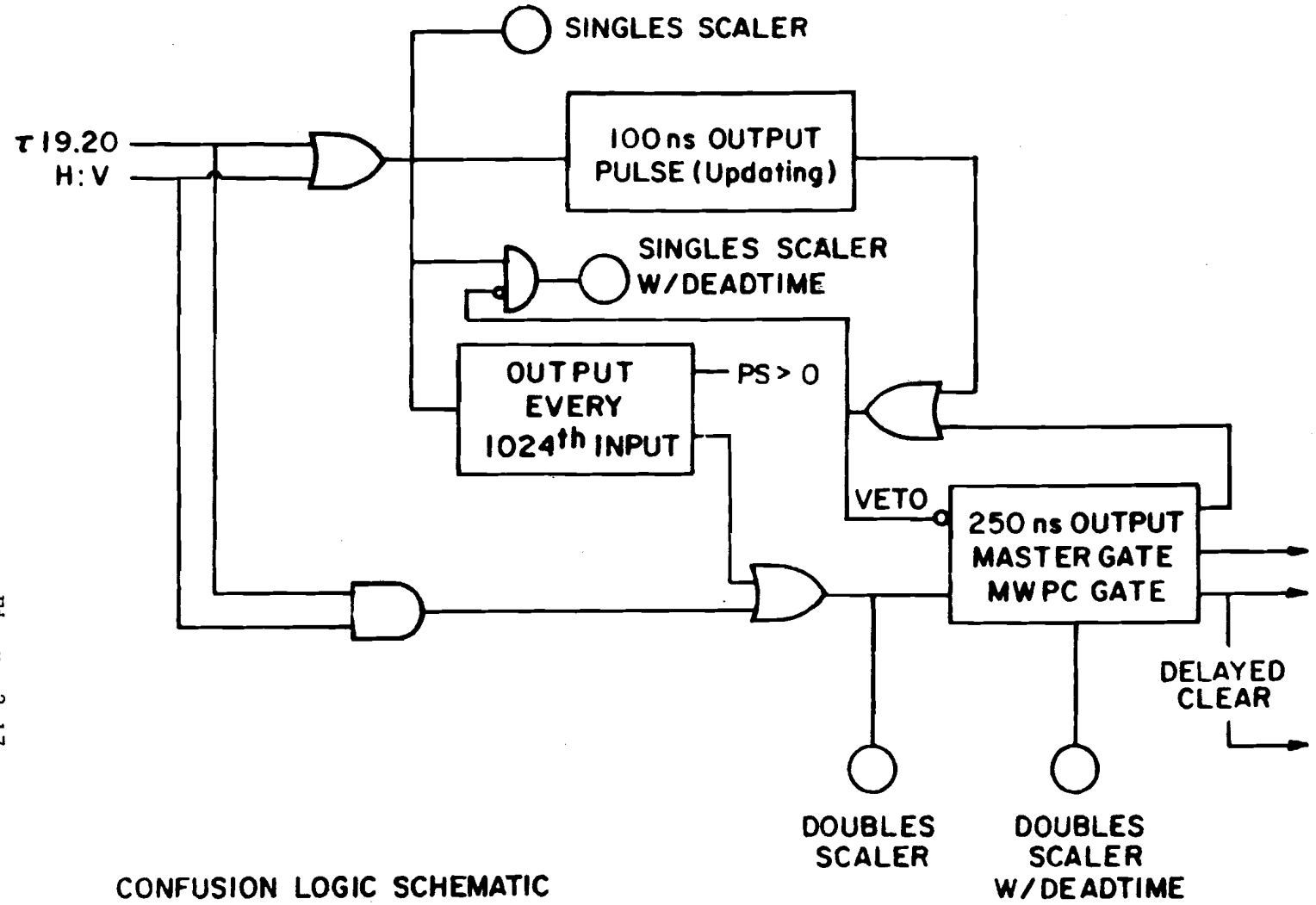

CONFUSION LOGIC SCHEMATIC

Figure 2.17

coincidences (MG>1 NDT) and the number of generated master gates (MG>1 DT) to compute the first part of the deadtime. Another pair of outputs, MG>0 NDT and MG>0 DT, performs the same function for the singles induced deadtime. The product of these two livetimes gives the total livetime of the master gate circuitry.

Once the master gate is generated, the MG module shuts itself off, as noted above, for 250 nsec to allow the DC logic time to process its information. If conditions are right for a trigger, the event is read out through ACE into the 64K buffer and a special computer busy level is set to block the readout of any other event satisfying the trigger requirements while the current event is still being handled. The deadtime resulting from such readout suppression is monitored by 2 outputs on each pin logic module which count the total number of triggers generated and the number of triggers read out. The ratio of these two numbers is the DC logic livetime.

The coincidence register rack was double buffered, allowing the DC logic to form triggers while previous events were being read out. The TRM logic (using MWPC band signal information), however, did not possess this double buffering scheme, hence the deadtime computed for triggers involving TRM's is meaningless. We assumed that this deadtime is the same as that for Pin 1, which is just the heavily prescaled (by 1024) master gate.

CHAPTER 3

ANALYSIS TECHNIQUES

The data used for this analysis were collected, with several brief interruptions, from December 1977 to May 1978. During that time the experiment wrote 24 million triggers on 1200 tapes, representing a total delivery of 7×10^{16} protons or 5×10^{11} photons having energies greater than 50 GeV. As mentioned at the beginning of chapter 2, we took an additional 300 tapes worth of data (6 million triggers) with 6 radiation lengths of lead inserted into the beam to monitor hadronic backgrounds.

The magnets M1 and M2 were run at opposite relative polarity to approximately focus the heavily produced e+e- pairs through the hole in C2, thereby minimizing their impact on the central mirrors. The absolute values for the vertical momentum kicks of the magnets were .401 GeV/c for M1 and .632 GeV/c for M2. Periodically during the course of the experiment the polarity of each magnet was reversed in such a way so that the focussing mode was always in effect.

Section A Data Reduction

The arrival in 1979 at Fermilab of the CYBER 175, with its attendant high disk storage and 6250 bpi tape drives, granted us increased computing power and the ability to store our data on a manageable number of tapes. The data were processed according to the following steps, each stage adding information to the last:

1. Pass 0 (1200 tapes ==> 191 tapes) All events with 200 or more hits in MWPC's, or having inconsistent information, were thrown out at this stage. The program then matched the MWPC wire and band regions for the surviving 95% of the events and only wrote out ADC's above threshold. The change from a 16 to a 60 bit format was also made at this time.

2. Reconstruction (191 tapes ==> 191 tapes) The track reconstruction program used MWPC wire information to construct tracks and find V^0's decaying downstream of P0 or P1.

3. Edit (191 tapes ==> 191 tapes) A collection of programs performed the following tasks: (1) Vertex determination; (2)TRM drift analysis; (3)Shower reconstruction; (4)V^0 finding; (5)Hadron identification via Cerenkov; (6)Muon tagging. The information obtained by each task was encoded and written to the output tape.

The same steps were performed for the background data and resulted in 50 tapes at each stage.

We then produced the following sets of summary tapes:

1. 1 K Edit (50 tapes, 13 background tapes) Required the presence of at least one charged K or P or a V^0 having $M_{\pi\pi}$ within 30 MeV of the K_S mass.

2. K_S Edit (8 tapes) Demanded a V^0 having a $\pi\pi$ mass within 30 MeV of the K_S.

3. Mass Edit (13 tapes) Required a charged K satisfying $M_{K\pi} > 1.5$ GeV/c^2 or $M_{K\pi\pi} > 1.5$ GeV/c^2 (to facilitate D search).

4. V^0 Edit (7 tapes) Demanded a V^0 with a $p\pi$ mass < 1.145 GeV/c^2.

5. 2 Heavy Edit (13 tapes) Insisted on the presence of a charged or neutral K plus at least one other heavy particle not including the Λ.

Section B Track Reconstruction

A reconstruction program, RCON, performed a pattern recognition algorithm on the raw MWPC wire addresses in order to construct track information. The method by which this was accomplished is described elsewhere {19,35}, hence we will only outline the type of information available and describe some of the cuts employed.

RCON supplies information for 3 basic types of tracks: full tracks, which pass through the second magnet; stubs, which do not; and V tracks, which begin downstream of P0 or P1. These cases are discussed below.

Full tracks, required to pass through 4 or 5 chambers, were the best resolved because they had an appreciable lever arm on both sides of M2. The program fitted each track of this class to the hypothesis that the X

projection (measuring the non-bend horizontal coordinate) formed a straight line while the vertical projection made a line with a "kink" at the center of M2. The resolution for these tracks is $\Delta P/P$ = 2.5% at P=100 GeV/c.

Stubs, which only left hits in the 3 chambers in front of M2, were fit to straight lines in both projections. In order to calculate the momentum for a track of this type, one must use the event vertex, which lies upstream of M1, in addition to the measured downstream line segment. The event vertex was obtained by intersecting full tracks, whose momenta were known, upstream of the magnet, taking proper account of the field asymmetries and weak focussing effects. The stub resolution $\Delta P/P$ is 7.5% at P=100 GeV/c. Fig. 3.1 graphically illustrates the difference in momentum spectra for full tracks and stubs.

Tracks in the third, or V, category were reconstructed in pairs under the hypothesis that they intersected downstream of P0 or P1. One of the 2 tracks was required to make a hit downstream of M2 and pass through at least 3 MWPCs to insure momentum information. The other track had to hit a minimum of 2 upstream MWPCs or 1 upstream and 2 downstream chambers.

Section C Edit Analysis

We will review in this section the techniques employed by the following analyses in obtaining the final set of 191 tapes: (1) TRM drift measurement; (2) Vertex determination; (3) V^0 algorithm; and (4) Shower reconstruction. Because of its importance, particle identification via the Cerenkov system will be discussed in Section D, whereas the muon tagging algorithms, unrelated to this thesis, are left to ref. 36.

TRM Information

After reconstruction, a program utilizing the TRM drift time information attempted to improve the momentum measurement of the tracks. Ref. 19

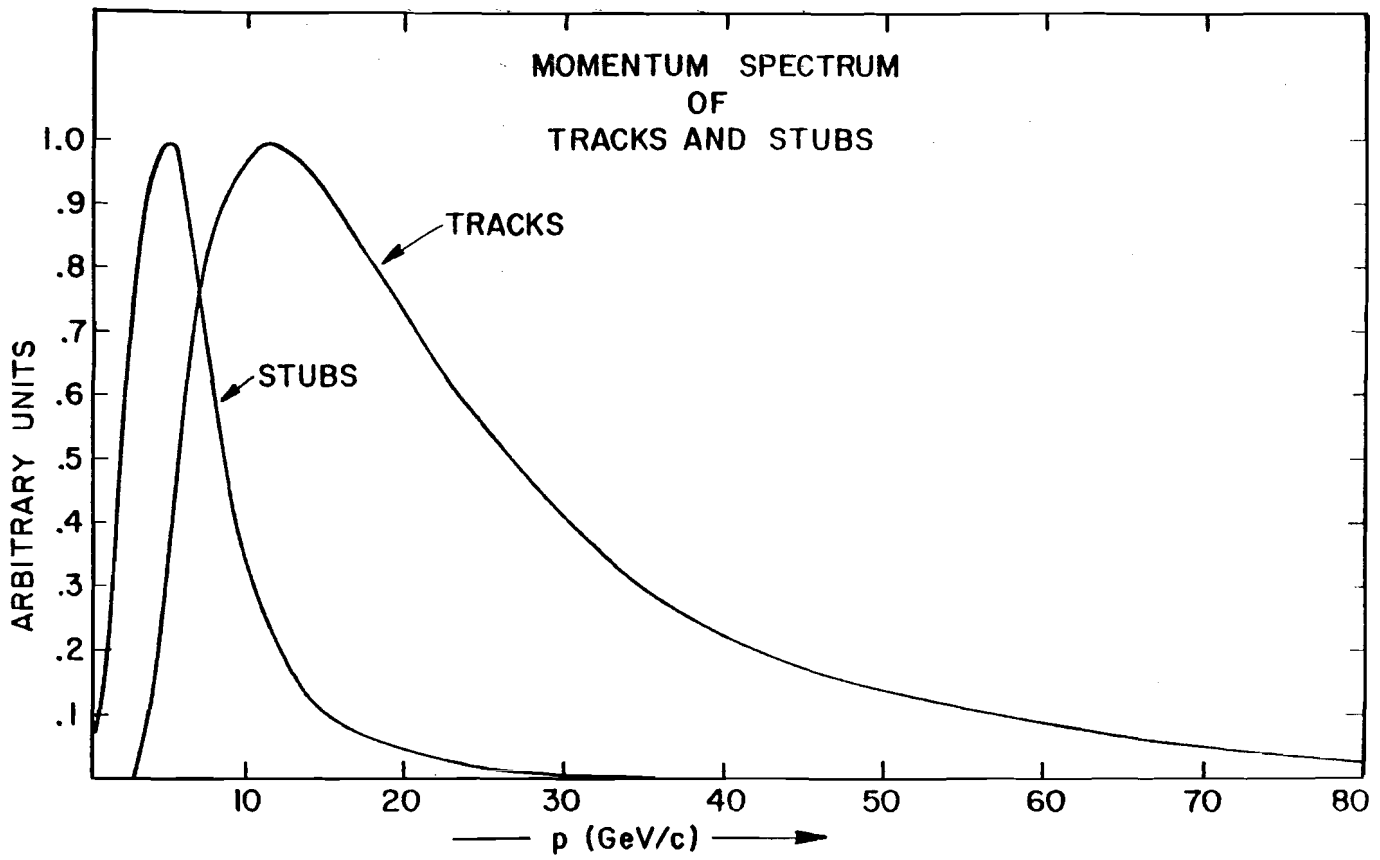
MOMENTUM SPECTRUM
OF
TRACKS AND STUBS
TRACKS
STUBS
ARBITRARY UNITS
1.0
.9
.8
.7
.6
.5
.4
.3
.2
.1
10
20
30
40
50
60
70
80
p (GeV/c)

Figure 3.1

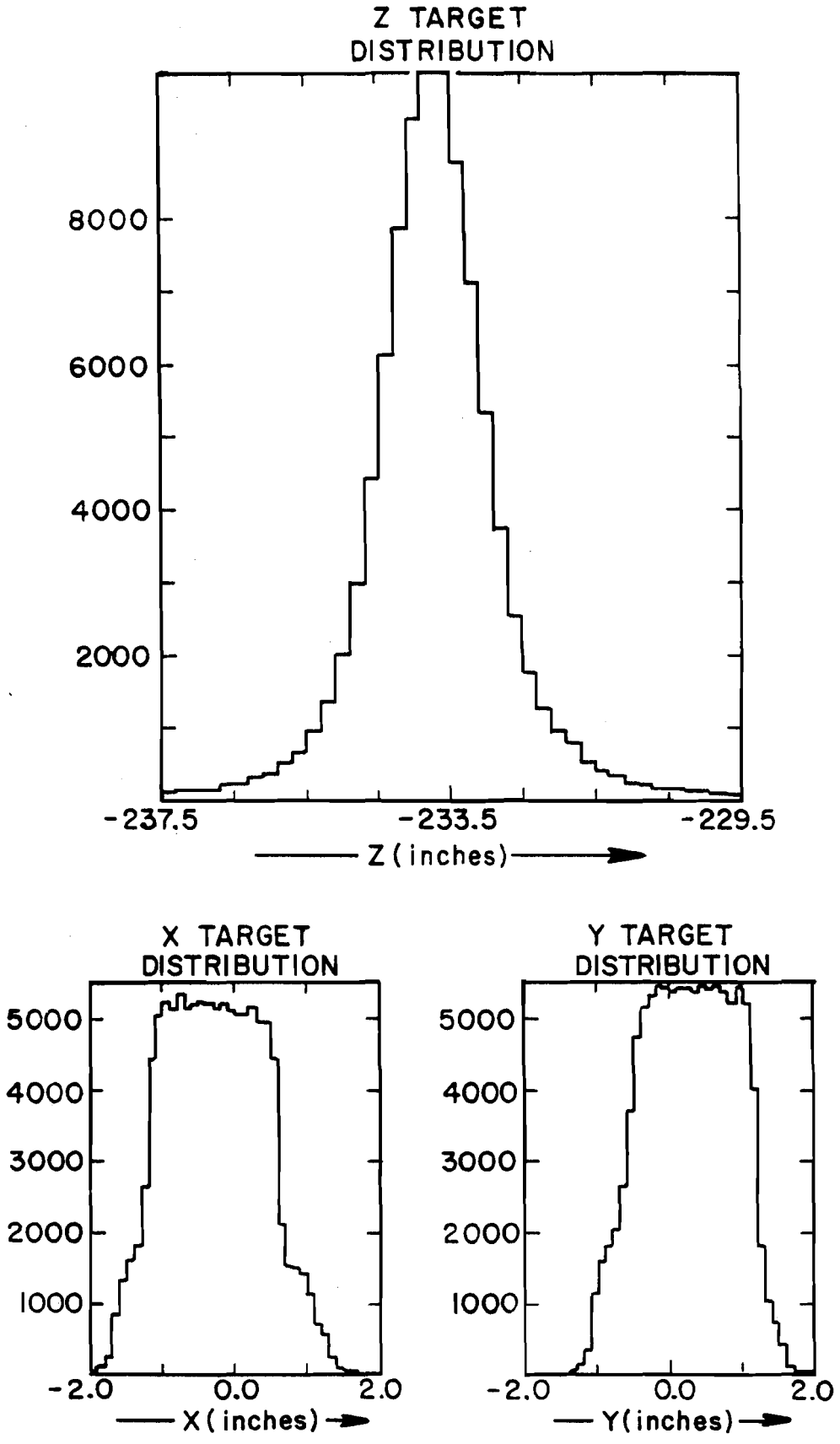
Z TARGET
DISTRIBUTION
8000
6000
4000
2000
-237.5
-233.5
-229.5
Z (inches)
X TARGET
DISTRIBUTION
5000
4000
3000
2000
1000
-2.0
0.0
2.0
X (inches)
Y TARGET
DISTRIBUTION
5000
4000
3000
2000
1000
-2.0
0.0
2.0
Y (inches)

Figure 3.2

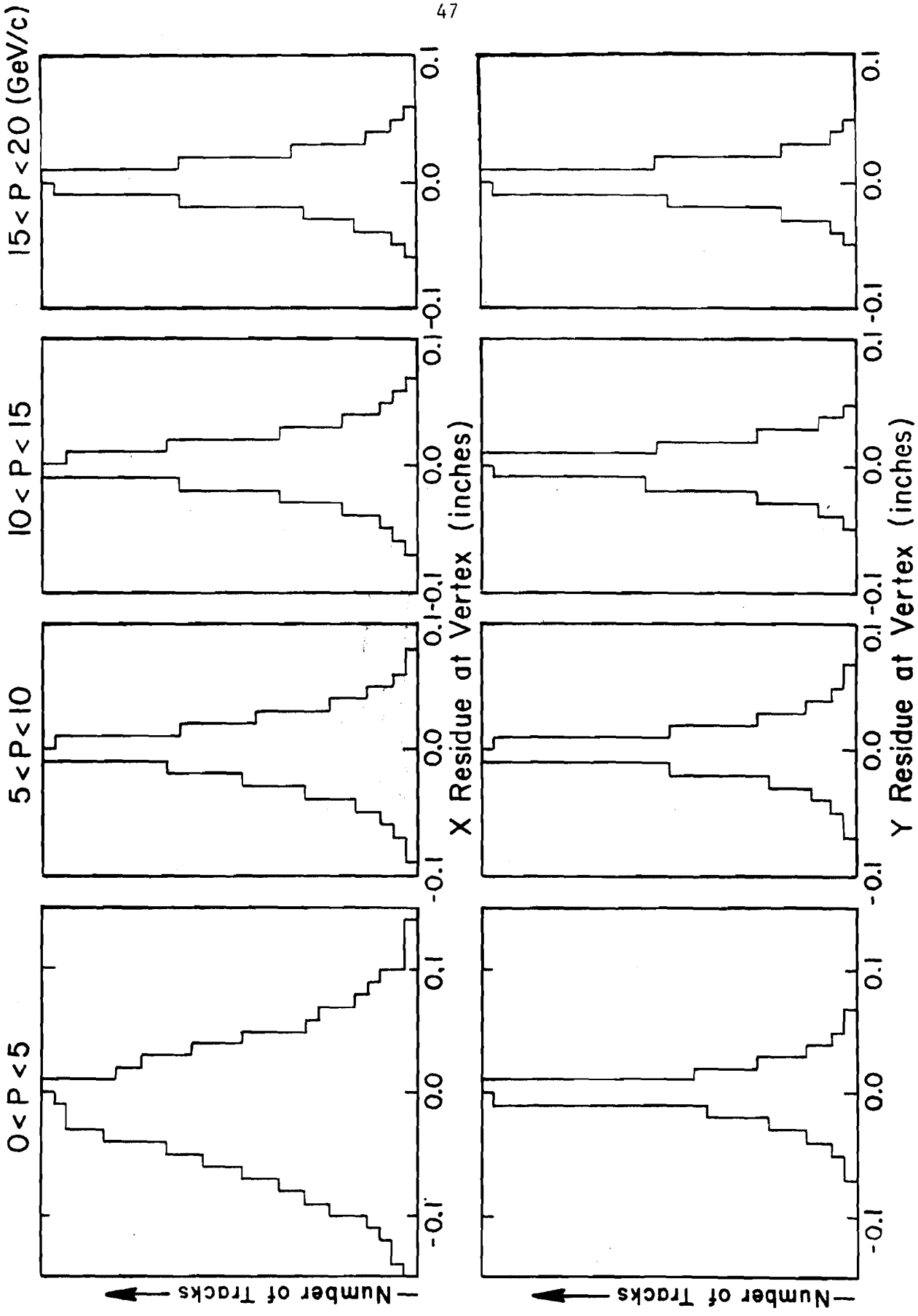
0<P<5
5<P<10
10<P<15
15<P<20 (GeV/c)
Number of Tracks
X Residue at Vertex (inches)
Y Residue at Vertex (inches)
-0.1
0.0
0.1

Figure 3.3

contains a complete exposition of the techniques necessary to exploit this information.

Vertex Determination

The vertex finding routines had the capability of resolving several vertices within an event, labeling the one with the most tracks emerging from it as the primary vertex. Typical distributions for the x,y, and z components of the vertex are shown in fig. 3.2. Most of the secondary interaction points were due to the presence of another photon in the event converting to an e+e- pair. The assignment of a given track to a vertex required that it satisfy a distance of closest approach criterion given by:

Full tracks	DCA < .122"	
Stubs	DCA < .15"	(Measured only in non-bend plane)

Distributions of the x and y residues at the vertex for tracks and stubs of various momenta are shown in fig. 3.3.

V^0 Reconstruction

Since most of the Λ's and K_S's decayed inside the first magnet, V^0's were initially identified by searching for pairs of tracks intersecting downstream of the target in the non bend plane. The action then taken depended strongly on the nature of the tracks involved {19}. In the end, 7 types of V^0's of various quality were found:

1. Downstream. These are V^0's decaying downstream of P0 or P1 where both tracks pass through M2. The tracks were fit to the hypothesis that they intersected at a point.

2. Track-Track. These were composed of two full tracks, one of which had to be unassigned to the target. The tracks must pass within .15" of each other.

3. Track-Stub. These were composed of 1 full track and 1 stub, one of which must be unassigned to the target.

4. Downstream with Short Stub. The V^0 decays in back of P0. One track

must pass through M2 and the other must hit P1 and P2.

5. Downstream Assigned. Same as case 1 but with a looser criterion for MWPC hit sharing.

6. Track-Track Both Assigned. Same as case 2 where both tracks were assigned to target.

7. Track-Stub Both Assigned. Same as case 3 where both tracks were assigned to target.

The $\pi\pi$ and $P\pi$ mass distributions for each of the 7 types of V^0's are shown in fig. 3.4 and 3.5.

Shower Analysis

The shower finding routines operated independently of any charged track information, the only inputs being the energy deposition in each of the lead glass blocks. The algorithm first isolated the block possessing the largest amount of energy and defined a 3 x 3 array with the "hot" block in the center. This 9 element array was further subdivided into 4 quadrants of 4 blocks apiece, each quadrant containing the central cell, which were scanned to find the one with the most total energy subject to a "diagonal" rule. This rule demanded that the diagonal neighbor of the central block have less energy than the two side neighbors.

Having a quqdrant identified, the program then removed its constituents from the list of available blocks and proceeded to calculate the x and y position of the shower using as input the fraction of energy on either side of the 2 orthogonal cracks dividing the quadrant. A shower sharing formula developed in ref. 37 translated each of these fractions into a position relative to the corresponding crack.

The entire process described above was repeated until no available blocks were left with energy deposition above .8 GeV. If, along the way, any potential shower nucleus (i.e. "hot" block) was found to be adjacent to a

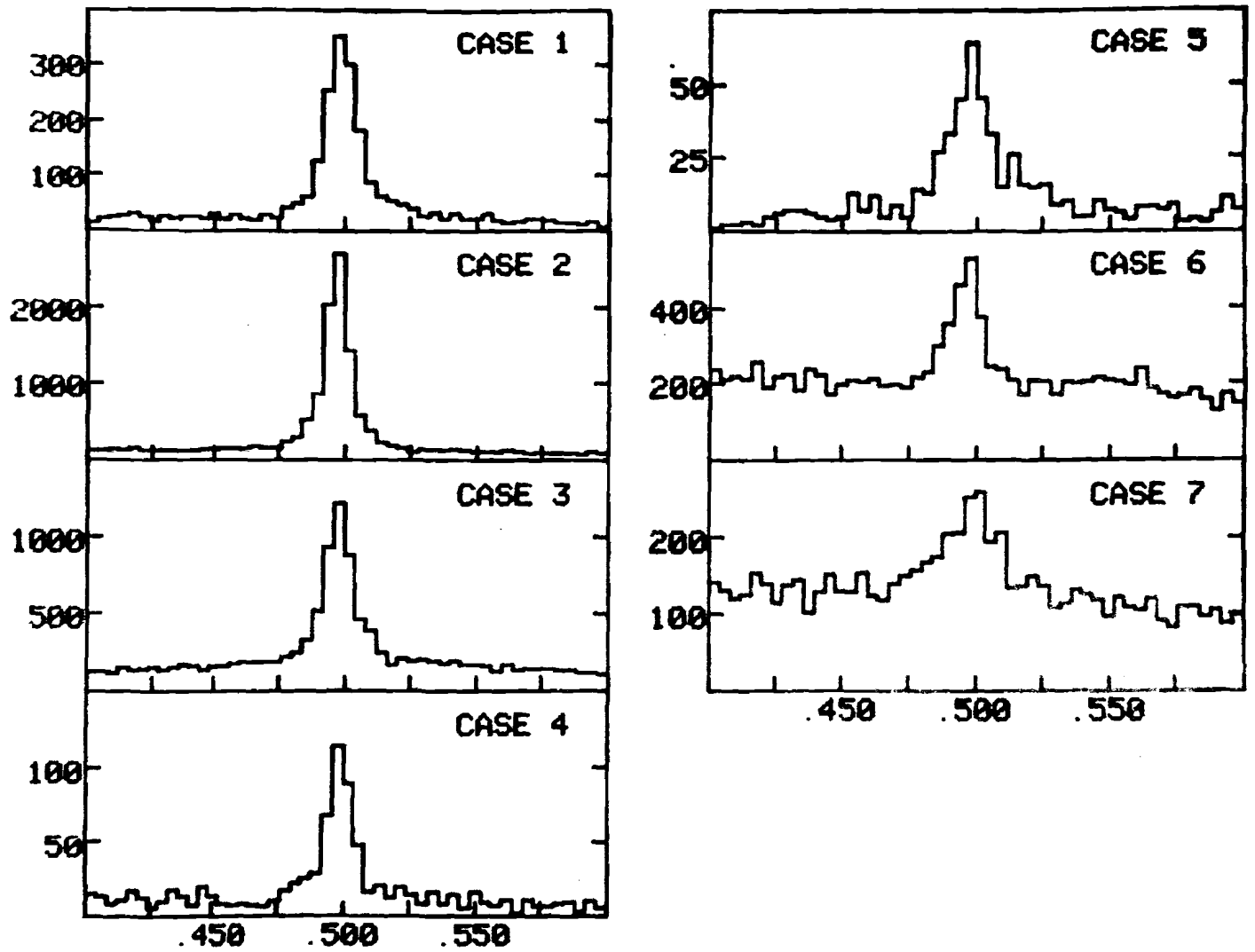

PIPI MASS VS CASE FOR ALL V^0 CANDIDATES

Figure 3.4

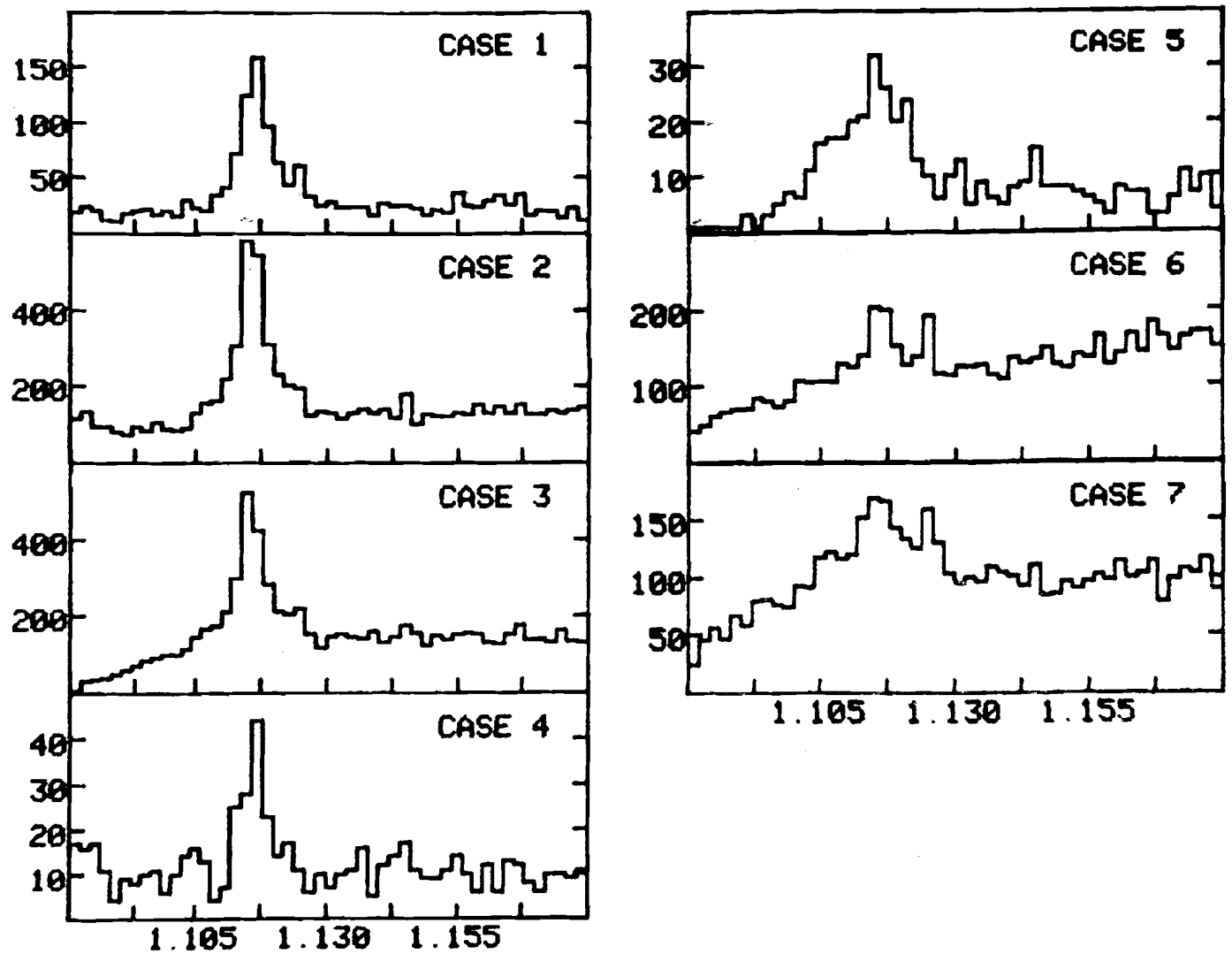

PPI MASS VS CASE FOR ALL V^0 CANDIDATES

Figure 3.5

previously determined shower, the algorithm incorporated the block's energy into the shower and removed it from the pool of available blocks.

Section D Cerenkov Identification

The Cerenkov routines began by calculating for each track the light fractions on every mirror for 4 particle hypotheses: electron, pion, kaon, and proton. Matters were somewhat complicated for C1 because the magnetic field of M2 bent the tracks into circular trajectories, leading to a teardrop shaped light distribution at the mirror plane. The light sharing algorithm approximated a solution by summing the contributions from 10 equally spaced points along the path.

The mirror fractions and Cerenkov tube ADCs were inputs to a program called CANAL which determined the particle identification by an iterative process. First, CANAL called the routine PARTP2, described below, which examined the C2 information using the current set of particle assignments (to determine the proper light allocation). PARTP2 then returned a number called the KCTK code, defined as:

KCTK = 0	Mirrors off for track
KCTK = 1	Mirrors on for track
KCTK = 2	Too much confusion from other tracks
KCTK = 3	Track misses mirrors

Every track was initialized to KCTK = 2 at the start of the event. CANAL then made a first estimate of the particle type, e, π, K, or P, and called PARTP1, which used this guess as input, along with the light fractions and ADC information, to determine the corresponding KCTK code for C1. The particle type was calculated again by CANAL in light of this new information and the loop was repeated until either the KCTK codes stopped changing or 4 iterations had elapsed. The algorithm rarely required more than the minimum of 2 iterations.

PARTP1 (PARTP2) determined the KCTK code for C1 (C2) by only looking at tracks with KCTK = 2, which meant that once a track was determined to be OFF or ON (KCTK = 0 or 1) its status could not be changed. The program compiled for each track a list of so-called "isolated" mirrors which were required to overlap the track's light cone and intercept no more than .2 photons from all other sources. If any one of these mirrors had an ADC count of 10 or more, it was considered to be on and the KCTK code was set to 1 (ON) for the track. Otherwise, the expected light yield for all off mirrors (ADC < 10), isolated or not, was summed, and if greater than 2.5 photons, the KCTK code for the track was set to 0 (OFF).

CANAL calculated for each track a number, called the ID, which was determined from the particle momentum and the KCTK codes (see table 3.1). It is defined by the table below.

ID = -2	Total confusion, KCTKs are either 2 or 3
ID = 0	Electron
ID = 1	Pion
ID = 2	Kaon
ID = 3	Proton
ID = 4	Electron, pion, or kaon
ID = 5	Kaon or proton (K/P)
ID = 6	Pion, kaon, or proton
ID = 7	Pion, kaon, or proton
ID = 9	Electron, pion, kaon, or proton

The e:π:K:P breakdown for our data is approximately 5:75:13:12, with most of the K and P production resulting from the K_L and neutron beam components respectively.

Section E Analysis Programs

The set of 191 data tapes produced by these programs provided the basis for the analysis effort described in this section. The routines organized the available information into a coherent picture by confronting the following issues: (1) V^0 cleanup; (2) Track association to vertex or V^0 ;

Table 3.1

CHERENKOV IDENTIFICATION TABLE

C2 / C1	OFF			ON			DON'T KNOW			
	OFF	ON	DON'T KNOW	OFF	ON	DON'T KNOW	OFF	ON	DON'T KNOW	
00										
	π/K/p	?	π/K/p	?*	e	e	π/K/p	e	?	
5.9										$C1_\pi$
	K/p	π	π/K/p	?*	e	e	K/p	π	?	
10.7										$C2_\pi$
	K/p	π*	K/p	π*	π	π	K/p	π	?	
20.7										$C1_K$
	p	K	K/p	π*	π	π	p	π/K	?	
37.4										$C2_K$
	p	K	K/p	π/K*	π/K	π/K	p	π/K	?	
39.3										$C1_p$
	p	p	p	π/K*	π/K	π/K	?	?	?	
70.9										$C2_p$

*C1,C2 DO NOT AGREE

(3) Formation of photons from lead glass showers; and (4) Calculation of event properties. Each of these topics is discussed below.

V^0 Cleanup

The V^0 cleanup algorithm, schematically outlined in fig. 3.6, demanded that a V^0 meet certain criteria before being classified as a "good" K_S or Λ. A V^0 was not even considered to be a candidate unless it had a $\pi\pi$ mass within 15 MeV of the K_S or a $P\pi$ mass within 10 MeV of the Λ. The $\pi\pi$ mass distributions for V^0's before and after the cleanup are displayed in fig. 3.7. Although V^0's that did not satisfy the cleanup algorithm were included in the appropriate particle lists (and hence allowed into mass plots), they could not contribute to quantities calculated for the event as a whole, such as total mass, visible energy, etc.

Track Assignment

Every track was classified into one of the following 3 categories:

1. Assigned to target. The track must be assigned by the edit program to the primary vertex and not be part of any V^0 satisfying the cleanup criteria.

2. Assigned to V^0. The track is a component of a V^0 satisfying cleanup criteria.

3. Unassigned

Only tracks in the first category were allowed to make direct contributions to event quantities and mass plots; those in the second were represented by the parent V^0. Unassigned tracks, which account for only a few per cent of all tracks, were ignored in the data analysis performed in this thesis.

Photons

Many of the showers found by the algorithm described in section D were generated by hadronic interactions in the lead glass. We considered a shower

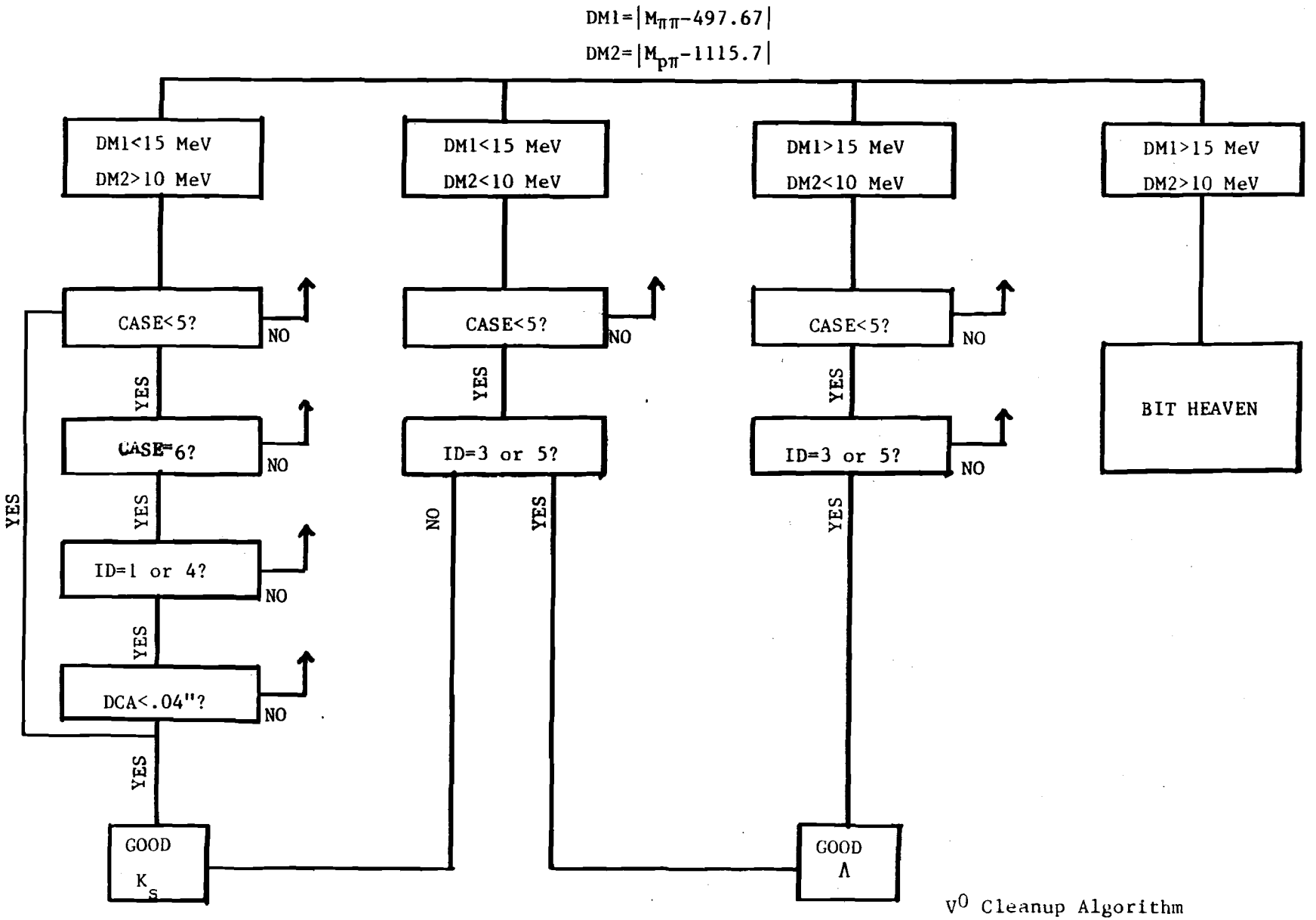

Figure 3.6

V^0 Cleanup Algorithm

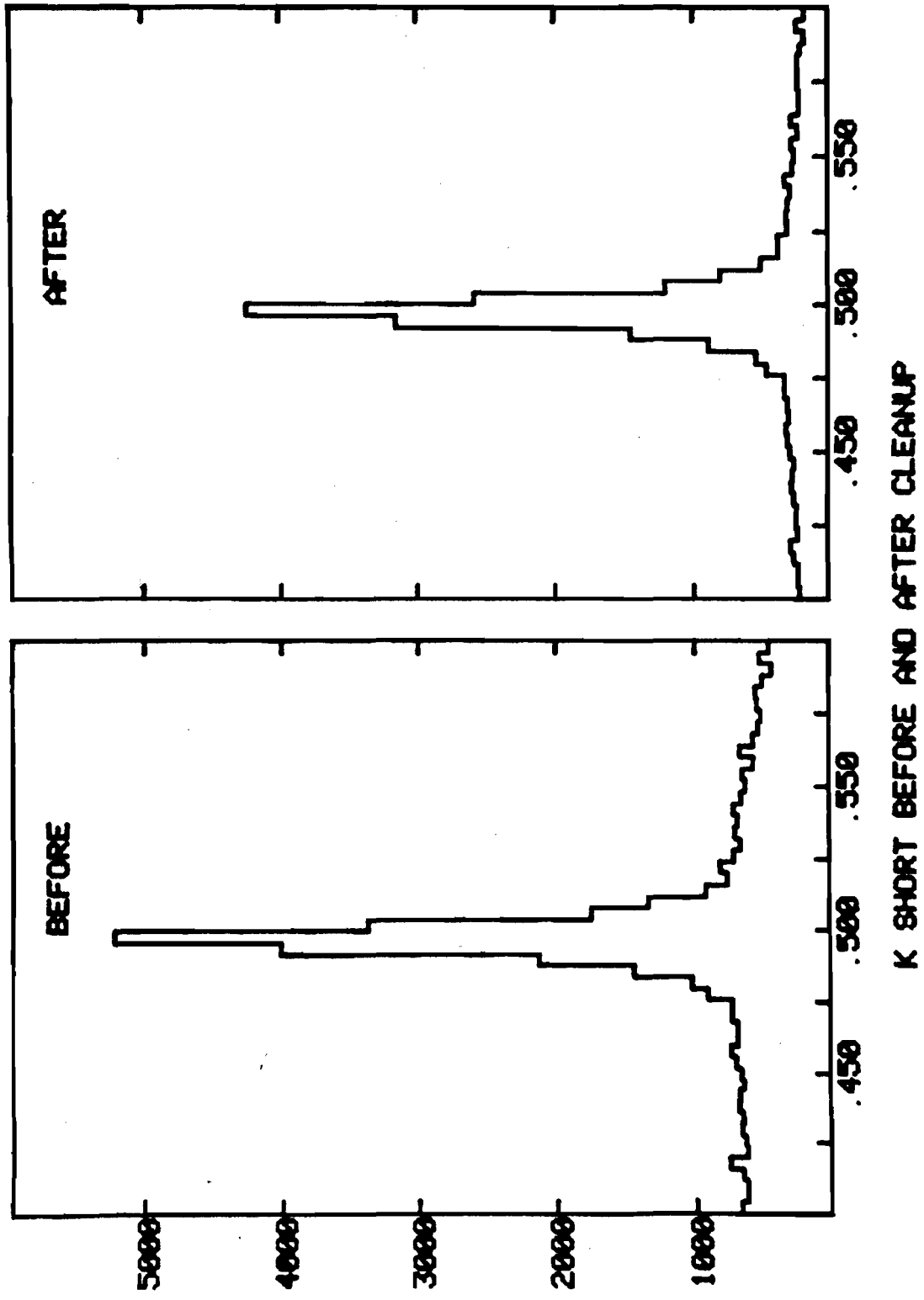
BEFORE
AFTER
5000
4000
3000
2000
1000
.450
.500
.550
K SHORT BEFORE AND AFTER CLEANUP

Figure 3.7

to be unassociated with a track if the distance between the track and the shower (DCA) was greater than some minimum separation, the value chosen depending on shower energy as follows:

DCA > 5"	$0 < E_{sh} < 10$ GeV
DCA > 3"	$10 < E_{sh} < 20$ GeV
DCA > 2"	$E_{sh} > 20$ GeV

Any unassociated shower with energy greater than 1.5 GeV was considered to be a photon with a 4-momentum calculated from its energy and position relative to the primary vertex.

Calculation of Event Properties

A consistent set of rules must be employed when calculating variables such as total energy, mass, multiplicity, etc. A problem might arise, for example, if a particle is allowed to contribute twice to these quantities, once as a track and again as part of a V^0.

Only the following are allowed to make contributions to event quantities: charged tracks assigned to the target, V^0's passing the cleanup criteria, and photons satisfying the requirements posed above. An ambiguity can arise, however, because it is not clear what mass should be assigned to particles labeled as K/P (ID = 5) by the Cerenkov algorithm. We resolve this issue via the following strategem: assign the kaon mass to the particle in question during a meson search and assign the proton mass during a baryon search.

Finally, the absolute currents in the magnets were adjusted to give the $\psi(3095)$ its proper mass. The necessary shifts employed were less than 1%.

CHAPTER 4

DETECTOR PERFORMANCE

The last two chapters have presented considerable detail regarding the E-87 detector and analysis software. We complement that description below with a discussion of the detector performance in two critical areas, Cerenkov identification and trigger efficiency, and apply this knowledge in the next chapter to calculate detection efficiencies for charmed particle final states.

Section A Cerenkov Identification

We begin by discussing: (1) mirror geometry, (2) thresholds, (3) photon yield, and (4) sensitivity of the phototubes and ADCs.

The boundary between two adjacent mirrors was determined by plotting the fraction of the time that both mirrors were on versus the position of the track relative to the edge. If we call f the fraction of light on one mirror and n the average photon yield per track, then the probability that the mirror is off is given by the Poisson formula:

$$P_{off} = \exp(-fn)$$

where the fraction f can be calculated using the distance x from the center of the light cone to the edge of the mirror by

$$f(x) = 1 - \frac{\cos^{-1} d}{\pi} + \frac{d}{\pi} \log(1/d + \sqrt{(1/d^2 - 1)})$$

using d=(x-b)/R, where R is the light cone radius and b is the mirror boundary. Given these relations, we can write down the probability that both mirrors are on if the light is contained on both of them as:

$$P(x) = \{1-\exp(-fn)\}\{1-\exp(fn-n)\}$$

This probability is maximized when the fractions of light on each mirror are equal or, equivalently, when the track hits the mirror boundary. The mirror

location can be determined by fitting the corresponding efficiency plot (an example is shown in fig. 4.1) for the parameter b using the formula derived above. The mirror positions obtained by this technique are typically accurate to .1"-.2".

The above procedure was implemented for C2 by means of special e+e- runs performed over the course of the experiment. In the case of C1, single muon events were employed with a light baffle inserted in the gas radiator to reduce the light cone radius by about a factor of 4. M2 was turned off at this time to eliminate light smearing problems caused by the bending of tracks.

The hadron thresholds were obtained by plotting, as a function of momentum, the fraction of times that a fully contained track (light on one mirror) causes its target mirror to be on. Figs. 4.2 and 4.3 show efficiency curves for C1 and C2 averaged over all mirrors in each device. The pion thresholds determined from these plots are 5.85 and 10.7 GeV/c for C1 and C2 respectively.

The mirror pulse height spectra, obtained during the same electron runs, provided information on the photon yield per track and the mirror calibration constants (ADC counts/photon). These distributions were fit to the formula:

$$f(x) = N\Sigma_n \frac{\mu^n}{n!} e^{-\mu} (2\pi n\sigma^2)^{-\frac{1}{2}} \exp\{(x-nH)^2/2n\sigma^2\}$$

where
N = total number of events
μ = photon yield
H = ADC counts per photon
σ = resolution of phototube
x = pulse height

A typical pulse height distribution and its fit are shown in fig. 4.4.

Unfortunately, there were not enough statistics from the e+e- calibration to determine the above constants for every mirror. This

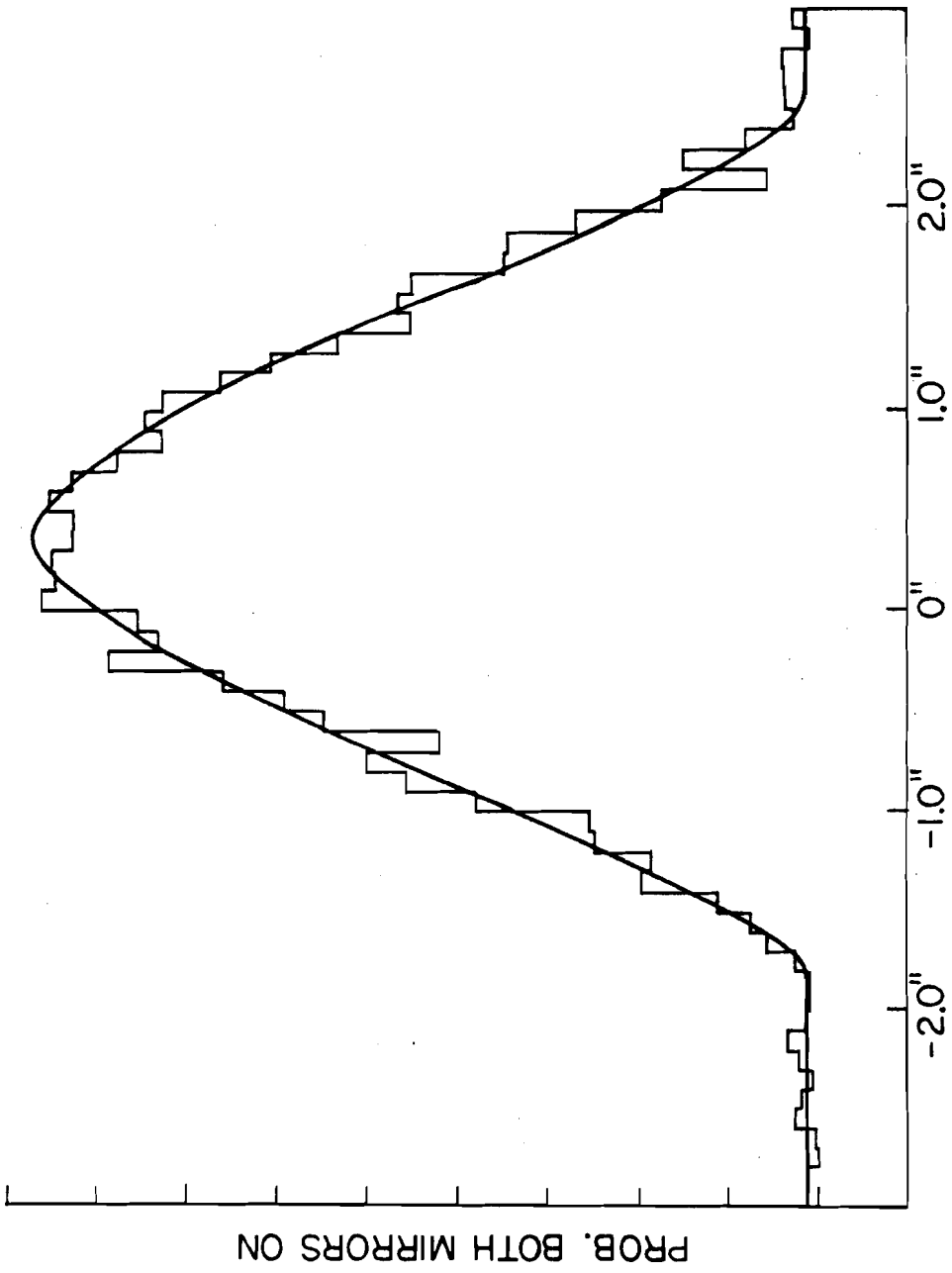

Example of Fit Used to Obtain Mirror Positions

Figure 4.1

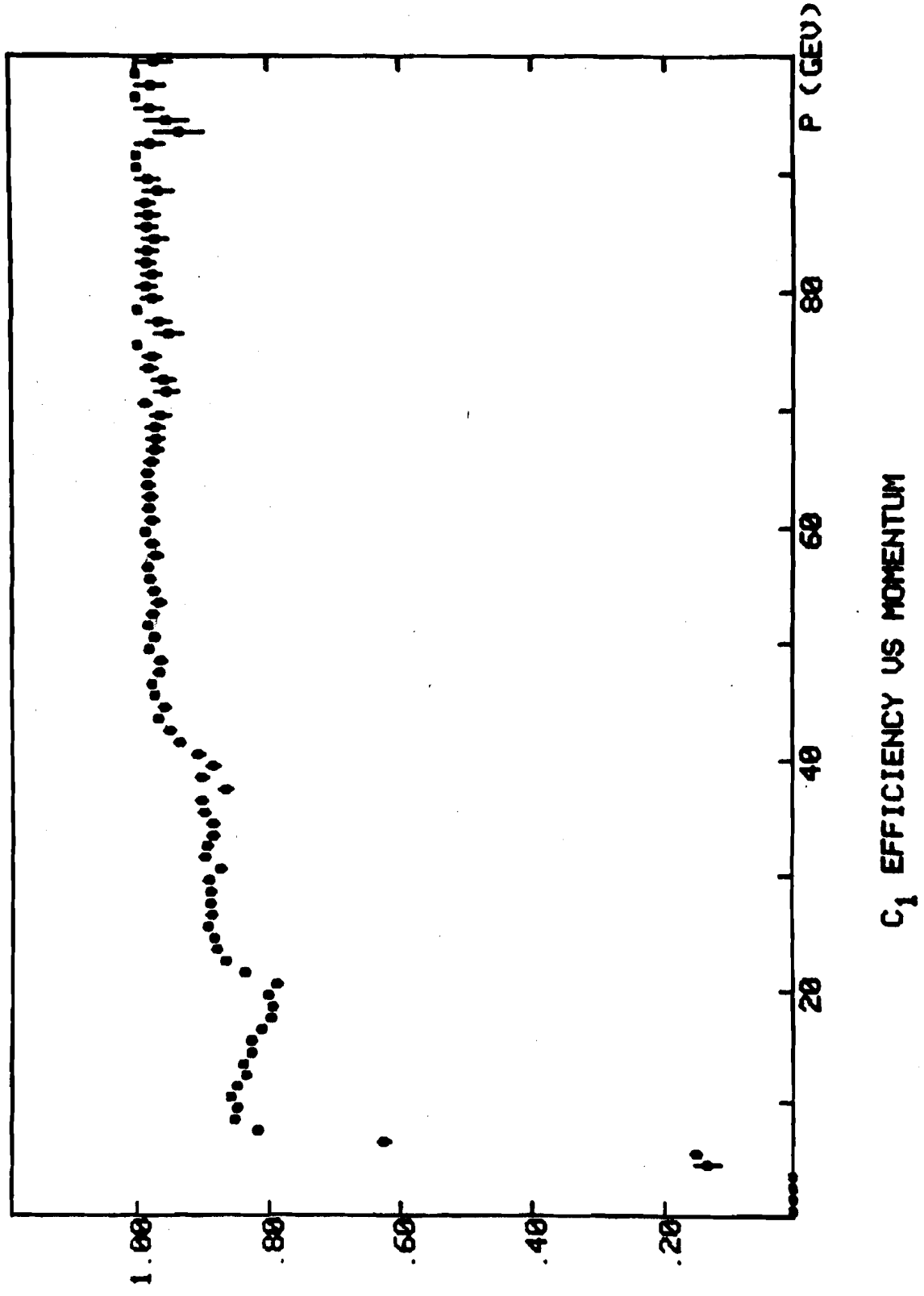

Figure 4.2

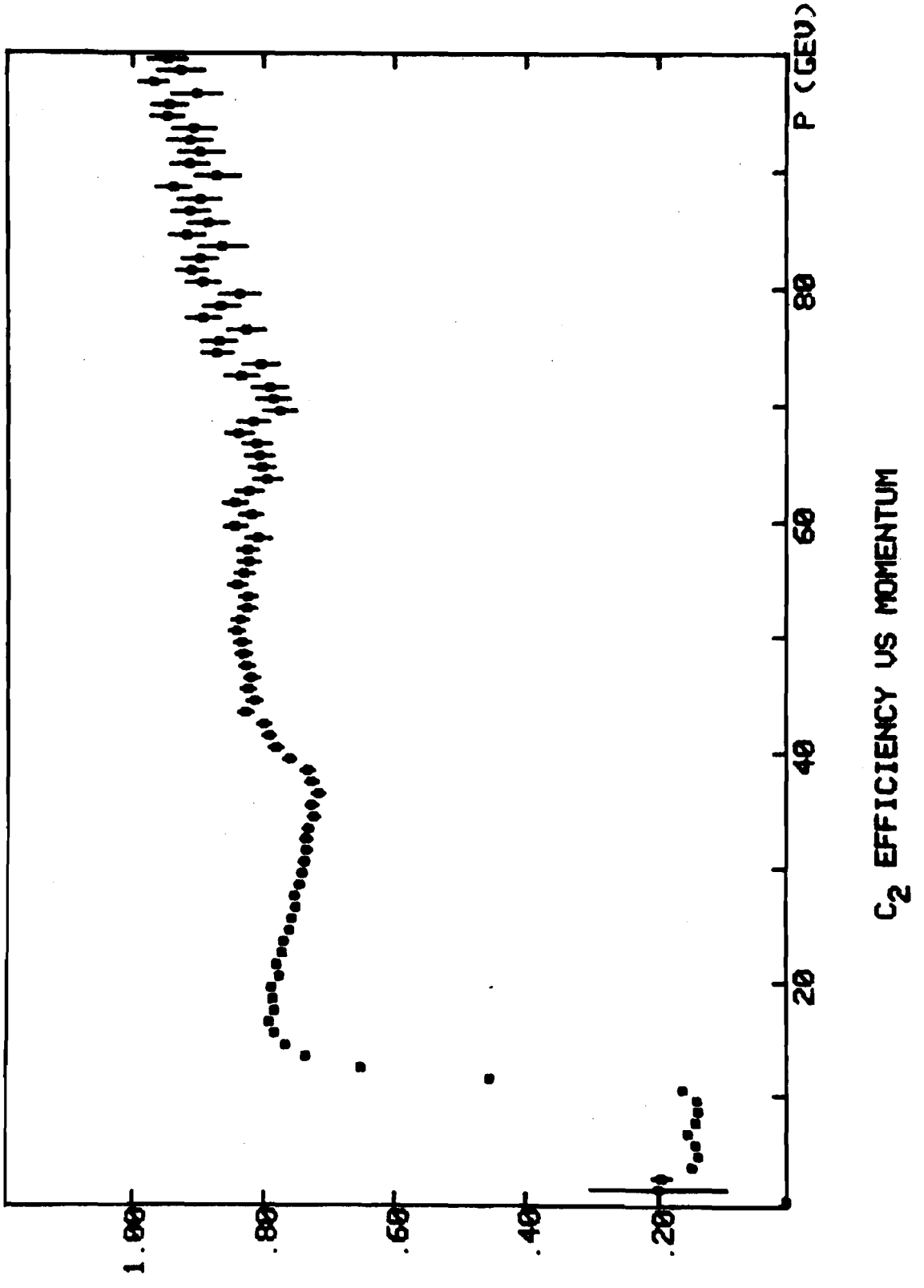

Figure 4.3

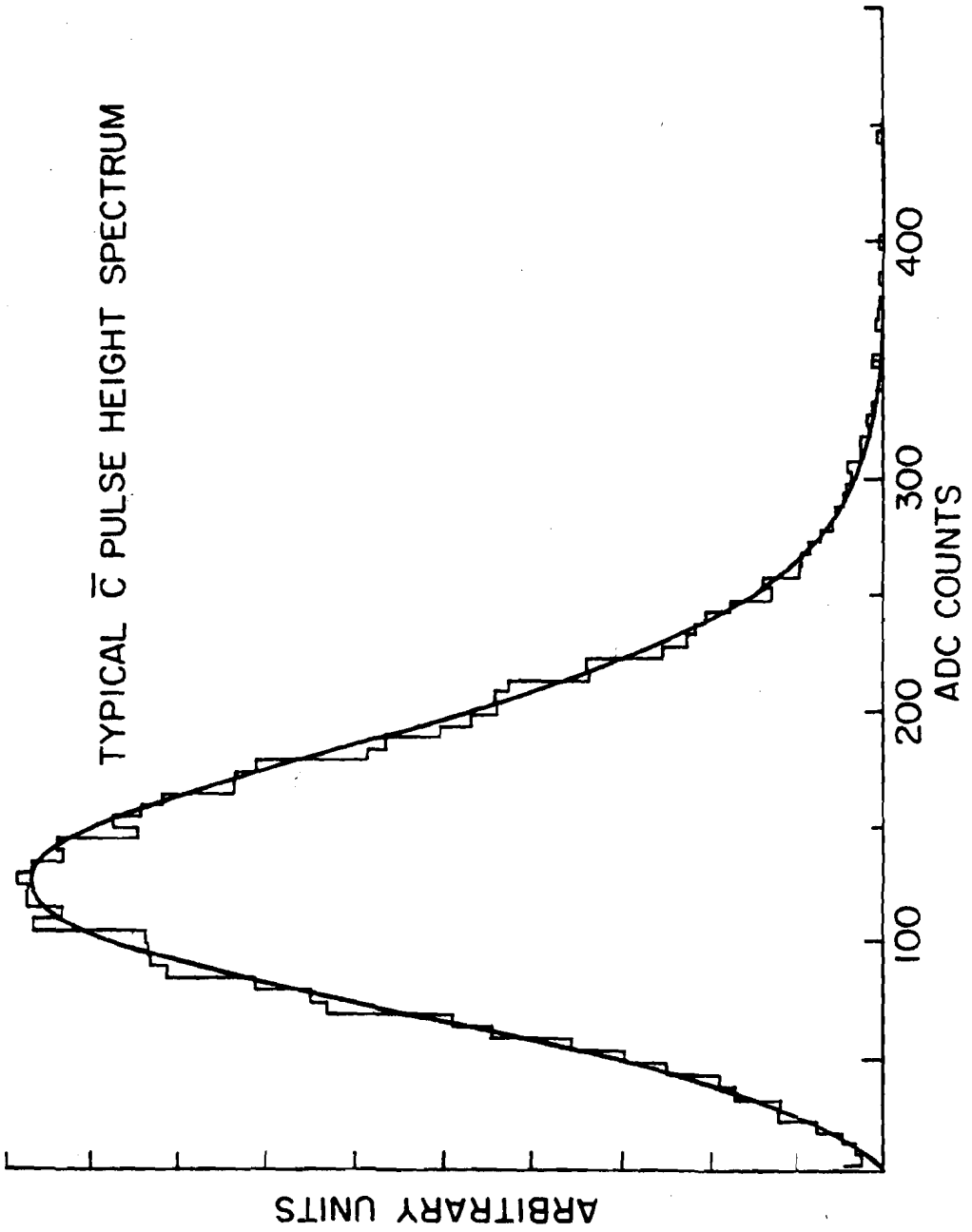
TYPICAL $\bar{C}$ PULSE HEIGHT SPECTRUM
ARBITRARY UNITS
100
200
300
400
ADC COUNTS

Figure 4.4

necessitated the use of a slightly different algorithm employing the same data. We chose representative values of the photon yield μ, 8 for C1 and 6 for C2, and determined the average calibration for each mirror from the relation:

$$H = \Sigma Y_i / \Sigma \mu_i$$

where Y_i is the pulse height for a given mirror and μ_i is the expected number of photons from all sources on that mirror. Each sum was performed over a subset of events for which the electron had at least half of its light on the mirror. The resolution parameter σ was estimated using the values obtained for mirrors which had their pulse height distribution fit in the manner described previously, and which had calibration constants H similar to the mirror under study.

The estimated values for H and σ for each of the 28 mirrors in the Cerenkov system are shown in the table below. A knowledge of these parameters is essential for determining the detector efficiency for final states requiring Cerenkov identification.

Cerenkov Sensitivity and Resolution Constants (ADC counts/photon)

	C1		C2	
	H	σ	H	σ
1	15	10	28	16
2	48	24	29	16
3	30	15	24	15
4	14	10	22	15
5	40	20	21	10
6	43	20	37	20
7	36	20	38	15
8	11	8	22	15
9	10	8	22	15
10	72	30	19	10
11	20	12	28	14
12	10	8	26	15
13			14	10
14			10	9
15			12	9
16			10	9

We are now in a position to demonstrate pictorially that the Cerenkov system actually does provide hadron separation. Figs. 4.5 and 4.6 show the $K\pi$ and KK mass distributions for events where the K is identified by the Cerenkov algorithm (K or K/P). Clear K^* and ϕ signals are present in their respective plots, culled from about 1.5% of the data sample. The $P\pi$ mass histograms for V^0's before and after a cut is applied demanding that the faster track be consistent with being a proton (P or K/P) are shown in fig. 4.7. It is obvious that the heavy particle requirement selects out a very pure sample of Λ's with little contamination.

In order to understand the detection efficiency for final states involving a charged K, it is important to know the fraction of the time that the K is identified by the Cerenkov system. Although this identification probability depends critically on details such as the disposition and momenta of tracks in the detector, which are taken into proper account in Monte Carlo simulations (Chapter 5), we can estimate its average size by determining the percentage of times that a known kaon is called OFF (no light on mirror) by C1 or C2 in the momentum region between pion and kaon threshold. For the real K sample we use K^*'s and ϕ's obtained from fits to the $K\pi$ and KK invariant mass distributions respectively. The efficiency for K identification can then be written as N2/N1, where N1 is the number of K^*'s (or ϕ's) in the momentum region defined above, and N2 is the number of K^*'s for which the Cerenkov counter registers an OFF. Fig. 4.8 shows the $K\pi$ and KK mass distributions in the K momentum region $7 < P < 21$ GeV/c before and after the C1 tagging. The corresponding histograms for C2 are displayed in fig. 4.9. The only requirements imposed on these data are that both particles must pass through the entire detector (full tracks) and that the event must contain 6 or fewer tracks.

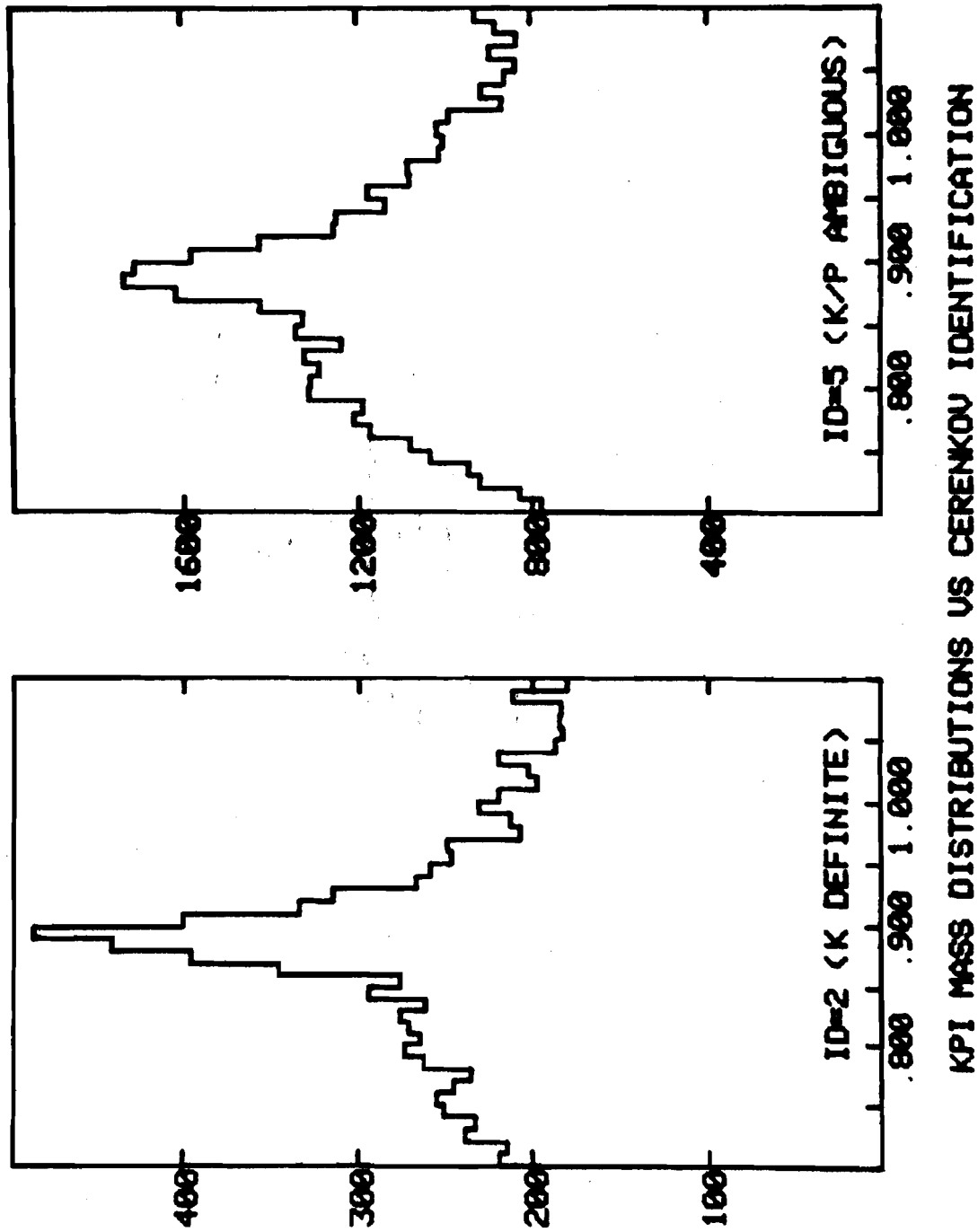
ID=2 (K DEFINITE)
ID=5 (K/P AMBIGUOUS)
KPI MASS DISTRIBUTIONS VS CERENKOV IDENTIFICATION
.800
.900
1.000
100
200
300
400
400
800
1200
1600

Figure 4.5

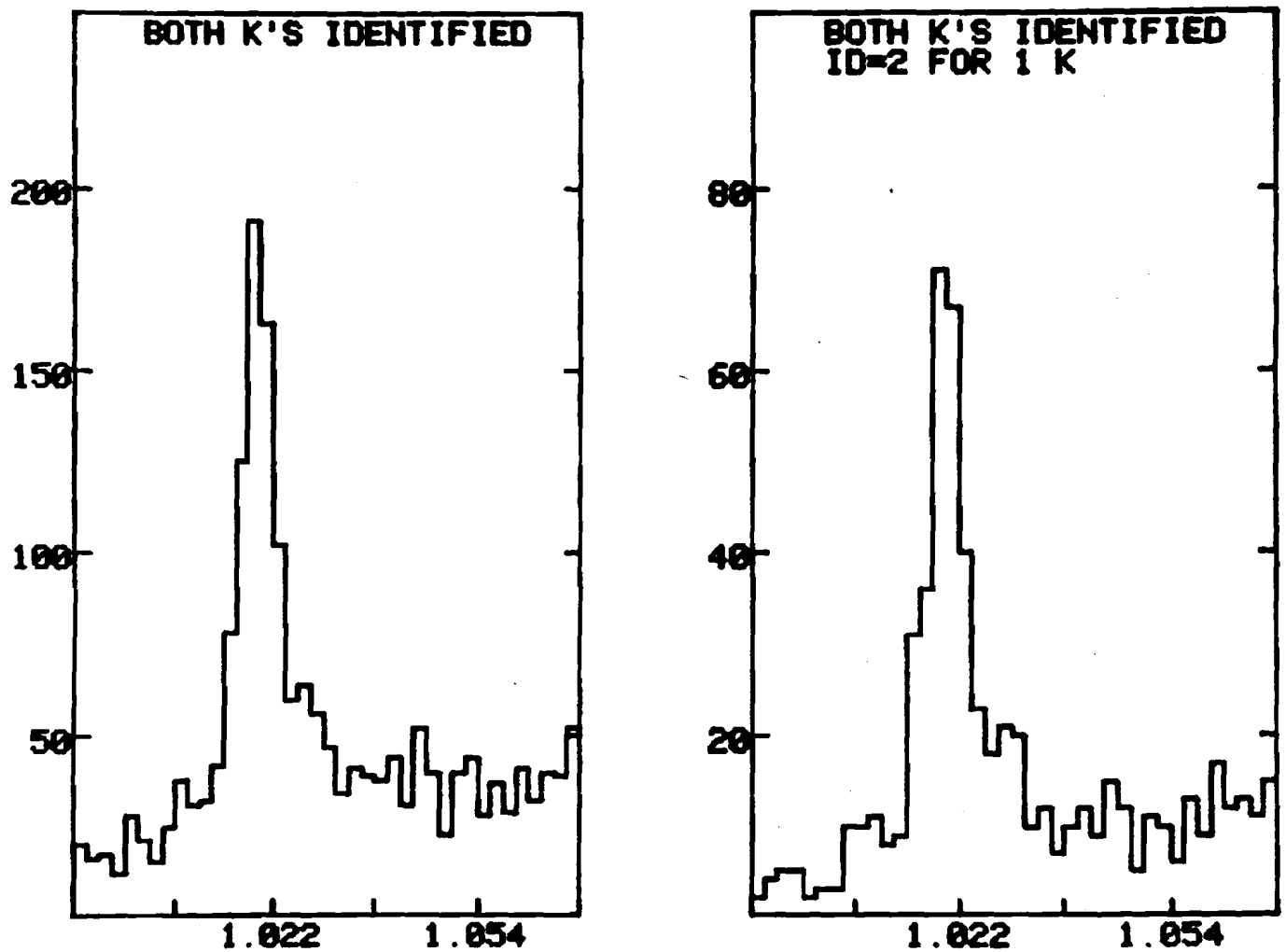

KK MASS DISTRIBUTIONS VS CERENKOV IDENTIFICATION

Figure 4.6

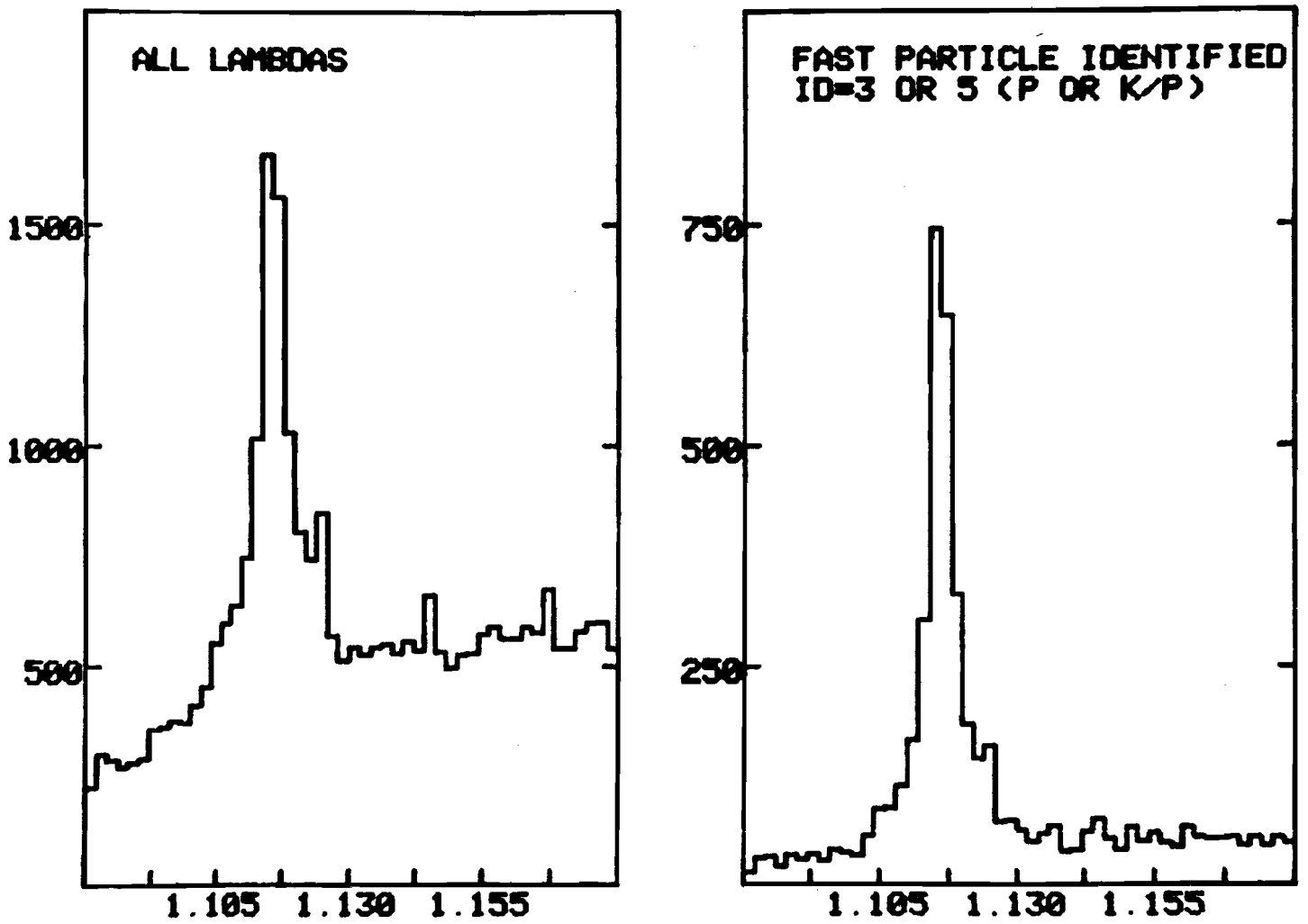

LAMBDA BEFORE AND AFTER HEAVY PARTICLE REQUIREMENT

Figure 4.7

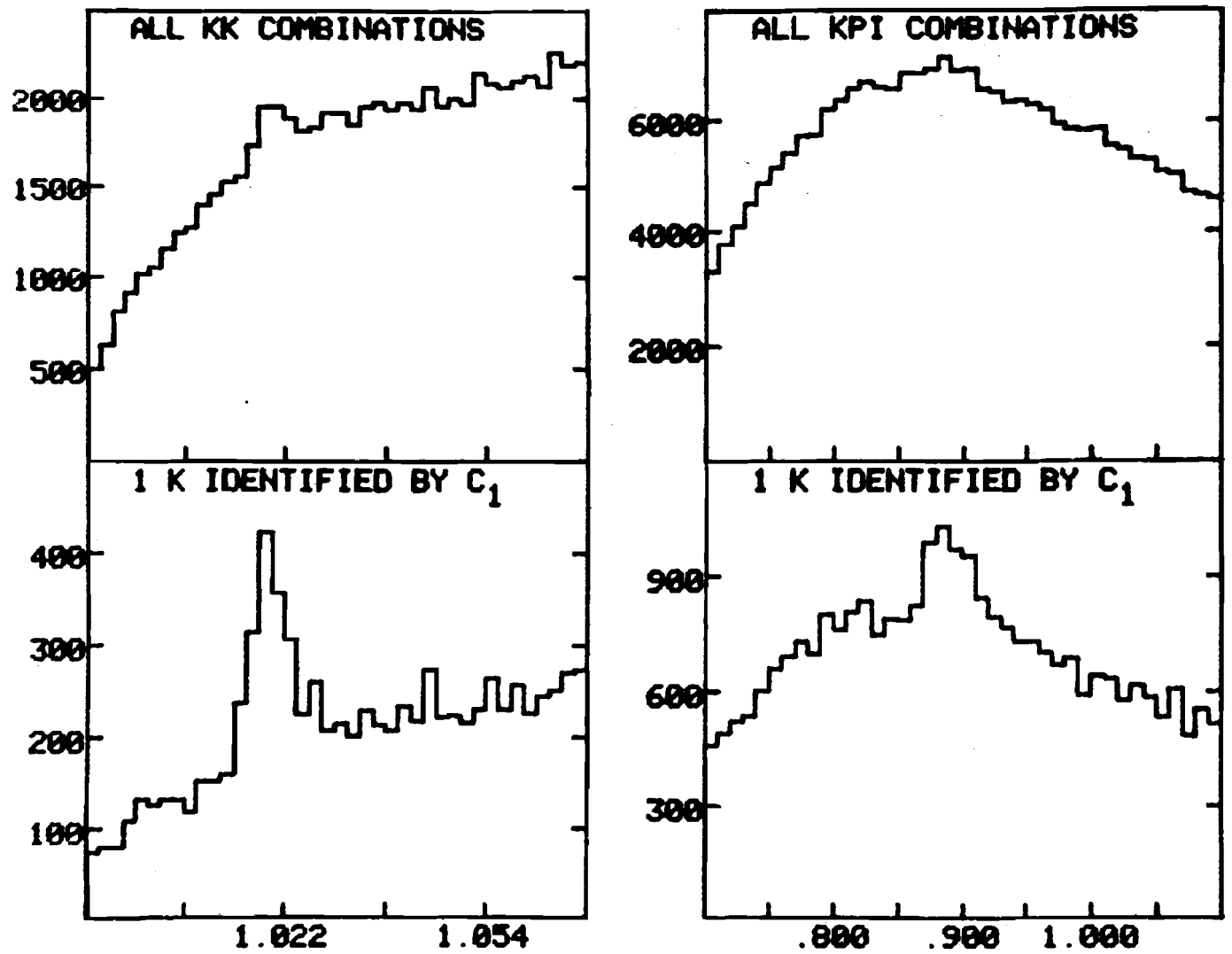

KK AND KPI MASS PLOTS FOR $7 < P_K < 21$ GEV

Figure 4.8

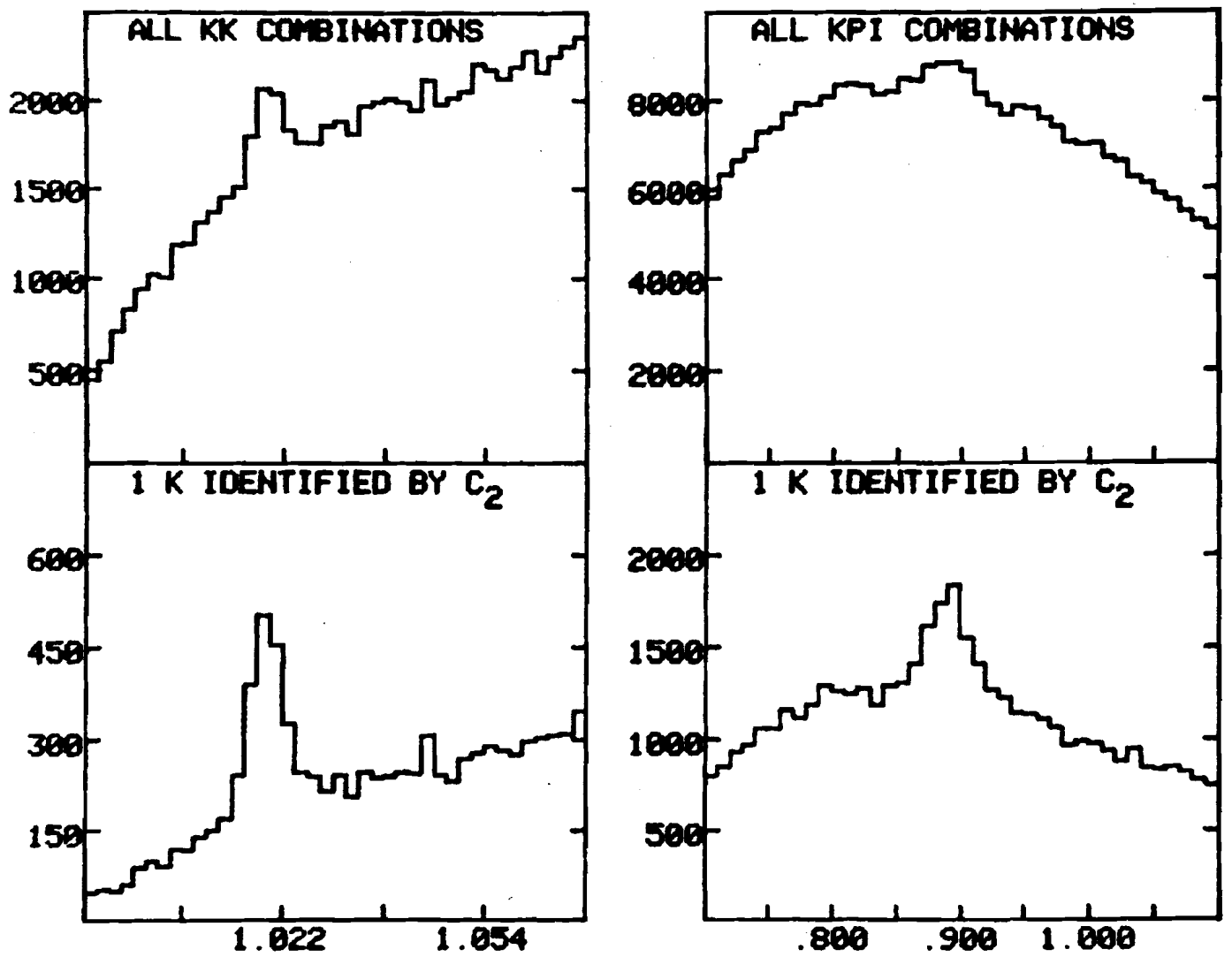

KK AND KPI MASS PLOTS FOR $12 < P_K < 38$ GEV

Figure 4.9

Fitting these histograms to a Gaussian signal plus polynomial background yields the results shown in the table below.

	C1		C2	
	Phi	K*	Phi	K*
Total	1005 ± 98	1889 ± 249	1518 ± 53	2609 ± 270
Ident	787 ± 42	1082 ± 81	1135 ± 45	2579 ± 137
Eff.	.78 ± .04	.58 ± .07	.74 ± .03	.96 ± .10

The apparent discrepancy between the K efficiency determined from ϕ's and that found from K*'s deserves some comment. Because of the relatively small phase space available for the decay $\phi \rightarrow K^+K^-$, the final state kaons are highly correlated both in position and momentum, hence a significant part of the K efficiency determined from ϕ events reflects the detailed nature of this correlation. The K* data provides a more realistic estimate of the true kaon identification efficiency because the K used in the study is not kinematically correlated with any other possible kaon in the event.

The table shows that once a kaon is in the right momentum region for K tagging (between pion and kaon threshold), it has a very high probability for being identified in C2. The C1 efficiency is somewhat lower than that of C2 because of the smaller amount of track dispersion at the C1 mirror plane and the light smearing due to the bending of tracks in the magnetic field of M2.

A small part of the inefficiency can be traced to the existence of occasional finite pulse height for mirrors - particularly in C2 - which have no light pointing at them. We believe that these "unused ons" are the remnants of large pulses generated by the showering of electrons several hundred nanoseconds before the event. The net effect is to reduce the efficiency of K and P tagging, which relies on a mirror being off, by approximately 5%.

Section B Trigger Study

The trigger used in this experiment was composed of three distinct elements: (1) Scintillation counters; (2) Band signals from the MWPC's; and (3) the energy busslines. Because scintillation counters have efficiencies in the neighborhood of 100%, we will not discuss this component any further. A similar statement applies to the band signals, which were generated by wires having electronic efficiencies between 97% and 99%. (Of course, the band signal logic will introduce a much larger trigger inefficiency than the electronic efficiency mentioned here because of the geometric constraints it places on final states. This effect can be accounted for in software by tracing each particle through the MWPC's and turning on the appropriate band regions.) This leaves us with the problem of understanding the energy busslines.

Of the three energy busslines, only 13 (hadron energy) and 15 (lead glass energy) were generated independently as outlined schematically in fig. 4.10. This diagram shows a model of the way in which photomultiplier dynode signals were actually processed, with the splits accomplished by passive divider networks. We simulate the busslines being set in the following manner. First, dynode pulses are generated proportional to the energy deposited in the lead glass and calorimeter and smeared by Gaussian distributions having widths appropriate to each device. Two software discriminators with sharp thresholds then test these two signals to form busslines 13 and 15, while bussline 14 (total energy) is set by another discriminator acting on the sum of the two resoluted pulses. This model for bussline behavior is not only conceptually simple, but has the additional advantage of automatically including the correlations among the 3 busslines.

In order to study the energy busslines we made use of 4 prong pin 7

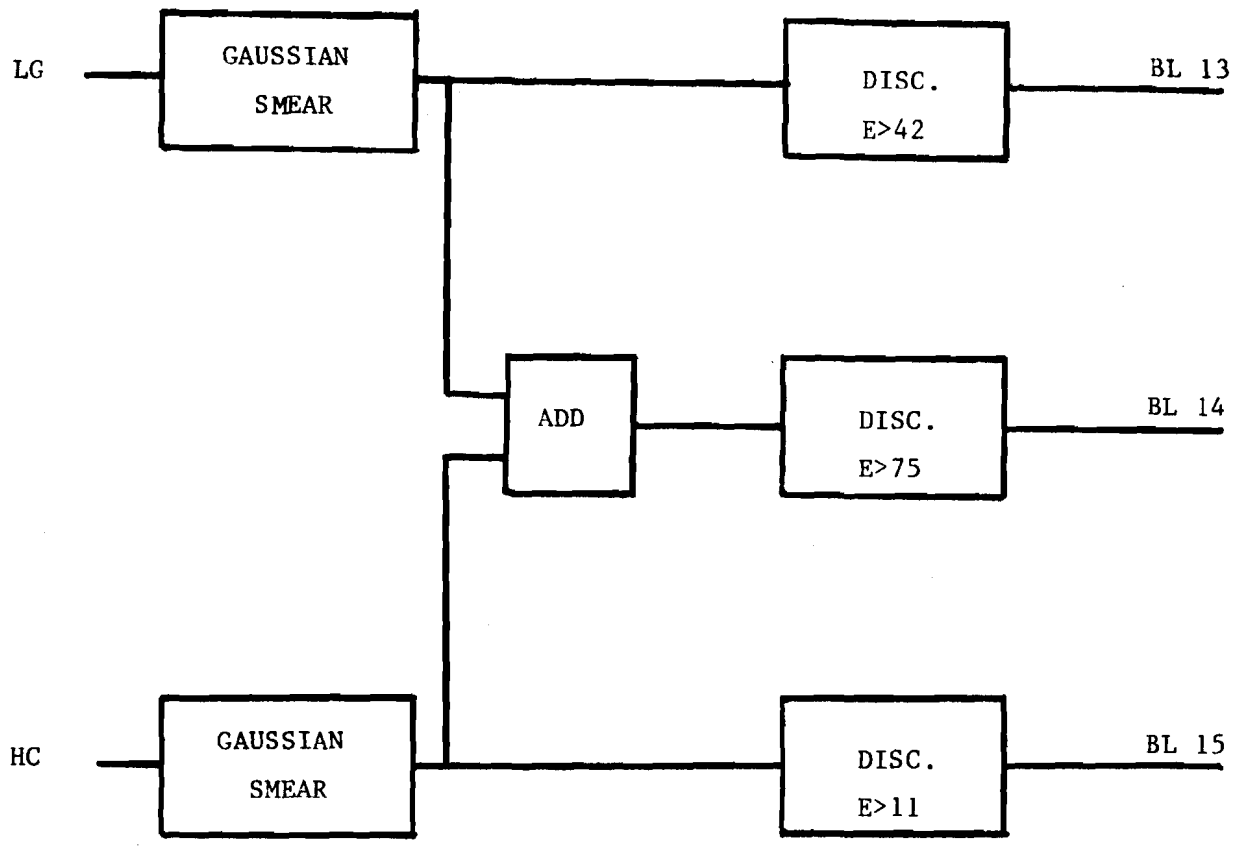

Energy Bussline Model

Figure 4.10

events (those not requiring the energy busslines to be set) to monitor the efficiency of each bussline as a function of the appropriate energy deposition. This energy deposition was obtained for bussline 15 (lead glass) by summing the individual block energies using the measured calibration constants. Unfortunately, this procedure could not be applied to bussline 13 because the hadron calorimeter has very poor resolution. We instead estimated the energy deposited in the calorimeter by the formula:

$$\text{"EHC"} = \text{Espec} - \text{Ehole} - \text{ELG}$$

where Espec = Charged energy in spectrometer
Ehole = Charged energy pointing at hole
ELG = Energy in lead glass

Because of the importance of not having any other neutral energy in the events, we further restricted the data sample to have no non-track associated shower energy. This cut also insured that the quantity ELG in the above formula contained only hadron shower energy in order to make the subtraction meaningful.

Bussline 14 was triggered by the total energy in the lead glass and calorimeter, a quantity which, again, could not be determined directly because of the lack of knowledge regarding the calorimeter calibration constants. We chose the following estimator for this parameter:

$$\text{"ETOT"} = \text{Espec} + \text{Esh} - \text{Ehole}$$

where Esh is the track unassociated lead glass shower energy.

Figure 4.11 shows the efficiencies of busslines 13, 14, and 15 as functions of "EHC", "ETOT", and ELG respectively. These data can be well represented by 4 parameter fits of the form:

$$f(E) = .5(A+B) + \frac{(B-A)}{\pi}\tan^{-1}(E-Eth)/D$$

where A is the asymptotic lower efficiency
B is the asymptotic upper efficiency

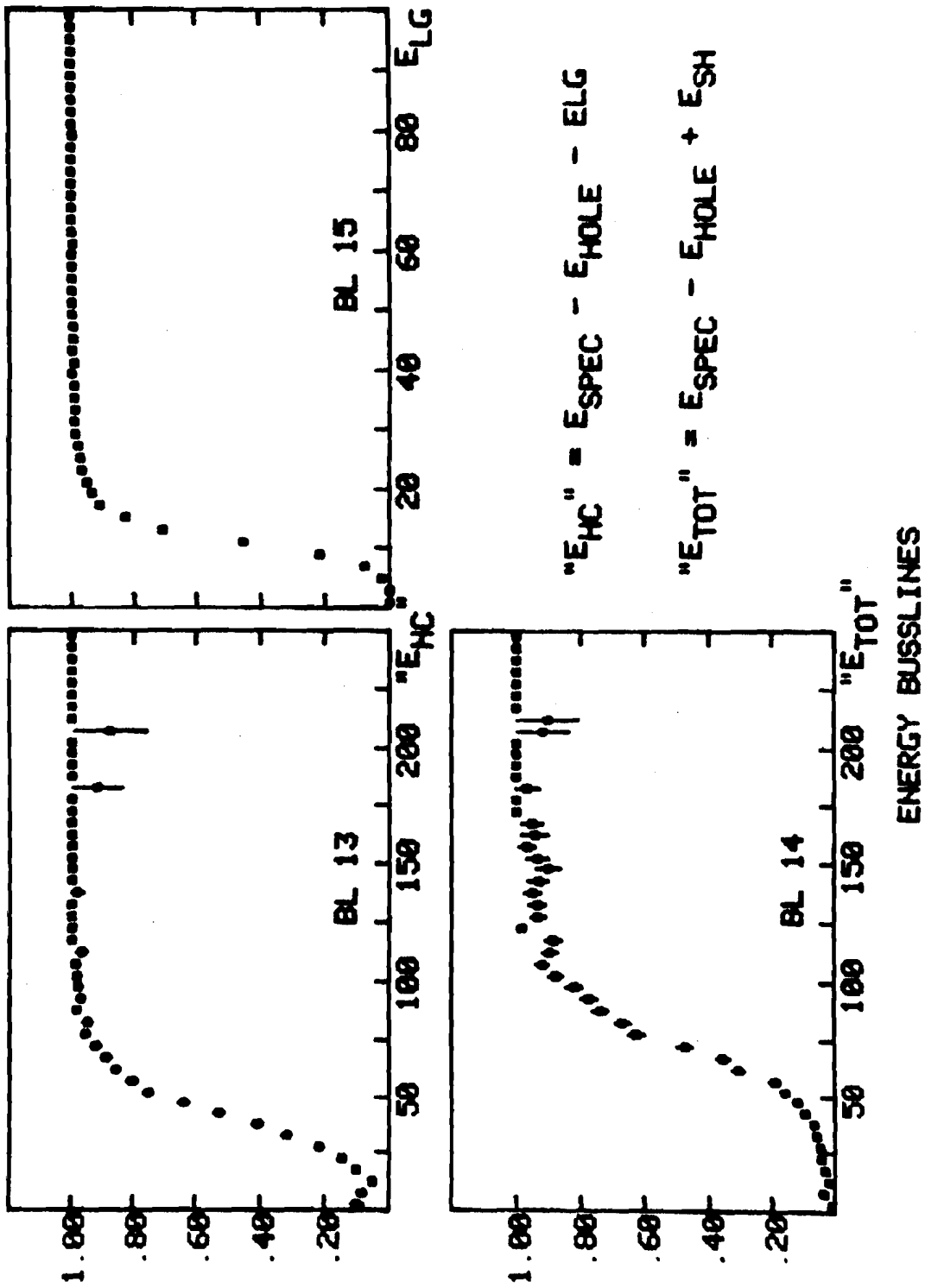
BL 13
BL 14
BL 15
"E_HC" = E_SPEC - E_HOLE - ELG
"E_TOT" = E_SPEC - E_HOLE + E_SH
ENERGY BUSSLINES
"E_HC"
"E_TOT"
E_LG
1.00
.80
.60
.40
.20
50
100
150
200
20
40
60
80

Figure 4.11

Eth is the "threshold" energy
D is the "width" of turnon region

Note that this just the formula one would expect for a Lorentzian distribution of width D being tested by a discriminator of threshold Eth. Although the energy spread is expected to be Gaussian rather than Lorentzian, the fits appear to describe the data reasonably well.

The energy smearing in the lead glass and calorimeter can be studied by histogramming for each device the ratio of the ADC sum to the energy deposition for various regions of energy. Since the ADC sum provides a measurement of the dynode pulse that actually triggered each bussline, the ratio measures the resolution of each device. The resulting energy ratio histograms, some of which are shown in figs. 4.12 and 4.13, exhibit clear Gaussian behavior. If we fit these distributions and plot the resolutions ($\sigma(E)/E$) as a function of energy, we arrive at the data shown in fig. 4.14 (The error bars reflect the fit uncertainties). The points can be reasonably well fit by curves of the form:

$$\sigma(E)/E = C1 + C2/E^{\frac{1}{2}} \qquad \text{(E in GeV)}$$

and C1 = .17 C2 = .051 (Lead Glass)
C1 = .021 C2 = 2.5 (Calorimeter)

Note that these resolutions are not the same as those measured for individual modules. For instance, the resolution of an individual lead glass block is typically $.03+.05/E^{\frac{1}{2}}$.

To check the consistency of these results with the efficiency curves of fig. 4.11 we wrote a Monte Carlo tape containing 4 prong events having mass and t distributions approximately matching those of the data. The tracks were allowed to deposit energy in the lead glass according to the experimentally determined relation:

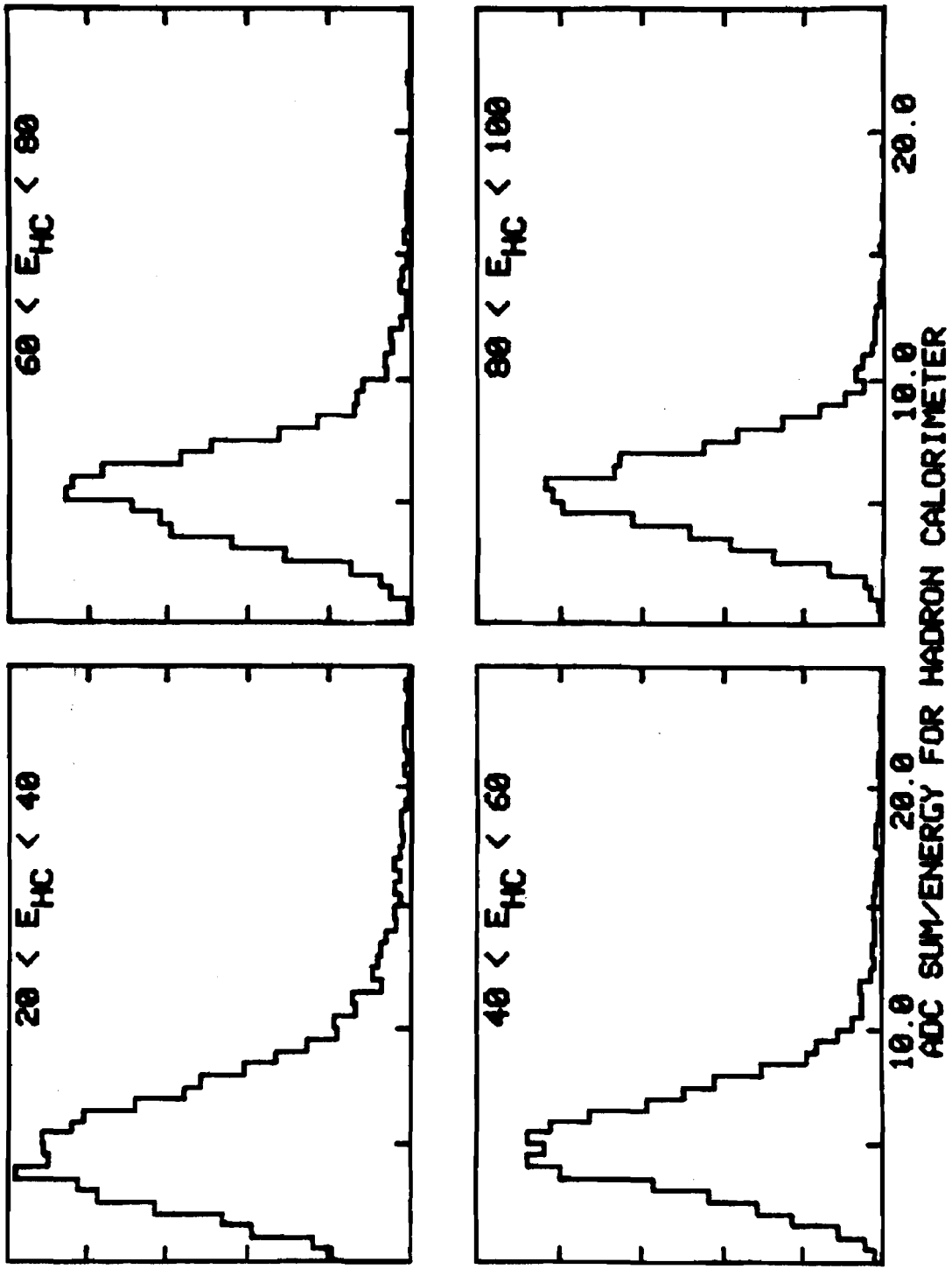
20 < E_HC < 40
60 < E_HC < 80
40 < E_HC < 60
80 < E_HC < 100
10.0
20.0
10.0
20.0
ADC SUM/ENERGY FOR HADRON CALORIMETER

Figure 4.12

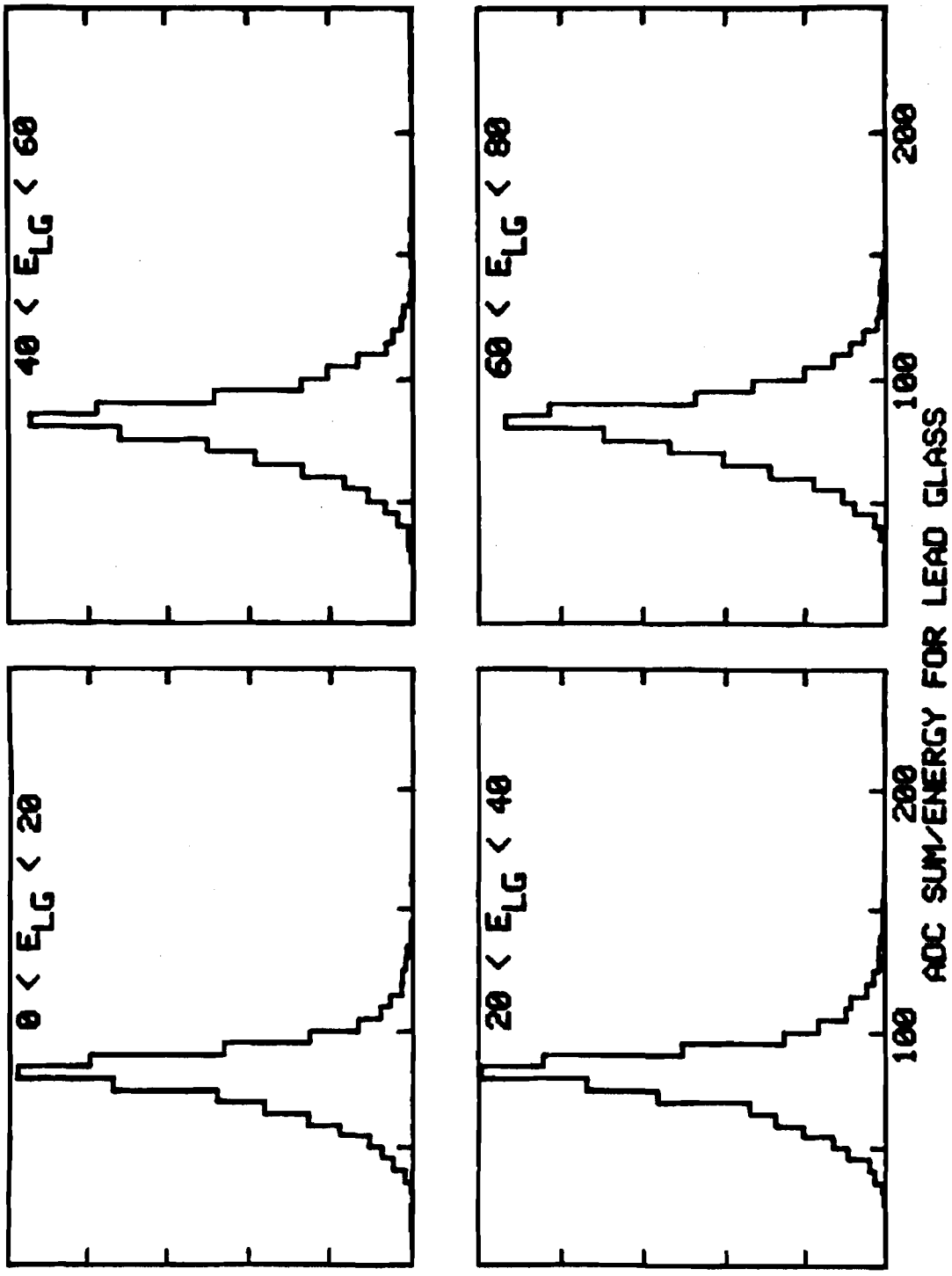
0 < E_LG < 20
20 < E_LG < 40
40 < E_LG < 60
60 < E_LG < 80
100
200
ADC SUM/ENERGY FOR LEAD GLASS

Figure 4.13

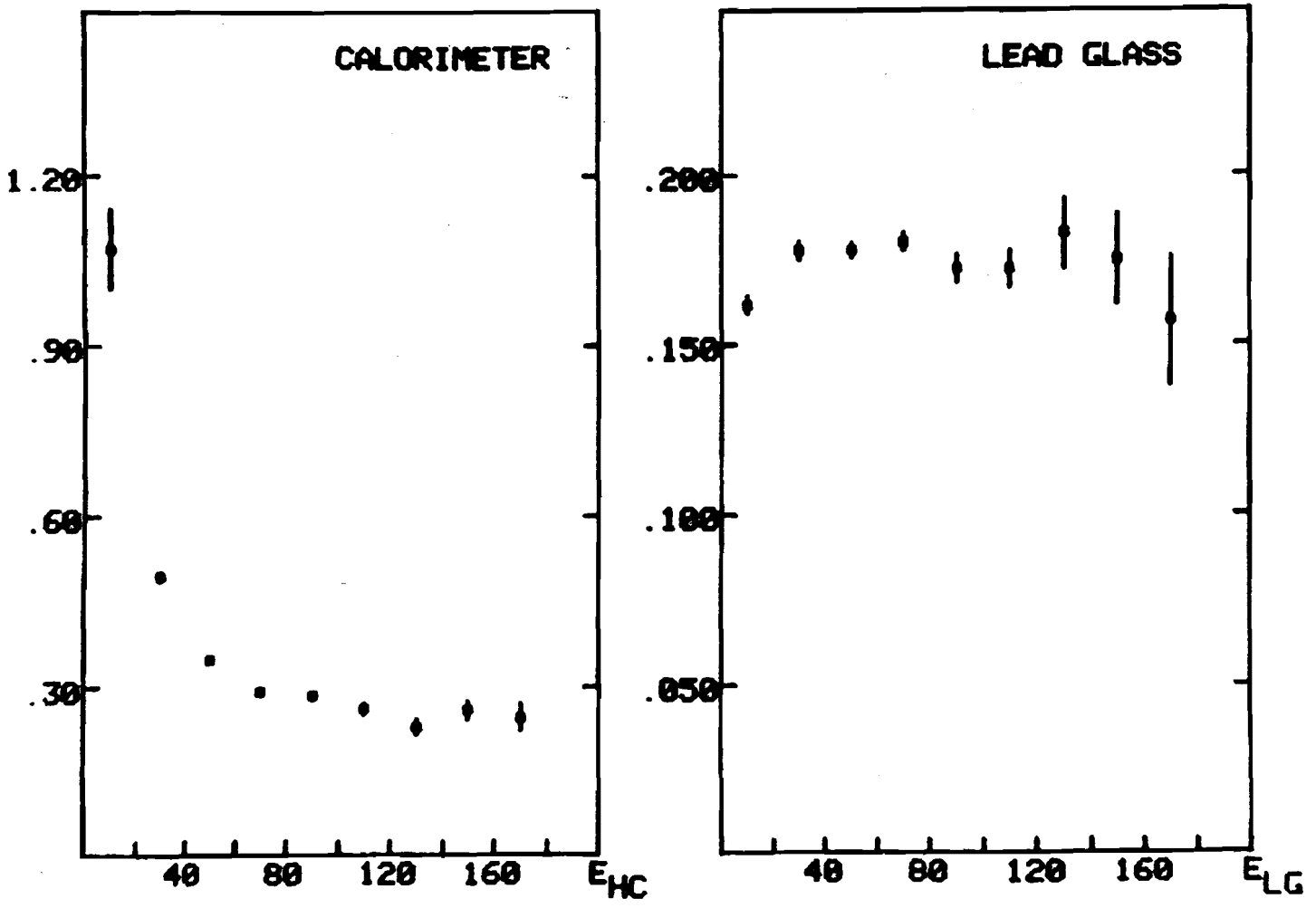

ARRAY RESOLUTIONS FOR CALORIMETER AND LEAD GLASS

Figure 4.14

$$Edep = 0 \qquad 25\% \text{ of the time}$$
$$P = \{1 - \exp(4Edep/E)\} \qquad 75\% \text{ of the time}$$

where Edep is the energy deposited in the lead glass
E is the energy of the track
P is the probability distribution

This formula was derived by studying the hadronic energy deposition in the lead glass for 4 prong events not requiring the energy busslines in the trigger (Pin 7 events).

The simulated energy deposition in both the lead glass and calorimeter was smeared by Gaussian functions with widths given as above, and the resulting "measured" energies were then tested by software discriminators having thresholds given by the values found for the fits to the data shown in fig. 4.11. The resulting Monte Carlo efficiencies for the three busslines are plotted in fig. 4.15 as functions of the appropriate energy depositions. The table below compares the fitted parameters for the data of fig 4.11 with those obtained from the Monte Carlo. Eth and D are the threshold energy and width respectively, as determined from the arctangent fit described earlier in this section. This quantitative comparison confirms the visual agreement of the two sets of distributions and allows us to claim that we are able to reproduce the energy bussline behavior to a satisfactory degree.

	Eth (GeV)		D (GeV)	
	Data	MC	Data	MC
BL 13	40.9 ± .3	41.8 ± 1.0	10.0 ± .1	9.5 ± .6
BL 14	72.6 ± .4	69.8 ± 1.5	14.5 ± .8	15.0 ± 1.2
BL 15	11.1 ± .1	11.1 ± .1	1.35 ± .02	1.10 ± .1

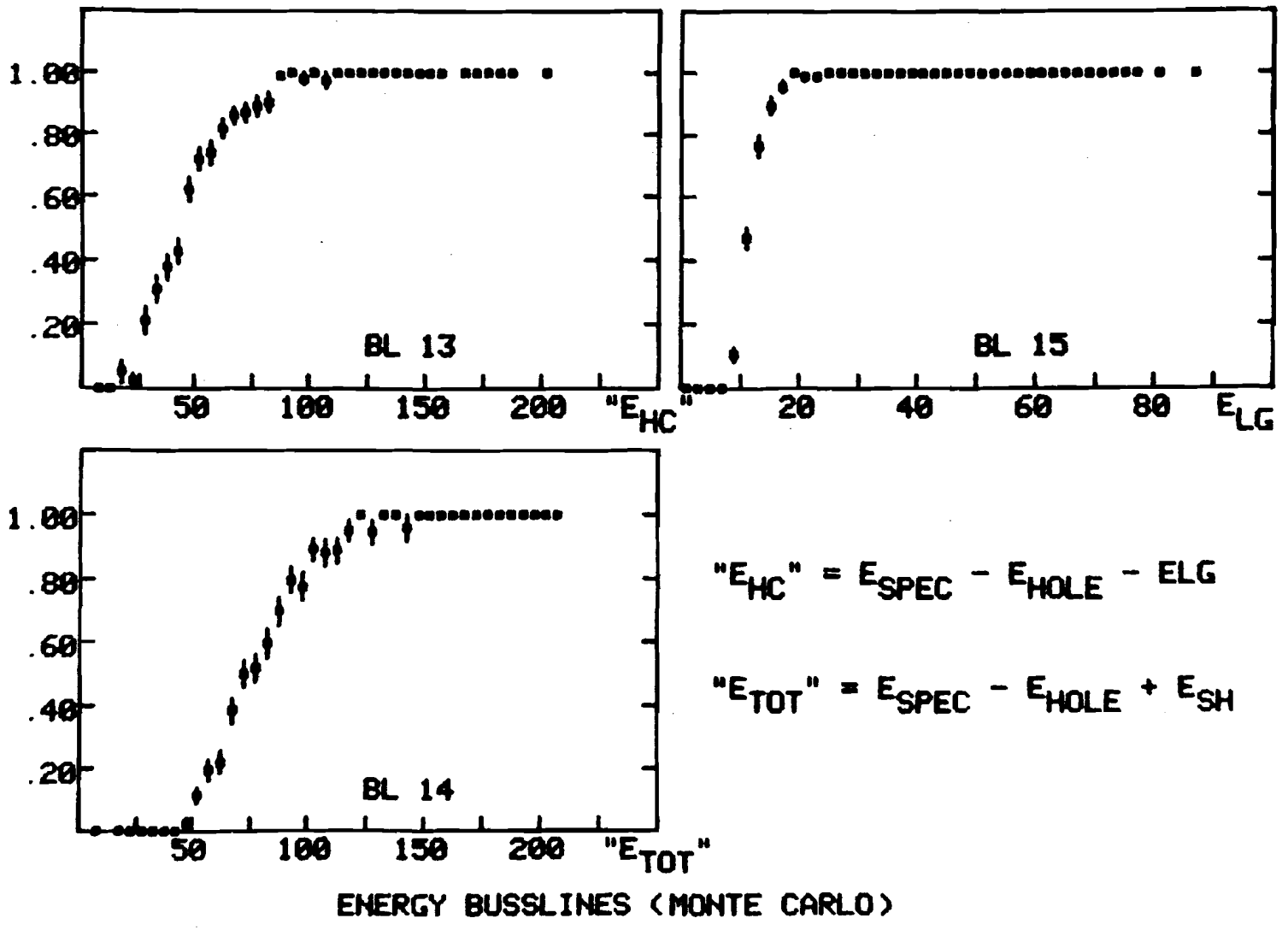
1.00
.80
.60
.40
.20
BL 13
50
100
150
200
"E_HC"
BL 15
20
40
60
80
E_LG
BL 14
"E_TOT"
"E_HC" = E_SPEC - E_HOLE - ELG
"E_TOT" = E_SPEC - E_HOLE + E_SH
ENERGY BUSSLINES (MONTE CARLO)

Figure 4.15

CHAPTER 5

MONTE CARLO

A detector simulation program incorporating many of the detector properties previously discussed was written with the aim of understanding the detection efficiency and resolution for the processes relevant to this thesis. At the core of this package was a routine capable of generating decay final states reflecting the branching ratios of the produced particles. For example, in the process $D^0 \rightarrow K_0\pi^+\pi^-$, the K_0 could decay 50% of the time into K_L and 50% into K_S. If the K_S was selected, it was then allowed to decay into $\pi^+\pi^-$ (69%) or $\pi^0\pi^0$ (31%) along a path whose length was determined from the lifetime and momentum of the K_S. In this manner all unstable particles could decay in a cascade fashion to yield final states consisting of nothing but electrons, muons, charged pions and kaons, protons, neutrinos, and K_L's.

With the 4-vectors of the final state particles at hand, the Monte Carlo generated the interaction vertex uniformly over the target's 2"x2"x1" volume and began tracing the charged and neutral particles through the detector. Special routines swam the charged tracks through the best available representation of the magnetic fields and made hits on the MWPC wires and scintillation counters lying in the path of the particles. The trace was abandoned if the track left the detector volume or struck the steel of one of the magnets.

If a charged track made it as far as the Cerenkov counters, it was allowed to radiate individual photons randomly along the Cerenkov cone. Each of these photons was then traced to a phototube which set a pulse height according to the calibration and smearing constants discussed in chapter 4.

Photons and electrons made electromagnetic showers in the lead glass array via an energy partitioning scheme developed in reference 37. The energy deposited in each block was divided by that block's calibration constant to give an ADC count, which was stored in an array and eventually written onto a magnetic tape.

A software model of the MWPC logic reproduced the operation of hardware logic elements acting on real band signals. In this representation, "struck" wires turned on the appropriate band "signals" which were then processed by FORTRAN routines mimicking the behavior of hardware logic components acting on real signals. At the same time, the TRM drift times were generated with with a smearing parameterized by a Gaussian having $\sigma=1$ count.

The simulation program set the energy busslines according to the prescription of the bussline model described in chapter 4. The lead glass energy deposition was obtained from the sum of the electromagnetic energy (photons and electrons) and the hadronic energy deposited according to the parameterization of chapter 4. The calorimeter energy was determined by adding up the momentum of all tracks pointing at the calorimeter - minus the energy deposited in the lead glass - with care taken to avoid the 6"x6" hole. The lead glass and calorimeter energies were smeared by Gaussian distributions and the resulting signals were then passed through 3 software discriminators to set busslines 13, 14, and 15 in the manner prescribed in chapter 4.

An output routine collected the generated information and wrote it to a magnetic tape in a format identical to a raw data tape. The tapes went through the same processing steps outlined in chapter 3 for real data in order to eliminate any possible bias due to separate handling of data and Monte Carlo events.

CHAPTER 6

THE D* SIGNAL

Section A Observation of Signal

It will be recalled from chapter 1 that the D^{*+}-D^0 mass difference has been measured at SPEAR, using the process $D^{*+} \rightarrow D^0\pi^+$, to be 145.3 ± .5 MeV/$c^2$, just barely above the pion mass. The extremely low Q value for this reaction indicates that a measurement of the mass difference ΔM between the D* and the D^0 would have a much higher resolution than the resolution of the D* or D masses alone because most of the measurement errors cancel during the subtraction. Indeed, a Monte Carlo calculation predicts the ΔM resolution to be on the order of 1 MeV/c^2, compared to the 15 MeV/c^2 expected for a $K\pi$ state at the D^0 mass.

To exploit this fact, we select events containing $K^{\mp}\pi^{\pm}\pi^{\pm}$ combinations, where the K is required to be identified by the Cerenkov system, and plot the quantity $\Delta M = M_{K\pi\pi} - M_{K\pi}$ in fig. 6.1 for: (a) $1.800 < M_{K\pi} < 1.825$ GeV/c^2, (b) $1.850 < M_{K\pi} < 1.875$ GeV/c , and (c) $1.900 < M_{K\pi} < 1.925$ GeV/c^2. A beautiful peak centered at 145.5 MeV/c^2 is seen to stand out when the $K\pi$ mass is constrained to be within 12.5 MeV/c^2 of the D^0. Bear in mind that, except for the $K\pi$ mass requirement, there are absolutely no cuts imposed on this data.

Because the photon beam contains a significant hadron component (accounting for 75% of our trigger rate), we must determine if the D* signal is in fact photoproduced. We resolved this question by examining data taken with 6 radiation lengths of lead inserted into the beam. Applying the same $K\pi$ mass requirements as those imposed on the photon data, and multiplying by 2.35 to correct for the different proton exposures and hadron absorption of the lead, we obtain the shaded portions of the histograms shown in fig. 6.1.

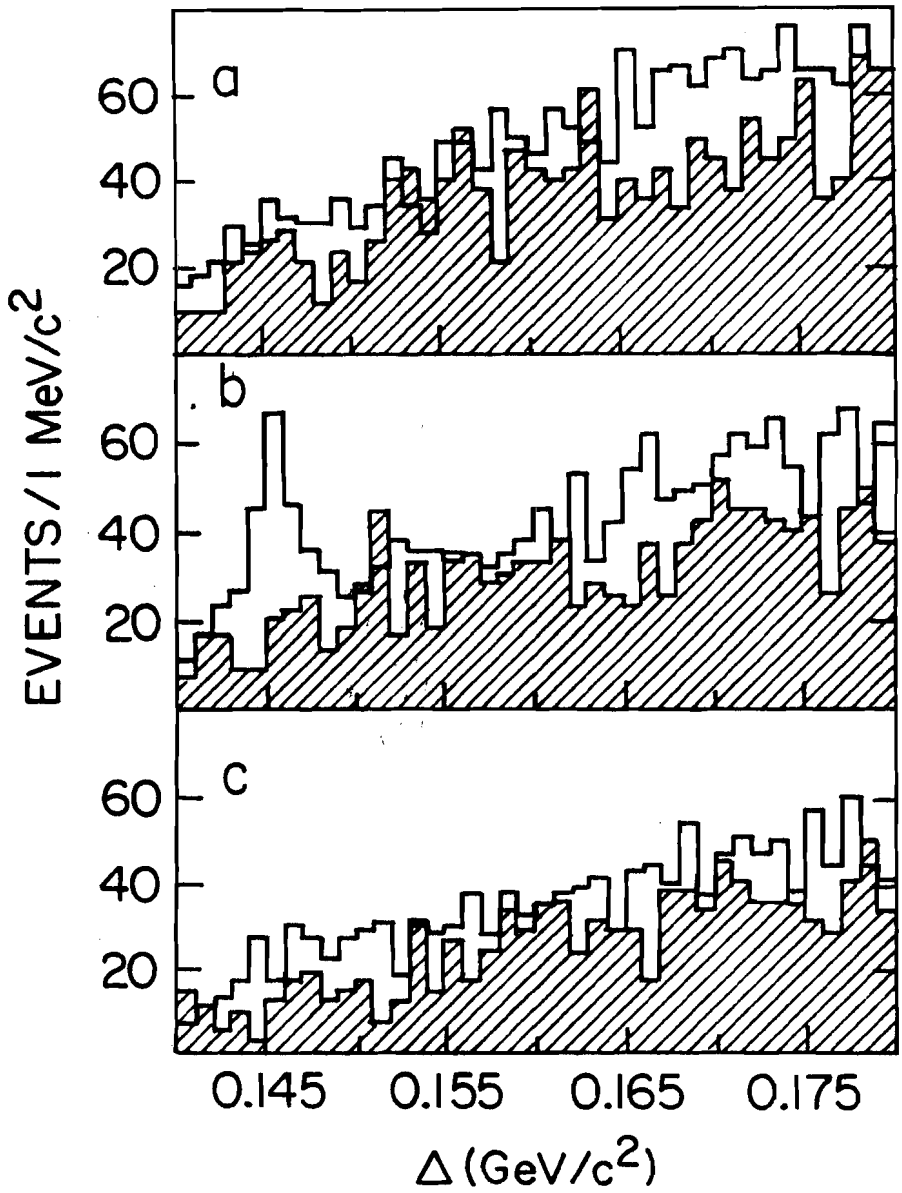

Histogram of $\Delta = M_{K\pi\pi} - M_{K\pi}$ for (a) $1.800 < M_{K\pi} < 1.825$ GeV/c^2 , (b) $1.850 < M_{K\pi} < 1.875$ GeV/c^2 , and (c) $1.900 < M_{K\pi} < 1.925$ GeV/c^2 Shaded histograms are for K_L induced background.

Figure 6.1

Note that not only is there no hint of a hadronically induced D* signal, but that the hadrons - no doubt K_L's - in the photon beam constitute almost all of the background in the region of the D* mass difference peak.

Alternately, we can plot the $K\pi$ mass distribution subject only to the requirement that $.1425 < \Delta M < .148$ GeV/c^2. As seen in fig. 6.2(a), a prominent peak, centered around 1.860 GeV/c^2 towers over the background. A fit to the data of the form exponential background plus Gaussian signal yields the following parameters (all errors are statistical):

$$N = 143 \pm 20 \text{ events}$$
$$M = 1.861 \pm .002 \text{ GeV}/c^2$$
$$\text{FWHM} = .023 \pm .003 \text{ GeV}/c^2$$

Note that the mass obtained here is in excellent agreement with the quoted SPEAR D^0 value of $1.8633 \pm .0009$ GeV/c^2.

It is amusing to note that the signal to noise ratios of both the ΔM and $K\pi$ mass distributions are so good that the D* can be seen by the eye in a scatter plot of ΔM vs $M_{K\pi}$. A clear clustering of events can be seen near $\Delta M = .145$, $M_{K\pi} = 1.86$ in the completely uncut scatter plot of fig. 6.3.

The background rejection afforded by the ΔM requirement naturally leads us to consider other possible D^0 decay modes, particularly $K_S\pi^+\pi^-$. Once again we histogram the mass difference, defined as $\Delta M = M_{K_S3\pi} - M_{K_S\pi\pi}$, for $K_S\pi^+\pi^-$ masses below, on, and above the D^0 mass as shown in fig. 6.4. A multiplicity cut demanding 7 or fewer charged tracks has been imposed to reduce the combinatorics to acceptable levels, and produces a moderate enhancement in the correct bin in the middle plot of fig. 6.4. Alternately, we histogram the $K_S\pi^+\pi^-$ mass subject to the above multiplicity cut and demand a tighter ΔM cut, $.1445 < \Delta M < .1465$ GeV/c^2, to produce the histogram pictured in fig. 6.2(b). A fit similar to that performed for the $K\pi$ data yields the parameters:

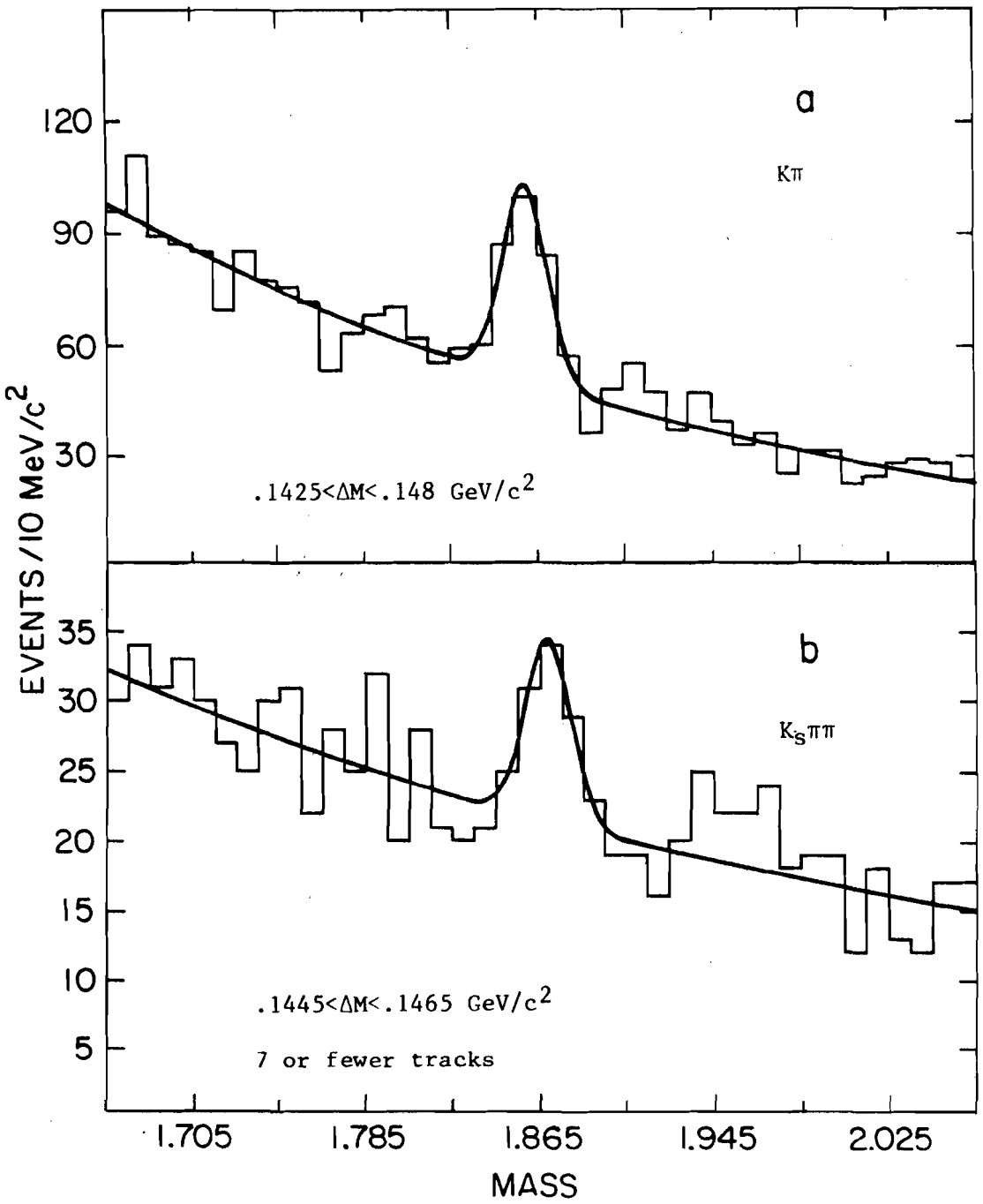

$M_{K\pi}$ and $M_{K_S\pi\pi}$ Invariant Masses with Mass Difference Cut

Figure 6.2

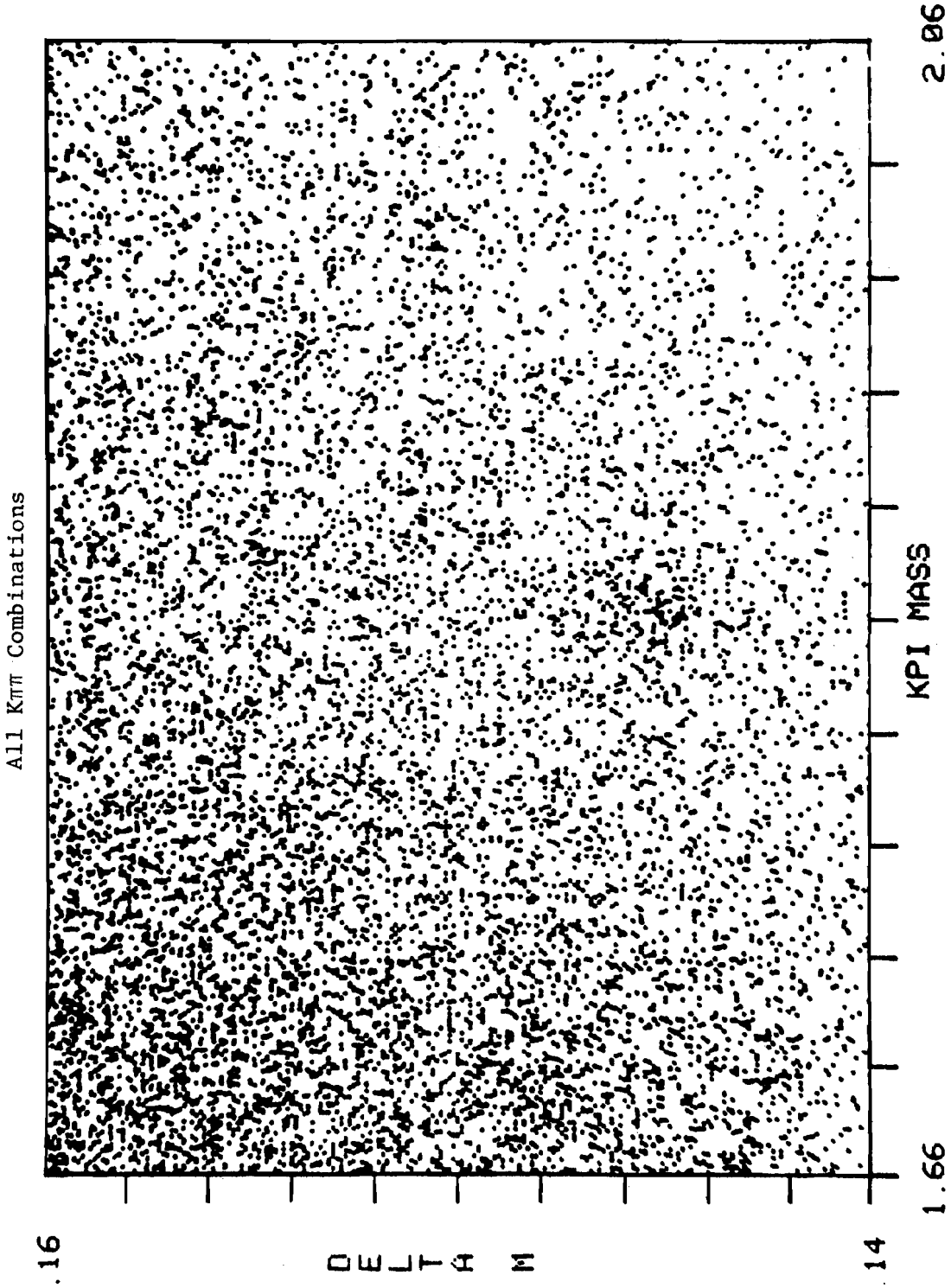

Figure 6.3

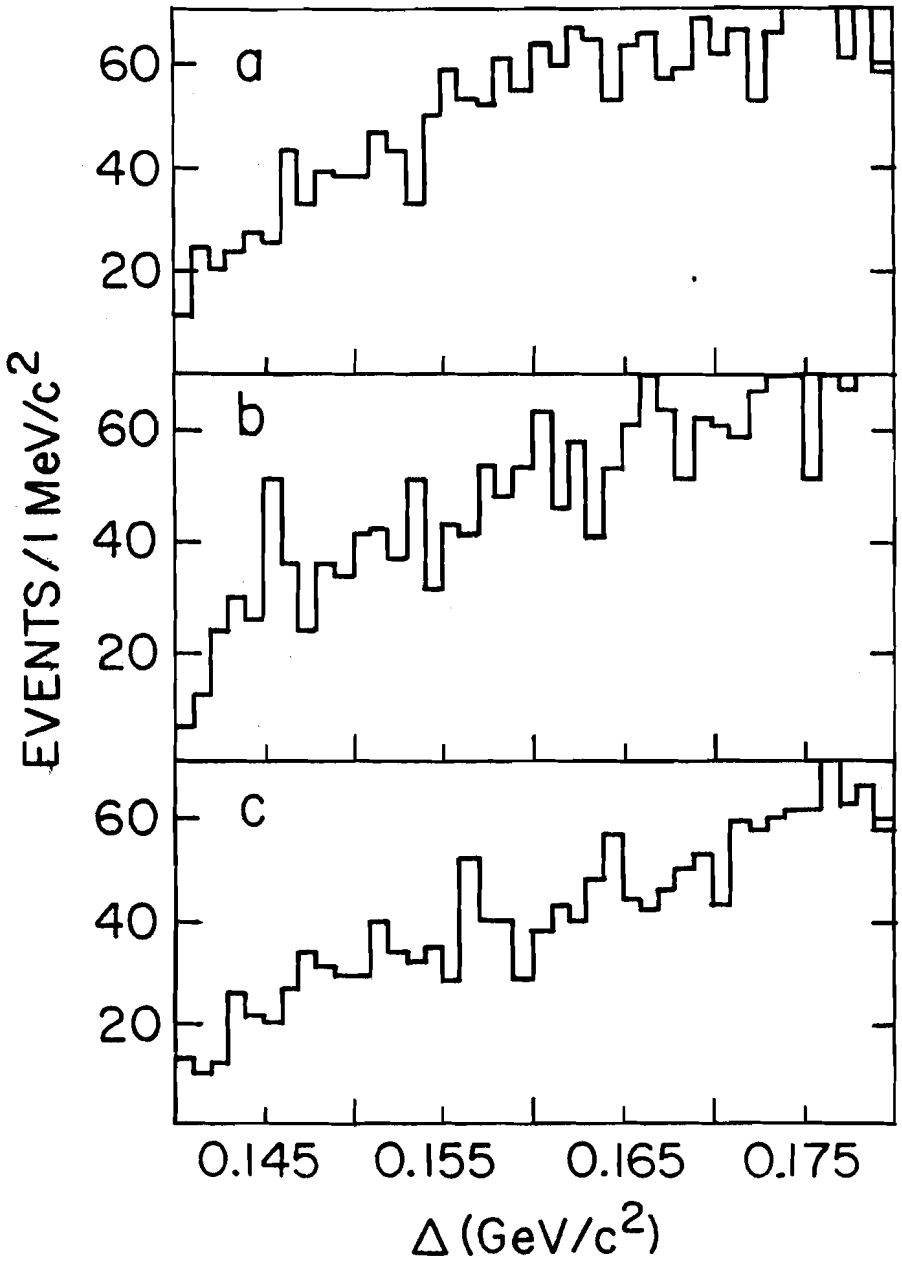

Histogram of $\Delta = M_{K_S 3\pi} - M_{K_S \pi\pi}$ for (a) $1.800 < M_{K_S \pi\pi} < 1.825$ GeV/c^2, (b) $1.850 < M_{K_S \pi\pi} < 1.875$ GeV/c^2, and (c) $1.900 < M_{K_S \pi\pi} < 1.925$ GeV/c^2

Figure 6.4

$$N = 35 \pm 11 \text{ events}$$
$$M = 1.869 \pm .004 \text{ Gev}/c^2$$
$$FWHM = .025 \pm .007 \text{ GeV}/c^2$$

A discussion of this result in terms of relative branching ratios is reserved for section D.

Section B $D^0 - \overline{D^0}$ Mixing

The observation of a strong signal in $D^0 \to K^-\pi^+$ and its absence in $D^0 \to K^+\pi^-$ (For notational simplicity, D^{*+} will refer to D^{*-} and D^{*+} in the following discussion on mixing) can be used to set limits on possible $D^0 - \overline{D^0}$ mixing. Such mixing could proceed via the reaction $D^0 \to \pi^+\pi^- \to \overline{D^0}$, but this process has been estimated to be too small for appreciable mixing to take place {38}. On the other hand charm changing neutral currents could induce $D^0 - \overline{D^0}$ transitions and cause complete mixing if the transition times for such reactions are less than the D^0 lifetime.

We can quantitatively describe the $D^0 - \overline{D^0}$ mixing strength by the fraction of time A that the D^0 decays like a $\overline{D^0}$, or, more precisely

$$A = N1/(N1+N2)$$

where N1 is the number of $D^0 \to (K^+\pi^-)\pi^+$ events
N2 is the number of $D^0 \to (K^-\pi^+)\pi^+$ events

Fig. 6.5 shows the $M_{K\pi}$ distribution for both correct and incorrect strangeness combinations subject to the restrictions $.1445 < \Delta M < .1465$ GeV/c^2 and charged multiplicity less than 7. We can set an upper limit on the parameter A from a simultaneous fit to these distributions using Gaussian signals with a common centroid and FWHM. This procedure yields the confidence level plot shown in fig. 6.6 from which we find that the fraction of time A that a D^0 decays like a $\overline{D^0}$ is less than .11 at the 90% confidence level. This result is similar to the .16 upper bound obtained by MARK I {8}.

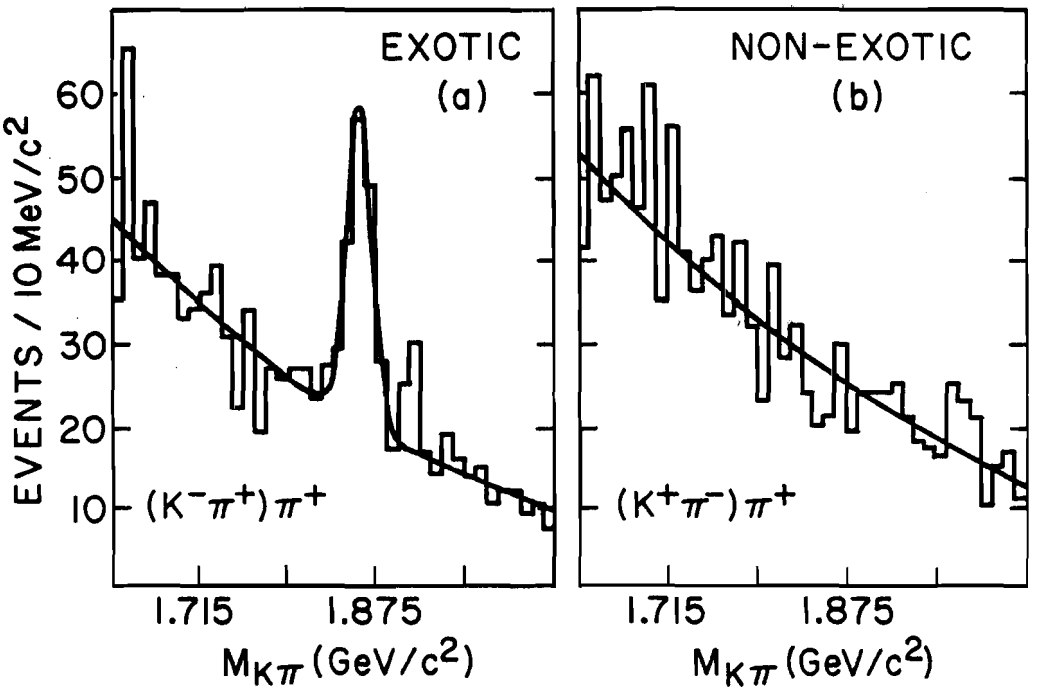

Kπ Invariant Mass for (a) Exotic and (b) Non-Exotic Kππ Combinations for Events having 7 or Fewer Tracks and Satisfying $.1445<\Delta M<.1465$ GeV/c^2

Figure 6.5

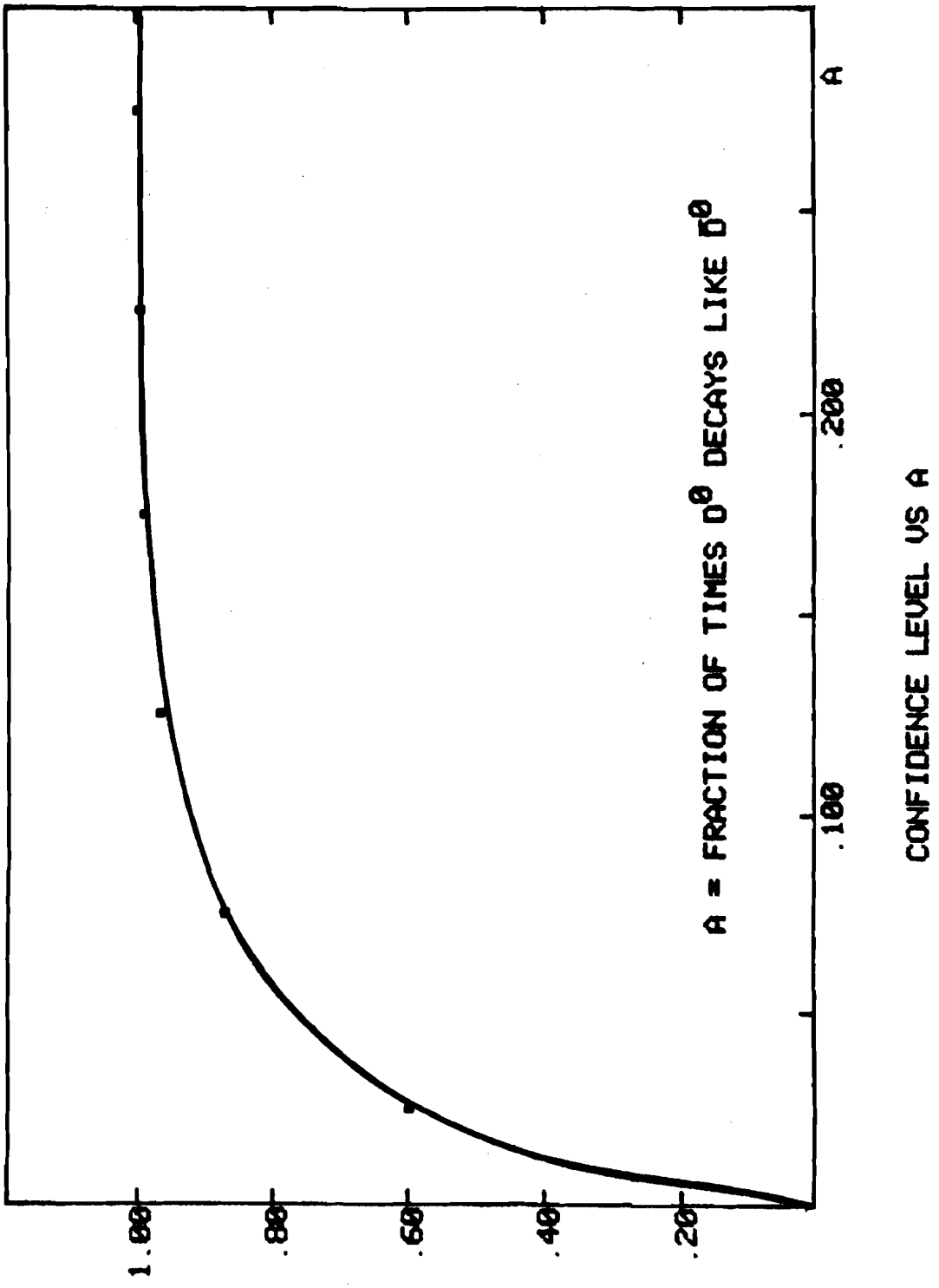
1.00
.80
.60
.40
.20
.100
.200
A
A = FRACTION OF TIMES D^0 DECAYS LIKE $\bar{D}^0$
CONFIDENCE LEVEL VS A

Figure 6.6

Section C How is the D* Produced?

Breaking up the D* signal by charm quantum number, we obtain the ΔM distributions for D^0 and D^0 shown in fig. 6.7. A broad $M_{K\pi}$ requirement of $1.825 < M_{K\pi} < 1.885$ GeV/c^2 was imposed to fully contain the signal. Fits to these distributions yield 61 ± 14 D^{*+} events and 65 ± 15 D^{*-} events, a result completely consistent with equality.

This result suggests that D* mesons are photoproduced against other charmed mesons, as is the case for e+e- annihilation 8 , rather than against charmed baryons as has been predicted elsewhere {39}. We shall show in this section that this indeed appears to be the case and in fact D* photoproduction bears many similarities to D* production by e+e- annihilation near threshold. In particular, we will show that the photoproduced final state for events with a D* consists of a mixture of events of the form $D^{*+}D^{*-}$ or $D^{*+}D^-$ with at most one or two extra pions.

It is of interest to fit the $K\pi$ mass distributions for events containing other heavy particles because such particles provide information about the state produced in association with the D*. These fits are performed using binned likelihood (because of the low statistics) and yield the following results (not corrected for acceptance):

1. 34 ± 9 events with an oppositely charged K against the D*.
2. 4 ± 4 events with a same charged K against the D*
3. 1.7 ± 2 events with a K_S against the D*.
4. 1.9 ± 3 events with a proton against the D*.
5. 3.3 ± 2.3 events with a Λ against the D*.

In fig. 6.8(a) we see the $K\pi$ mass distribution for events with an oppositely charged (opposite to the decay K charge) kaon. The corresponding distributions for events containing a same charge K and same charge P are shown in fig. 6.8(b) and (c). The fraction of total D* events contained in

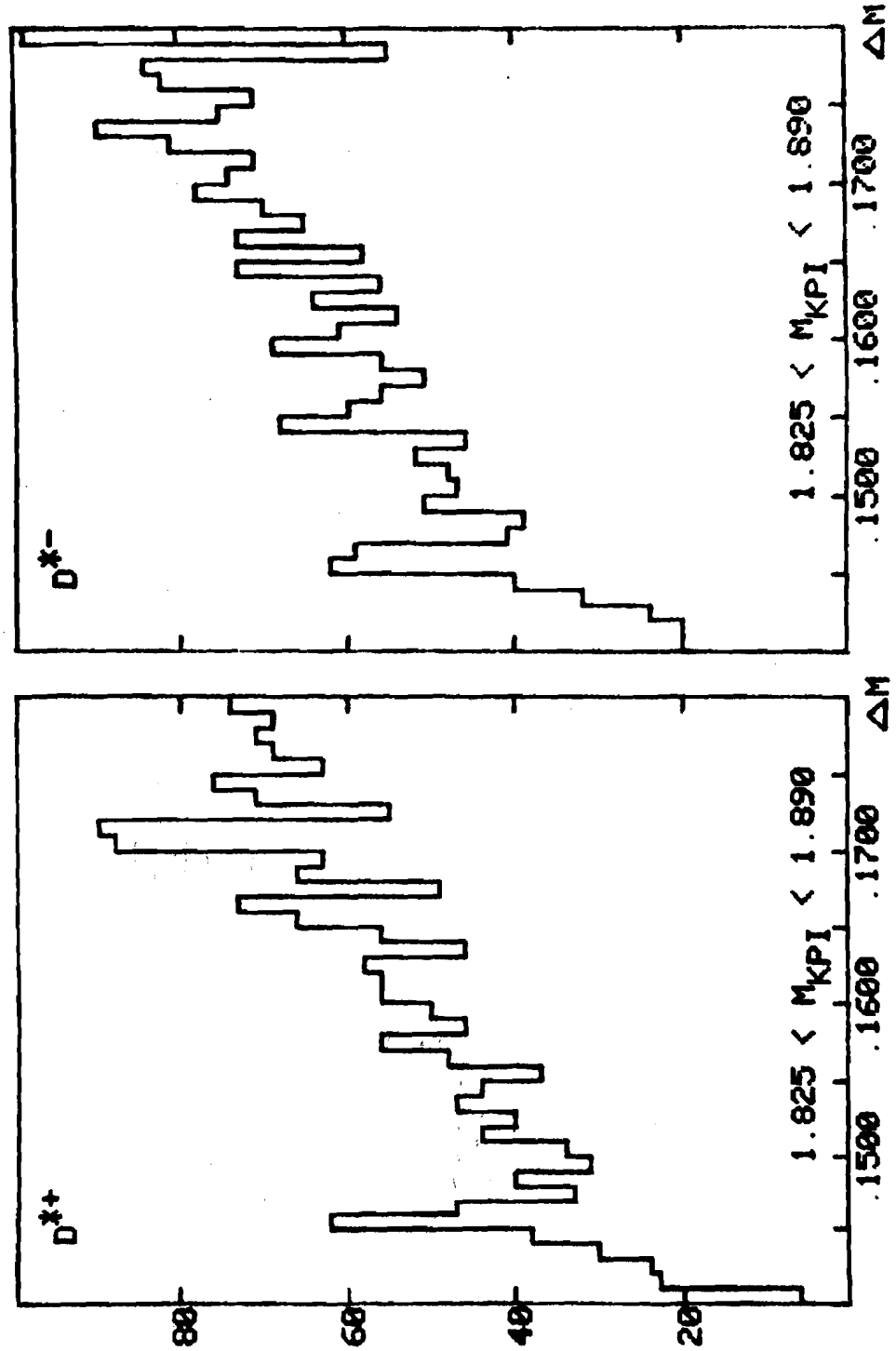

CHARGE BREAKUP OF D* SIGNAL

Figure 6.7

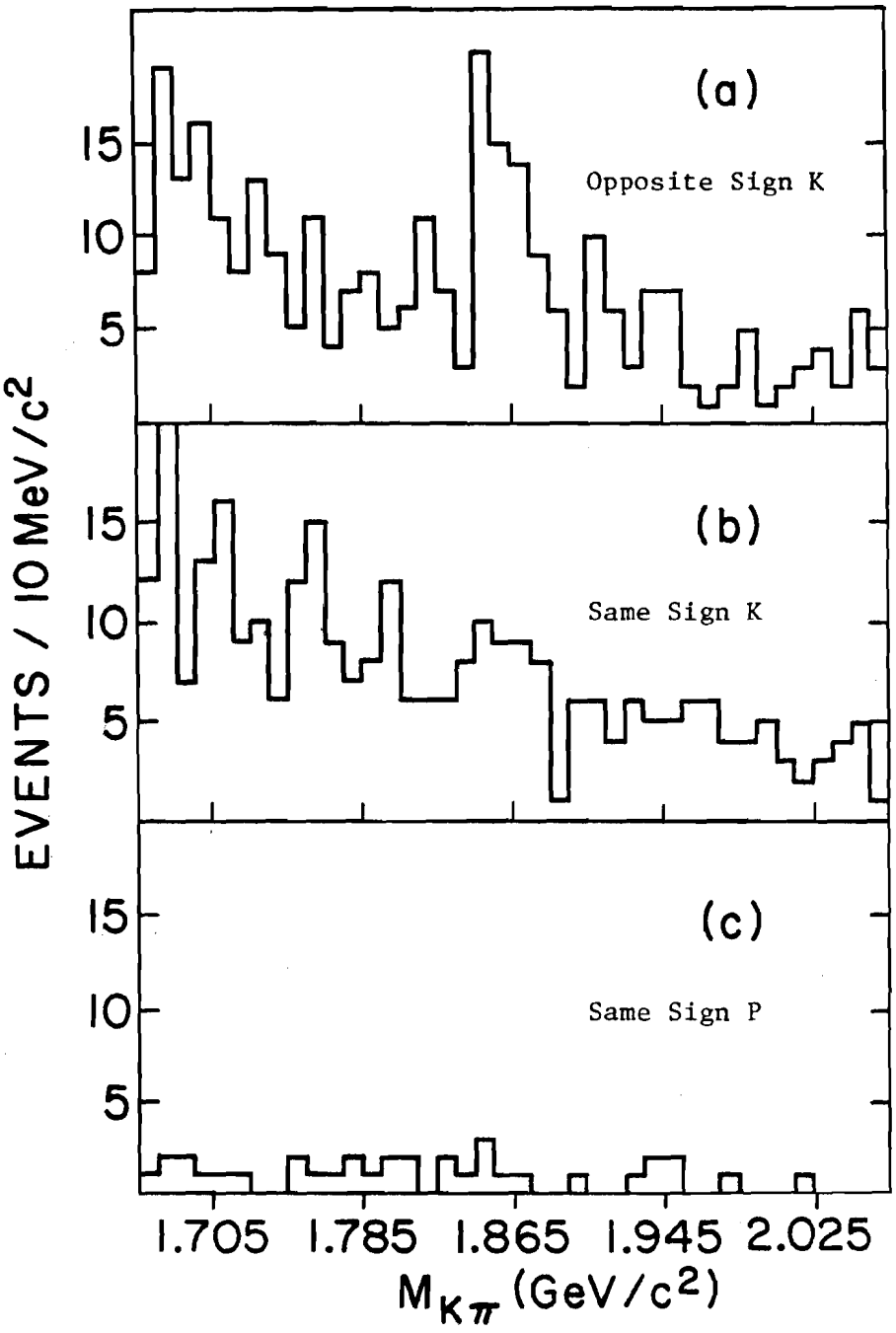

$K\pi$ Invariant Mass Subject to $.1425<\Delta M<.148$ GeV/c^2 for Events Containing (a) an Opposite Charge K, (b) a Same Charge K, and (c) a Same Charge P

Figure 6.8

each of these data samples can be obtained by simultaneously fitting each distribution with the $K\pi$ mass spectrum in fig. 6.2(a), using a Gaussian signal having a common centroid and FWHM. This procedure yields the fractions f_s(opposite)=.23 ± .05 and f_s(same)=.03 ± .027, using obvious notation. For comparison, the fraction of background events with oppositely charged K's is measured to be (using the same $.1425 < \Delta M < .148$ GeV/c^2 cut)

$1.60 < M_{K\pi} < 1.80$ GeV/c^2	f_{B1}(opposite)=.115 ± .007
$1.92 < M_{K\pi} < 2.12$ GeV/c^2	f_{B2}(opposite)=.099 ± .012

Average f_B(opposite)=.11 ± .01

From the value f_s(opposite)=.23 ± .05 we conclude that opposite charge K production in D* events is 2.5 standard deviations larger than background.

Both the signal and background K fractions include some contamination from misidentified pions. This "punch through" was estimated using pions from $K_s \rightarrow \pi\pi$ decay and can be expressed as a probability per track, if the track is already in the right momentum region for K identification ($6 < P < 42$ GeV/c). The number obtained is multiplicity dependent as shown below:

Tracks	Punch through/track
3	.025
4-7	.040
8-9	.050
10	.070

Using these numbers, we compute the probability for obtaining a fake recoil K in our D* events to be about .037 for opposite charge K's and .04 for same charge K's. The recoil K fractions for both signal and background can now be corrected for this effect as shown below.

Before Correction	After Correction
f_s(opposite)=.23 ± .05	.19 ± .05
f_B(opposite)=.11 ± .01	.07 ± .01
f_s(same) =.03 ± .03	-.01 ± .03

The signal fraction above can be corrected for acceptance using a diffractive type model to be described in the next section. The efficiency for picking up the extra K is about .55 ± .05 (a 10% systematic error has been included to reflect uncertainties in the Monte Carlo), which implies

$$f_s^{True}(\text{opposite}) = .35 \pm .09$$

If all D* production is assumed to be accompanied by either a D^0 or D^- (produced either directly or by D* decay) we can use our value of f_s^{True}(opposite) to estimate the fraction due to each. This argument relies on the observation made at SPEAR that charged and neutral D's have quite different branching fractions into charged K's. The average for MARK II and LGW {40} data is

$$B(D^0 \to K^-) = .50 \pm .05$$
$$B(D^+ \to K^-) = .15 \pm .05$$

Combining these results with our recoil fraction of .35 ± .09, we obtain

Recoil D^0	.57 ± .33
Recoil D^-	.43 ± .33

The issue of what recoils against the D* can be studied further by a somewhat different approach. Acceptance limitations and the small (few per cent) exclusive D branching fractions preclude us from looking for recoil D's or D*'s through direct observation. However information on a possible recoil D^{*-} can be obtained by observation of the cascade pion in $D^{*-} \to \pi^- D^0$ decay. This is because the Q value for the reaction is small enough that the pion can be considered to be at rest in the D* center of mass. Transforming to the laboratory frame, we obtain the D^{*-} momentum as being approximately

$$P^{\mu}_{D^{*-}} \simeq \frac{M_{D^*}}{M_{\pi}} P^{\mu}_{\pi^-} \simeq 14.386 P^{\mu}_{\pi^-}$$

If the production mechanism is $D^{*+}D^{*-}$ then the total momentum of the parent state can then be obtained by adding this vector to the observed D^{*+} momentum. We expect the total transverse momentum to peak near 0 because the D* P_t distribution, discussed extensively in chapter 7, is sharply peaked near 0 with 75% of the events having $P_t^2 < 1\ GeV^2/c^2$.

To test these ideas Monte Carlo data (see section D) for diffractive D*D* production were generated and the vector $\Delta^\mu = P^\mu_{D^{*+}} + P^\mu_{D^{*-}}$ was computed using the scaled pion approximation $P^\mu_{D^{*-}} = 14.386 P^\mu_{\pi^-}$. Scatter plots of Δ_x vs Δ_y are shown in fig. 6.9 and 6.10 for "right" and "wrong" sign pions, where "right" means that the charge of the cascade pion is consistent with coming from a recoil D*. The clustering of events in the right sign scatter plot and its absence in the wrong sign plot is evidence that cascade pions can be identified. The radius of the cluster turns out to depend more on the generated P_t of the parent D*D* system than on the pion resolution or the scaled momentum approximation. The particular plots shown in fig. 6.9 and 6.10 had a D*D* t dependence of

$$dN/dt = 11\exp(70t) + \exp(2t)$$

If we accept the fact that the D*D* system is produced near threshold, as required by the sharp D* P_t distribution mentioned previously, then a loose correlation of the D^{*+} and D^{*-} z momenta is expected. We paramaterize this correlation as α_z, where

$$\alpha_z = \frac{P^z_{D^{*+}} - P^z_{D^{*-}}}{P^z_{D^{*+}} + P^z_{D^{*-}}}$$

Fig. 6.11 contains a plot of α_z under the cut $\Delta^2 = \Delta_x^2 + \Delta_y^2 < 4\ GeV/c^2$ and graphically illustrates the difference between right and wrong sign pions as predicted by the Monte Carlo. The figures show that the right sign events

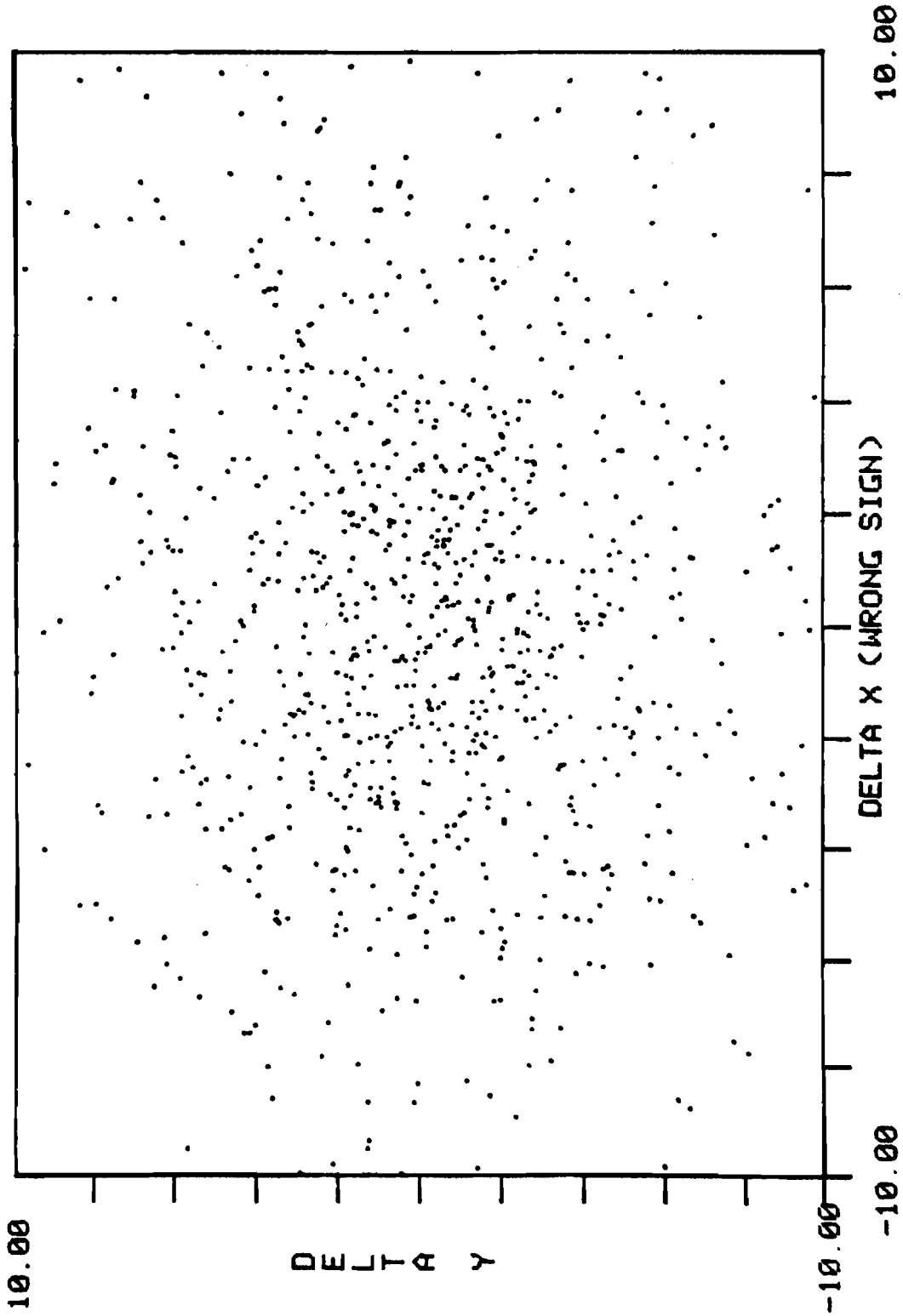

MONTE CARLO

Figure 6.9

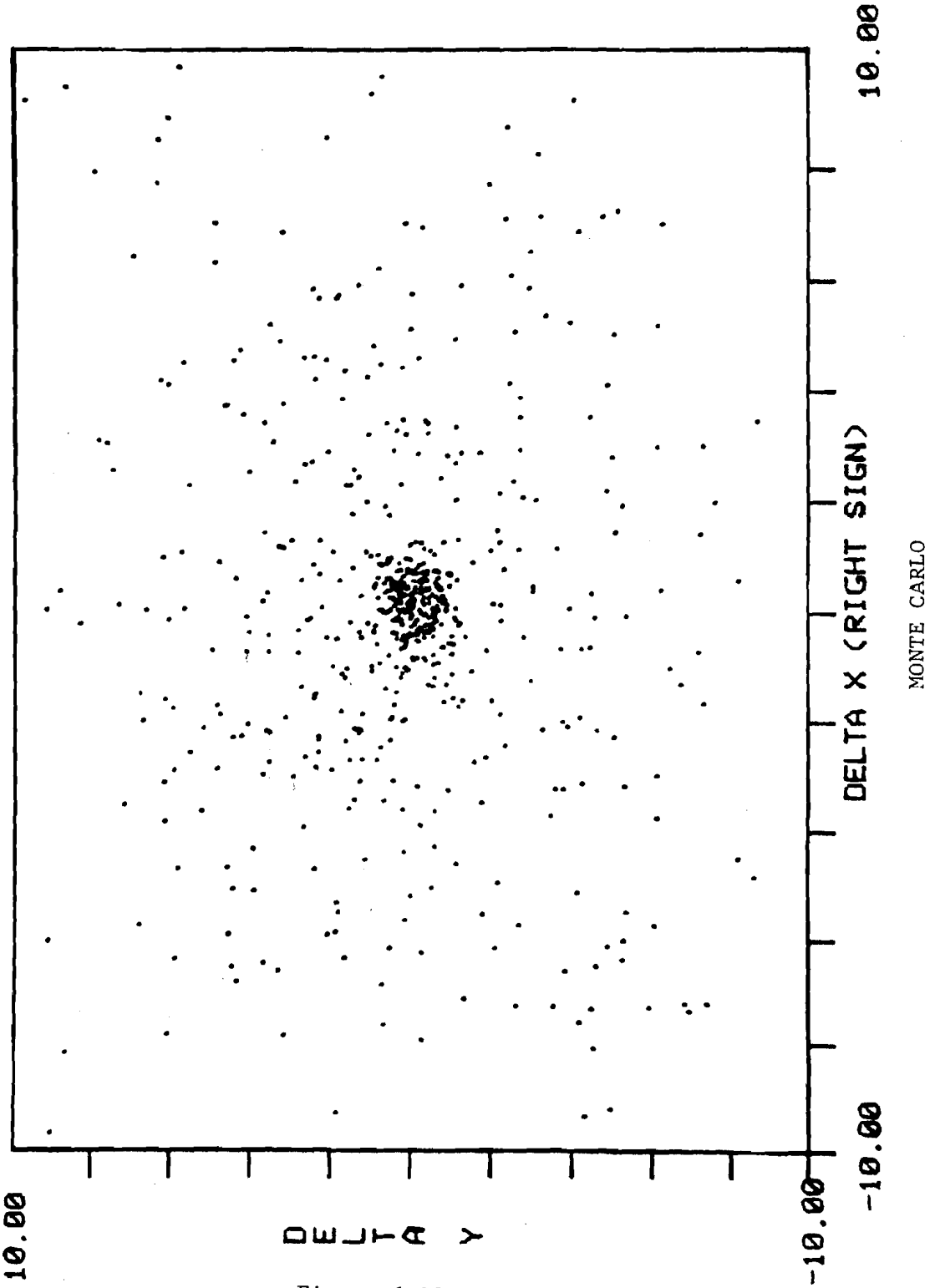

Figure 6.10

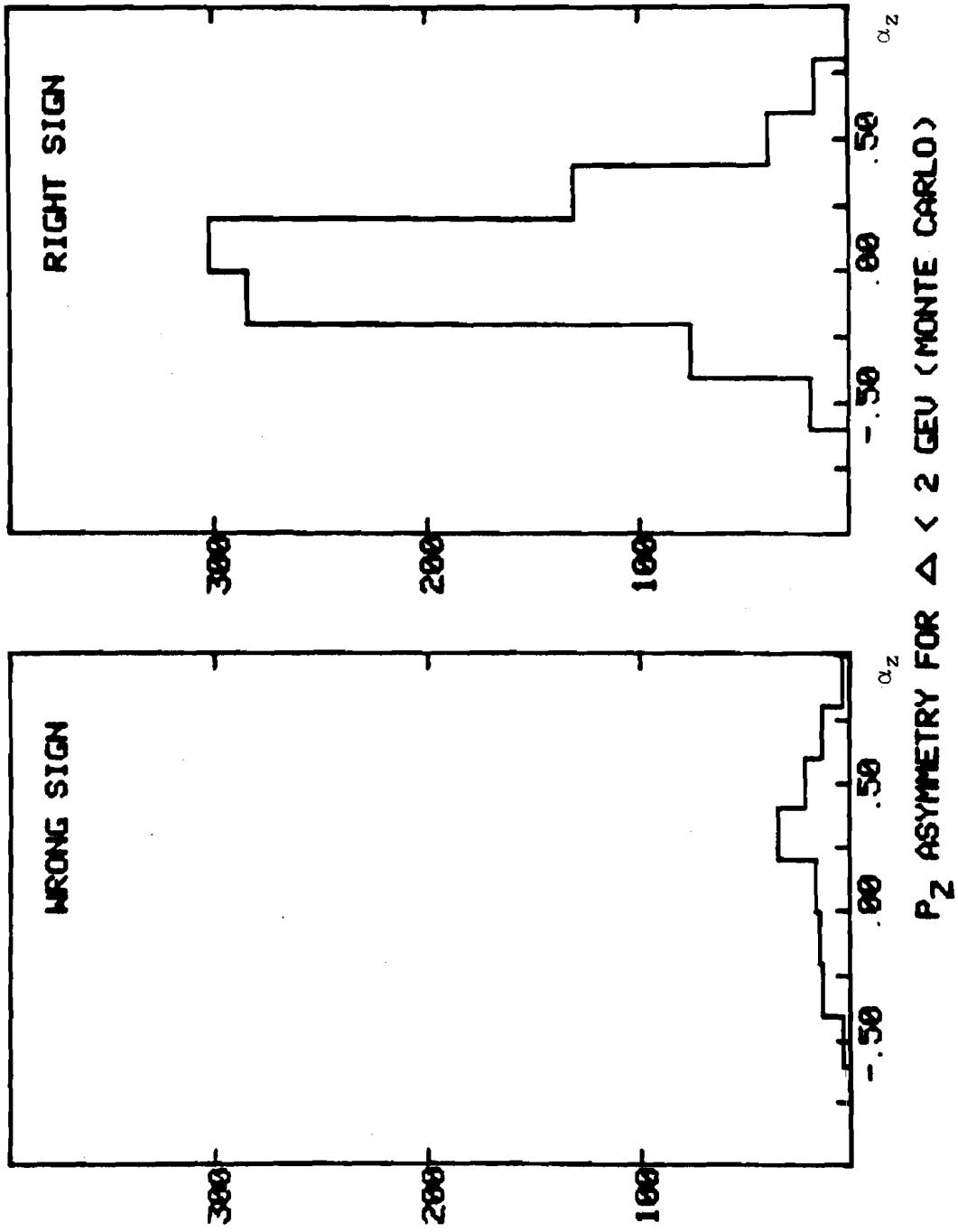
RIGHT SIGN
WRONG SIGN
300
200
100
-.50
.00
.50
α_z
P_Z ASYMMETRY FOR Δ < 2 GEV (MONTE CARLO)

Figure 6.11

peak around α_z=0 while the wrong sign ones have an asymmetric and relatively broad distribution.

Turning now to the data, we plot Δ for right and wrong sign pions as shown in fig. 6.12 for $.143 < \Delta M < .148$ GeV/c^2. The "signal" and "background" regions are defined as

Signal	$1.840 < M_{K\pi} < 1.880$ GeV/c^2		
Background	$1.800 < M_{K\pi} < 1.820$	and	$1.900 < M_{K\pi} < 1.920$ GeV/c^2

Fig. 6.13 shows the subtracted data, where the right sign histogram exhibits a clear excess in the first bin compared to the wrong sign histogram. Corroborating evidence comes when we plot the α_z correlation parameter for events satisfying $\Delta < 2$ as shown in fig. 6.14. The enhancement near α_z=0 for the right sign plot is reminiscent of the Monte Carlo prediction of fig. 6.11. We can carry this procedure further by subtracting the two background histograms from the signal histograms (to separate signal from background), and then subtracting the wrong sign subtracted plot from the right sign subtracted plot (to separate real cascade pions from background pions) using the normalization described below. This twice subtracted distribution, shown in fig. 6.15, has a significant peak near α_z=0.

To estimate the number of cascade pions we must subtract the wrong sign histogram from the right sign plot of fig. 6.13 with the proper normalizing factor. We have picked the bin widths shown in order to fully contain the signal in the first bin for reasonable t distributions. For $\Delta < 2$ there are 42 ± 12 right sign candidates compared to 6 ± 9.4 wrong sign ones. To estimate the number of background events in the $\Delta<2$ region of the right sign plot in fig. 6.13, we assume that the Δ distribution for right and wrong sign pions has the same shape. The 85 right sign and 71 wrong sign events satisfying $\Delta>2$ provide the relative normalization of the two data samples,

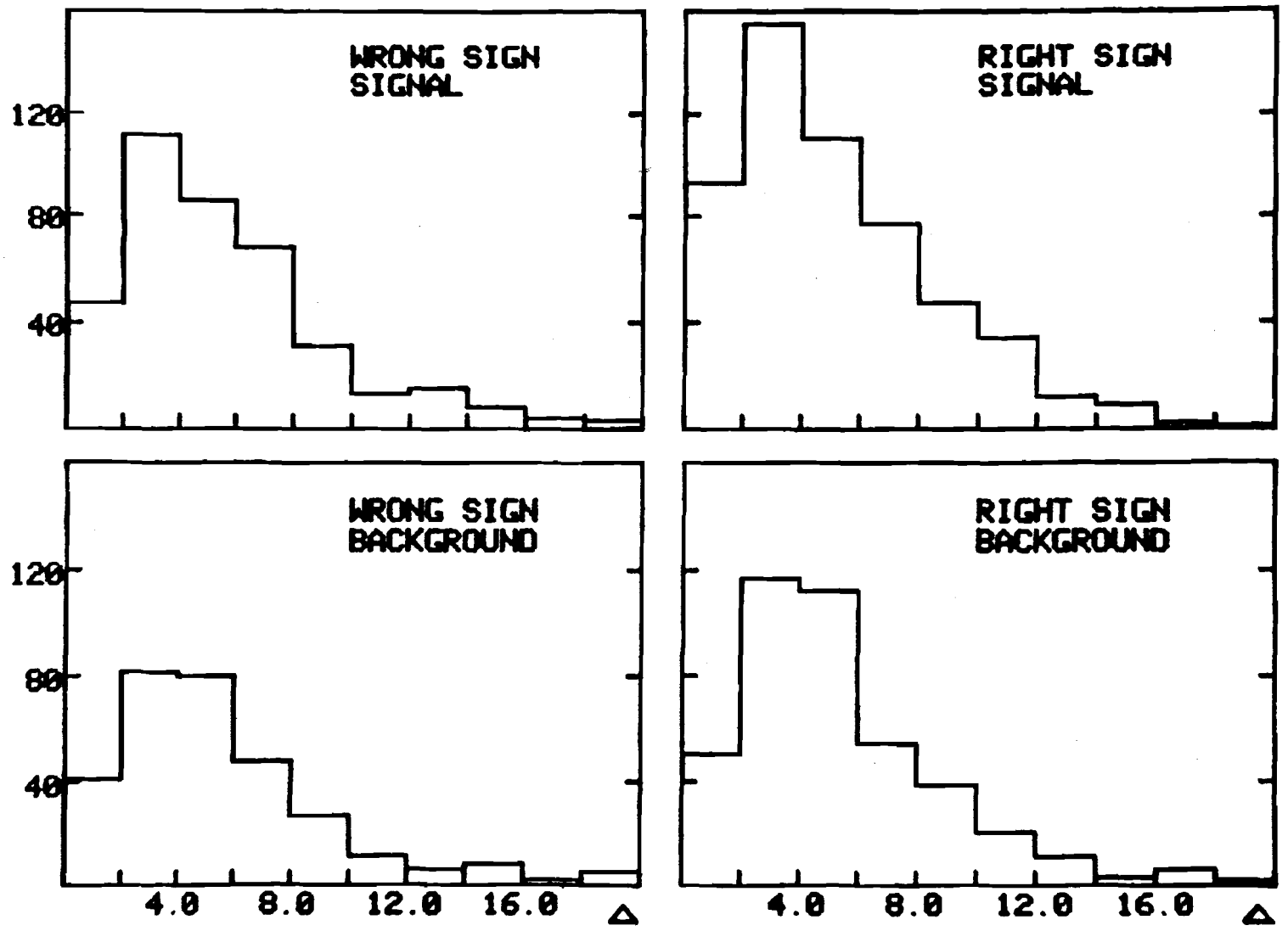

PLOTS OF Δ FOR SIGNAL AND BACKGROUND REGIONS

Figure 6.12

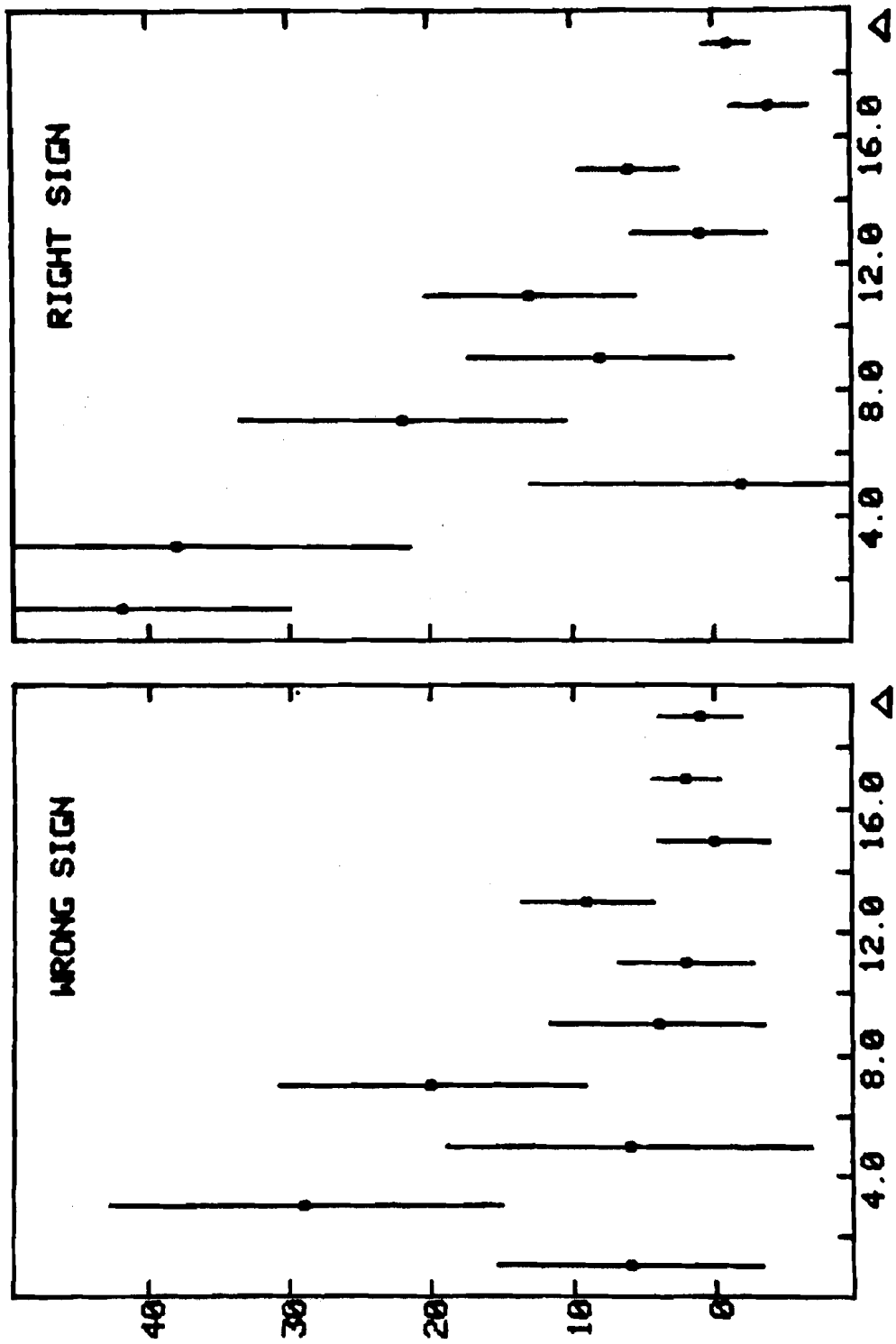

BACKGROUND SUBTRACTED PLOTS OF Δ FOR SIGNAL

Figure 6.13

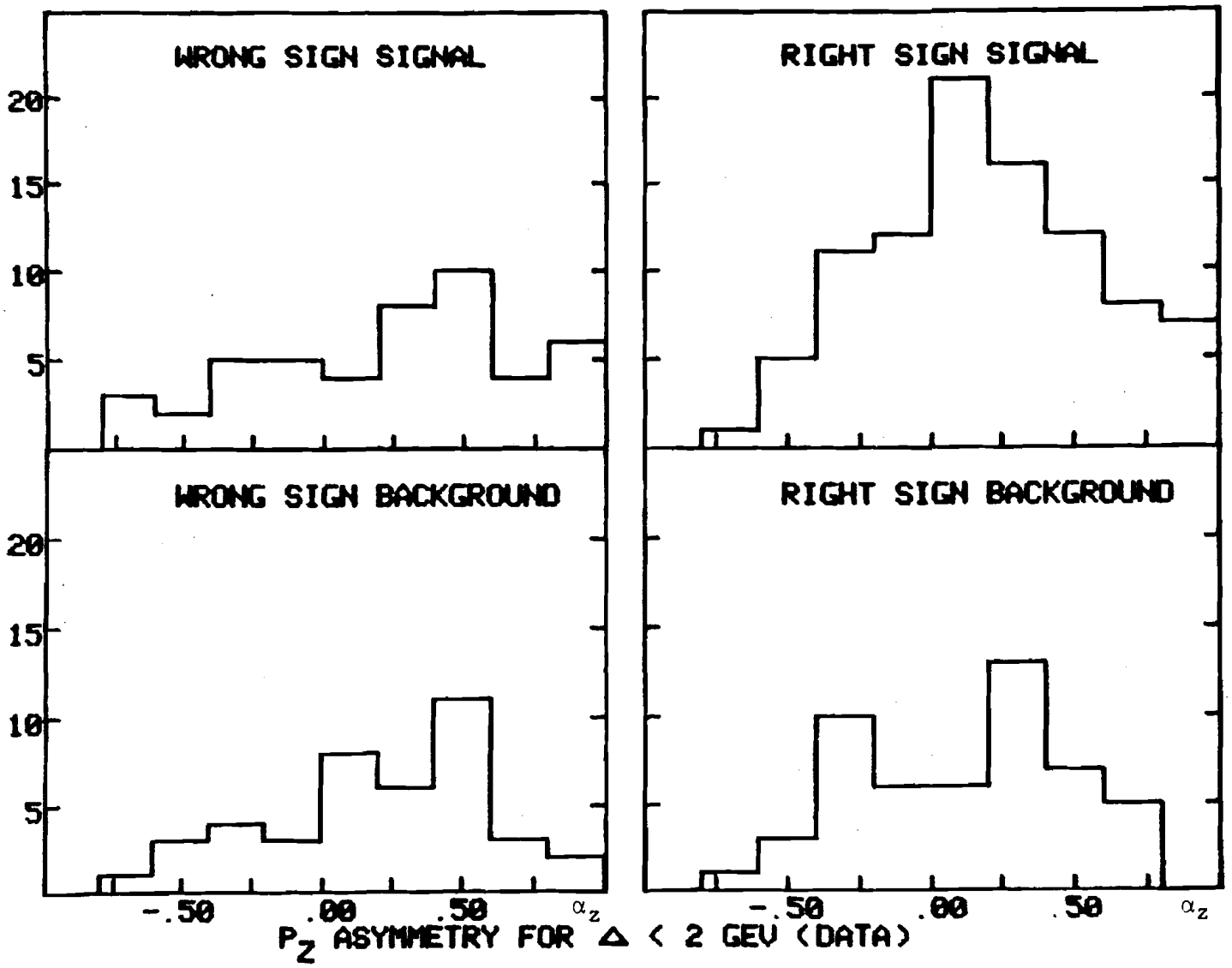
WRONG SIGN SIGNAL
RIGHT SIGN SIGNAL
WRONG SIGN BACKGROUND
RIGHT SIGN BACKGROUND
20
15
10
5
-.50
.00
.50
α_z
P_Z ASYMMETRY FOR Δ < 2 GEV (DATA)

Figure 6.14

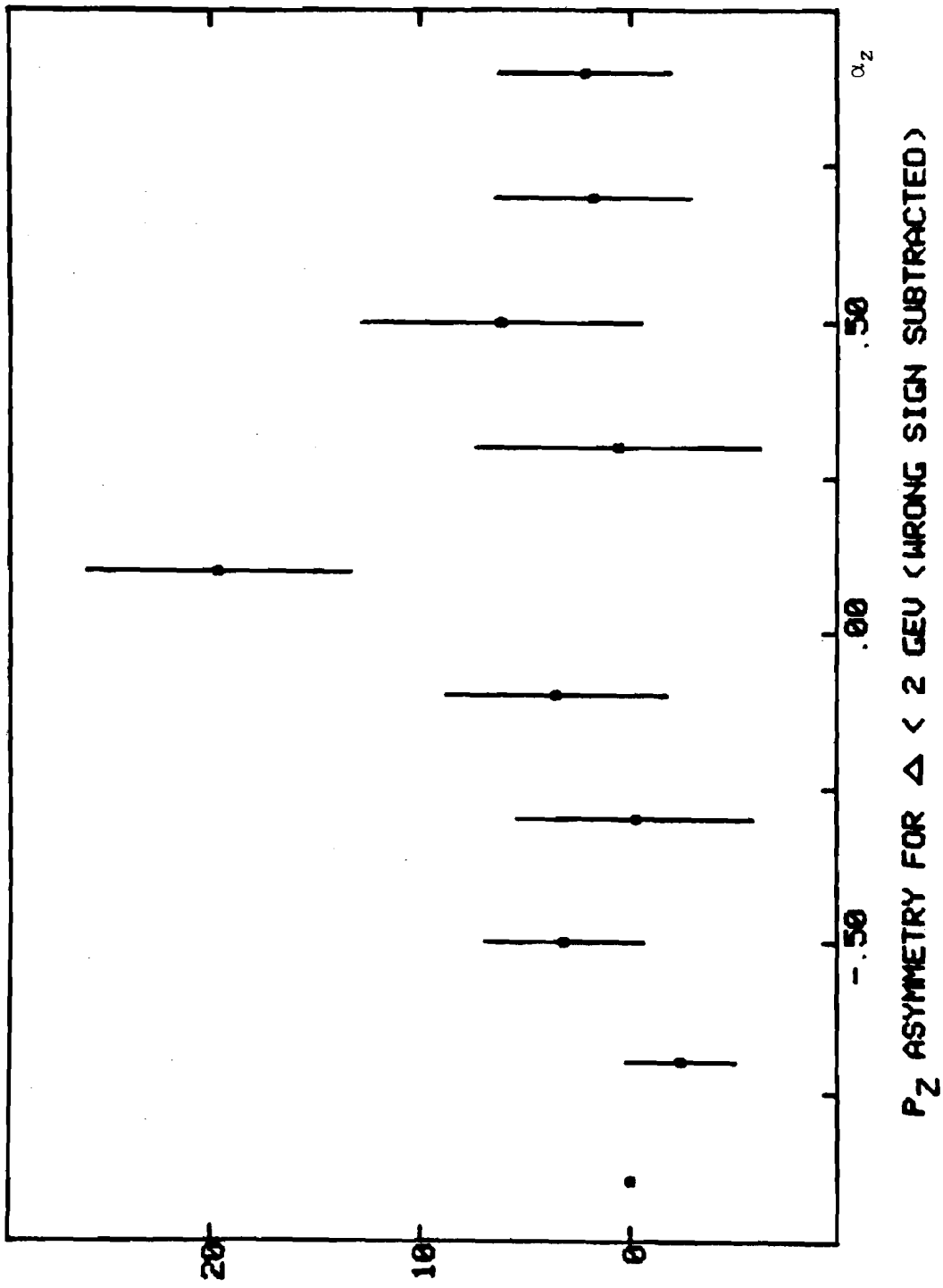
20
10
0
-.50
.00
.50
α_z
P_Z ASYMMETRY FOR Δ < 2 GEV (WRONG SIGN SUBTRACTED)

Figure 6.15

assuming that there is no signal in this region. The true number of cascade pions can then be estimated as

$$\text{cascade pions} = (42 \pm 12)-(85/71)(6 \pm 9.4) = 35 \pm 16$$

The number of right sign pions is expected to be slightly larger than the number of wrong sign ones because of charge conservation, which requires that the sign of the observed D* be compensated in the recoil state. Using our total D* event sample of 143 ± 20 events, the $D^{*+} \rightarrow \pi^+ D^0$ branching fraction of .60 ± .15, and the cascade pion acceptance of .90 ± .10, we can derive the fraction of $D^{*+}D^{*-}$ events as

$$\frac{\sigma(\gamma + N \rightarrow D^{*+}D^{*-})}{\sigma(\gamma + N \rightarrow D^{*+} + X)} = .45 \pm .25$$

We can compare this to the D*D* fraction obtained by the recoil charged K study performed earlier if we assume that all of the D 's inferred from that result come from D^{*-} decay. This yields

$$(.57 \pm .33)/(.60 \pm .15)=.95 \pm .60$$

which is very weak but consistent with the fraction obtained by the cascade pion analysis.

Another handle on the state recoiling against the D* can be obtained from the multiplicity distribution shown in fig. 6.16. From this distribution, which was obtained by fitting the Kπ mass spectrum for every unit of multiplicity, we estimate the average recoil charged multiplicity to be 2.31 ± .45. This number can be corrected for acceptance and compared to the multiplicity expected for various production mechanisms. These latter numbers can be estimated from the SPEAR measured values {12}

$$\langle n_{ch}^{D0} \rangle = 2.46 \pm .14$$
$$\langle n_{ch}^{D+} \rangle = 2.16 \pm .16$$

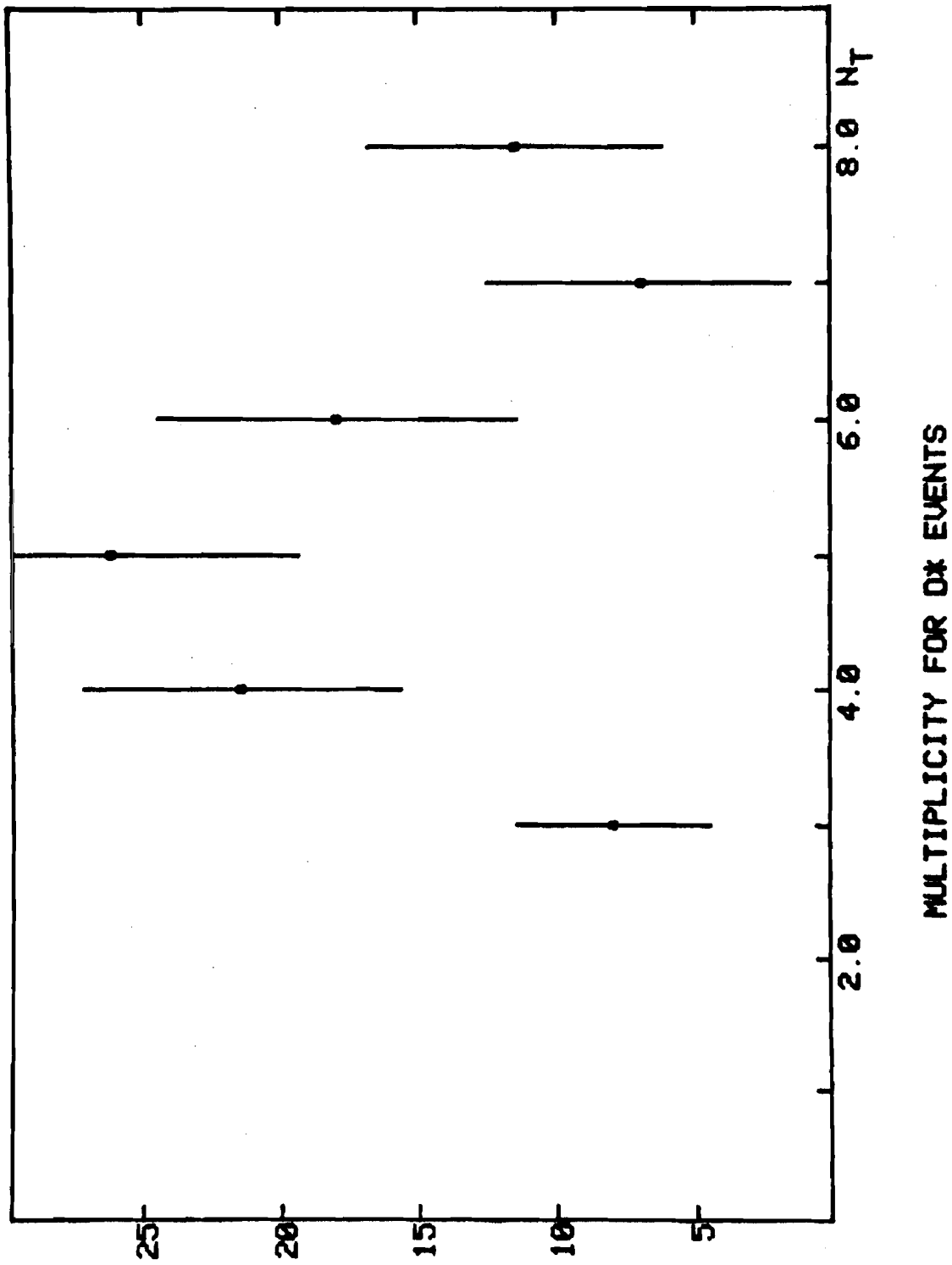

Figure 6.16

For the additive acceptance correction, we use the diffractive model discussed in the next section, with modifications introduced as necessary to generate extra pions at the D*D* vertex (we use uniform phase space). The table below summarizes the experimental and predicted charged multiplicities for 4 D* production mechanisms:

Process	Correction	Obs. Mult	Predicted Mult.
$D^{*+}D^{*-}$	.60	2.91 ± .45	2.92 ± .22
$D^{*+}D^{-}$	.60	2.91 ± .45	2.16 ± .16
$D^{*+}\overline{D^{0}}\pi^{-}$	.54	2.85 ± .45	3.46 ± .14
$D^{*+}D^{-}\pi^{+}\pi^{-}$	.78	3.09 ± .45	4.16 ± .14

If $D^{*+}D^{*-}$ and $D^{*+}D^{-}$ were the only allowable production mechanisms, then the observed averaged charged multiplicity would imply that the $D^{*+}D^{*-}$ fraction is 100 ± 65%, which is inconsistent by 1.5 standard deviations with all $D^{*+}D^{-}$ production. This result is consistent with the cascade pion measurement of this fraction of 45 ± 25%, which is independent of any assumption regarding other possible mechanisms.

The table above shows that the data is inconsistent with all D* production taking place with an extra charged pion, although some of this process can certainly be accomodated within the error bars of the measurement. However, if the photon is in a pure isospin state (I=0), then $D^{*+}D^{-}\pi^{0}$ production occurs at 1/2 the rate of $D^{*+}\overline{D^{0}}\pi^{-}$ production, which implies, from the table above, that virtually any amount of single extra pion production can be accomodated within the measurement errors because the two processes add compensating contributions to the observed multiplicity.

The issue of extra pion production arises because of the observation in our data that 16 ± 5% of all D* events have a recoil mass (obtained by assigning the pion mass to every particle outside the D* combination) larger than the D* mass. This effect is not seen in a Monte Carlo simulation of

D*D* production, but occurs at approximately the right level for $D^{*+}\ \bar{D}^0\pi^-$ production. Possible explanations include the presence of stray muons generated at the primary target upstream of our detector or fake tracks found by the reconstruction program. Both of these effects appear to be too small to account for the number of events with large recoil mass.

Section D^* Cross Section

The first step in obtaining a reliable cross section is the selection of a model which broadly reflects the observed characteristics of the signal and does not contradict other existing data from e+e- storage rings. We present one such model below primarily to illustrate the errors and efficiencies which make up a cross section calculation, and also to give a first estimate of the size of D^{*+} production. Other models will be discussed at some length in the next chapter.

The model we choose, diffractive pair photoproduction of $D^{*+}D^{*-}$, is motivated by the following observations:

1. SPEAR data convincingly demonstrate {8} that all D's are produced in association with either D's or D*'s, a result that is certainly not contradicted in our own data , as evidenced by the comparable numbers of D^{*+} and D^{*-} events and the observation of recoil K's.

2. 75% of our D* candidates have P_t^2's less than 1 GeV^2/c^2.

3. The average fraction of visible energy retained by the D* is .6 ± .1, which, because of the systematic underestimate of the total energy, is consistent with 1/2 of the incident photon energy.

4. The average multiplicity of the D^* events is consistent with a $\bar{D}$ or $\bar{D}^*$ recoiling against the observed D*.

5. Evidence has been presented that about 1/2 of the D* events are of the form $D^{*+}D^{*-}$, where the $D^{*+}D^{*-}$ system has a P less than 2 GeV/c.

Having convinced ourselves that a diffractive model is at least reasonable, we shall now fix its parameters in order to generate Monte Carlo

events. We assume a flat cross section in energy and select photon energies from 50 to 200 GeV according to the spectrum depicted in fig. 2.2. The joint D*D* mass is then generated from threshold to infinity according to M^{-7}, a parameterization that roughly reproduces the observed D* transverse momentum dependence.

The mechanism of a psion decay into D*D* (3 spin 1 objects) is governed by a matrix element containing two independent amplitudes ; hence it is not possible to predict either the angular distribution of the decay or the spin alignments of the D*'s. However, there are theoretical estimates {41} which show that these distributions might be consistent with uniform processes. We will assume that the D*'s are produced via a uniform angular distribution and, furthermore, that the spin axes of the D*'s are randomly oriented independently of each other. The latter assumption of course implies that the angular distribution of each D* decay must be uniform in its own center of mass because all spin directions are equally possible. Although we are not particularly sensitive to the angular correlations since the two D mesons are produced near threshold, we will include a 20% systematic error to account for this and other uncertainties in the model.

For purposes of this model, the D^{*+} always decays into $D^0\pi^+$, where $D^0 \dashrightarrow K^-\pi^+$ or $K_S\pi^+\pi^-$, depending on the process we want to measure. The D^{*-} fragments according to one of two statistical isospin models proposed by Quigg and Rosner {42}, which were constructed in such a way as to roughly reproduce the observed charge particle multiplicities in D and ψ decays. All acceptances in this thesis are based upon their so-called "Constant Matrix Element" (cme) model, although the efficiencies vary by only 1% of their values in changing to their "statistical" model.

With the model defined, we can now discuss the remaining cross section parameters, namely, dead times, luminosity, and small correction factors. The number of observed D^{*+} events can be expressed in terms of the cross section as:

$$N = \{FntL_1L_2\} \cdot Acc \cdot Corr \cdot \sigma(\gamma + N \text{ --> } D^{*+})$$

where
- N is the number of D^{*+} events actually observed
- σ is the D^{*+} production cross section/nucleon
- Acc is the detector acceptance (Geometry, Trigger)
- F is the total number of photons on target
- n is the nucleon density (nucleons/cm^3)
- t is the target thickness
- L_1 is the master gate livetime (.87)
- L_2 is the DC logic livetime (.89)
- Corr includes miscellaneous correction factors (K in-flight decays, track absorption, etc)

An implicit linear A dependence has been used in the above formula to infer the cross section per nucleon.

The number of photons on target is obtained indirectly from measurements of the quantameter charge Q, whose values were recorded at the end of each spill as mentioned in chapter 2. The quantameter was calibrated in a 90 GeV electron beam and provided a direct measurement of total beam power. This information must be supplemented by knowledge of the beam energy distribution to yield the total flux. The spectrum shape is obtained from a 3 exponential fit to the photon energy distribution shown in fig. 2.2.

$$dN/dE = \begin{cases} N_0 \exp(-E/20) & 0 < E < 25 \text{ GeV} \\ .468 N_0 \exp(-E/51) & 25 < E < 200 \text{ GeV} \\ 1.218 N_0 \exp(-E/41) & 200 < E < 400 \text{ GeV} \end{cases}$$

We are only interested in photon energies between 50-200 GeV, thus, using our definition above for F,

$$F = 8.482 N_0 = \int dE \cdot dN/dE$$

The total power of the beam is

$$P = 1226.1N_0 = \int dE\ E\ dN/dE$$

Using the measured quantameter calibration constant of 8510 ions/GeV, we finally obtain $N_0 = 3.829 \times 10^{13}$.

We can now estimate the quantity in brackets in the cross section formula above. For the runs we are including in our data sample, the "live" Q (already including livetime) sums to .0640 coulomb. Multiplying the factors in brackets together then yields an effective "live" luminosity of

$$L(50\text{-}200) = 602 \pm 60 \text{ events/nb}$$

where a 10% systematic error has been included to account for possible measurement uncertainties in obtaining this number.

The quantity Corr contains several correction factors listed below.

1. K in-flight decay. This is very difficult to measure in principle since it is not at all clear what decay distance to use. This distance lies between P3 and P4 since the K must be identified by the Cerenkov counters. We use the average distance of C1 and C2 coupled with the K momentum spectrum determined from a Monte Carlo to yield a decay non-probability of .94 ± .02, with the error reflecting the difference between C1 and C2.

2. Track absorption in the target and other material. This is estimated to be approximately 2 ± 2% per track. The correction for the D* (3 tracks) then becomes .94 ± .06.

3. Cerenkov counter inefficiency due to "unused on" problem. This correction has been discussed in chapter 4 and is estimated to be .95 ± .05.

4. There is a 5% correction for events which are thrown out because they have 200 or more total hits in the MWPC's.

5. Bussline 9 (multiplicity) has a certain inefficiency due to extra hits generated in the MWPC's. Although this correction is multiplicity dependent (see table below), we estimate its value to be .873 ± .05 for events containing a D*, using the multiplicity distribution in fig. 6.16.

Bussline 9 Inefficiency vs Multiplicity

Tracks	Inefficiency
3	.032
4	.046
5	.102
6	.158
7	.219
8	.300

Multiplying these individual corrections together yields a total correction factor Corr=.696 ± .08

We are now in a position to calculate the D^{*+} production cross section. Fig. 6.17 shows the ΔM and $K\pi$ mass distributions for accepted Monte Carlo events. Applying the same ΔM cut ($.1425 < \Delta M < .148$ GeV/c^2) as imposed on the data, we obtain 920 events via a Gaussian fit. For 20000 events generated, this implies an overall acceptance of 4.6 ± .92%, where a 20% systematic error has been included to account for model uncertainties. This overall acceptance sequentially factorizes approximately as

45%	$K\pi\pi$ Geometric acceptance
35%	K Identification probability
35%	Energy trigger efficiency
90%	MWPC Bussline logic acceptance

The D* events used in the cross section determination were required to have the correct busslines set for the main trigger and lie in a period of running known to be free from trigger changes. In addition, a cut of Evis < 200 GeV was imposed to match the range for the luminosity calculation. The number of events satisfying these criteria is (93 ± 17)/2, where the factor of 2 is included to count only D^{*+}.

The cross section formula now becomes

$$L \cdot B \cdot \sigma(\gamma + N \rightarrow D^{*+}) \cdot Acc \cdot Corr = (93 \pm 17)/2$$

where L = 602 ± 60 events/nb
Acc = .061 ± .012
Corr = .696 ± .08

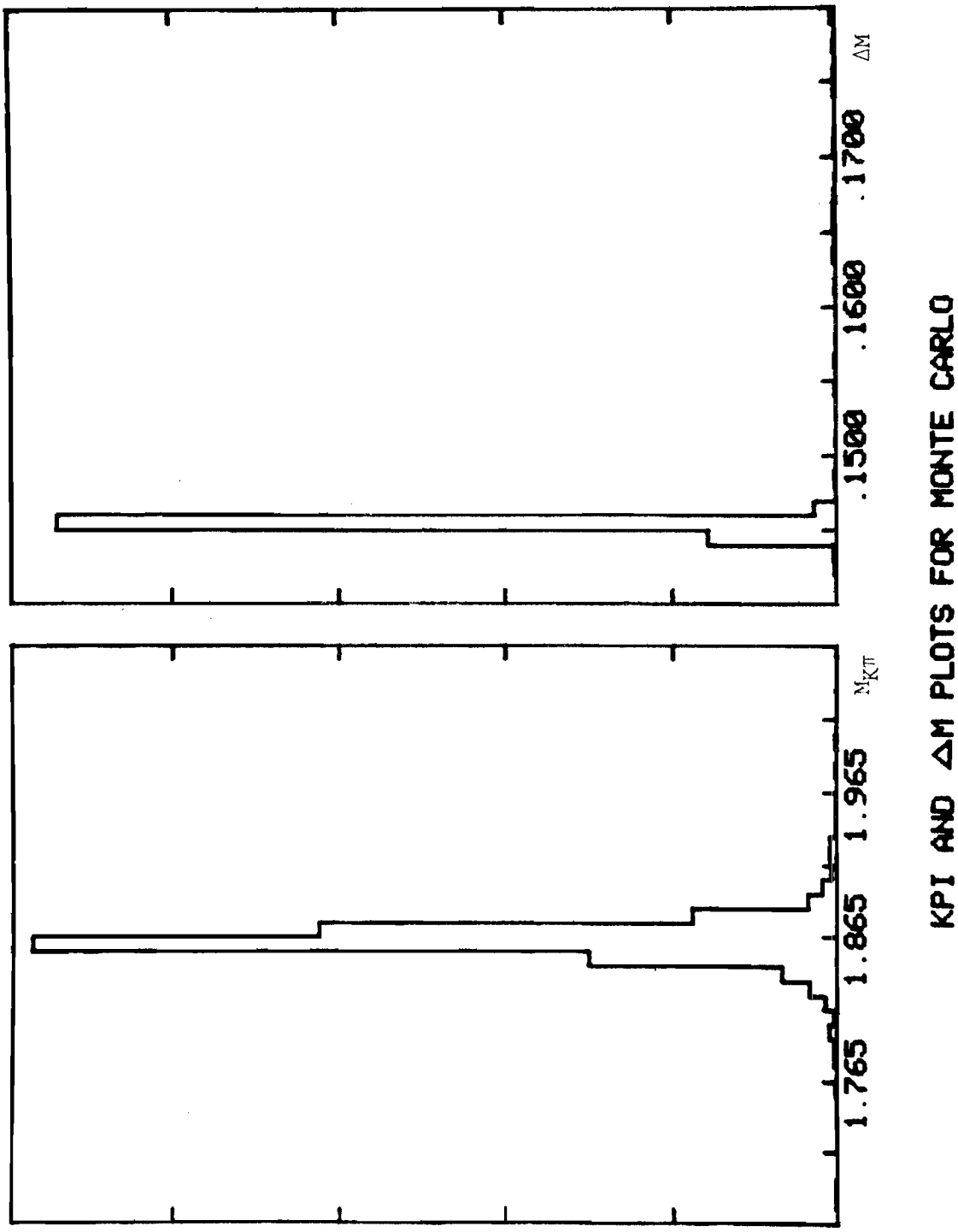
1.765
1.865
1.965
$M_{K\pi}$
.1500
.1600
.1700
ΔM
KPI AND ΔM PLOTS FOR MONTE CARLO

Figure 6.17

This yields $\sigma(\gamma + N \rightarrow D^{*+})\ B(D^{*+} \rightarrow D^0\pi^+)\ B(D^0 \rightarrow K^-\pi^+) = 2.4 \pm .77$ nb/nucleon.

The branching fractions are known from SPEAR measurements {40} to be

$$B(D^{*+} \rightarrow D^0\pi^+) = .60 \pm .15$$
$$B(D^0 \rightarrow K^-\pi^+) = .025 \pm .005$$

Including these numbers we finally arrive at the D^{*+} production cross section of 160 ± 70 nb/nuc.

The relative branching ratio of $D^0 \rightarrow K_0\pi^+\pi^-$ to $D^0 \rightarrow K^-\pi^+$ can be estimated using the same techniques. The Monte Carlo efficiency, including a 20% systematic uncertainty, is .0506 ± .011. The correction factor Corr must be modified to reflect the lack of an in-flight K decay and Cerenkov inefficiency and must include an extra 4 ± 4% absorption factor for the 5 body final state. The new correction factor now becomes Corr = .634 ± .11.

The same fiducial cuts applied on the $K\pi$ data are now imposed on the $K_s\pi\pi$ signal with the exception that the ΔM cut is much tighter ($.1445 < \Delta M < .1465$ GeV/c^2) in order to improve the signal to noise ratio. Because of magnetic field problems, the efficiency of this cut cannot be determined from the Monte Carlo simulation which predicts a much narrower ΔM distribution (see fig. 6.17) than is seen in the data. However the $K\pi$ signal can be used to establish this cut efficiency through simultaneous fits to the mass distribution with and without the tight ΔM cut. This yields an efficiency for this cut of .70 ± .10.

The fiducial cuts imposed on the $K_s\pi\pi$ data actually suffice to bring out the the D signal without the added multiplicity requirement used in fig. 6.2. A fit to this signal yields 42 ± 17 events. The relative branching ratio of $K_0\pi\pi$ to $K\pi$ can then be written

$$R = \frac{(42 \pm 17)}{(143 \pm 20)} \frac{(Acc2)}{(Acc1)} \frac{(Corr2)}{(Corr1)} \frac{1}{.34\varepsilon}$$

where Acc1 = $K_S 3\pi$ efficiency .0506 ± .01
Acc2 = $K\pi\pi$ efficiency .046 ± .0092
Corr1 = $K_S\pi\pi$ correction factor .634 ± .11
Corr2 = $K\pi$ correction factor .696 ± .08
ε = efficiency of tight ΔM cut (.70 ± .10)
.34 = branching ratio of $K_0 \rightarrow \pi^+\pi^-$

The above numbers yield R=1.6 ± .7, a value that is bracketed by the only other measurements completed {40} at the time of this writing: 1.8 ± .8 (LGW) and .96 ± .3 (MARK II).

Section E Inclusive D Signal

The evidence we have presented on the D* signal naturally raises the question of whether we can see a $K\pi$ D^0 signal without the ΔM requirement. Fig. 6.18 shows the $K\pi$ mass spectrum subject to no cut save that the K must be identified by the Cerenkov system. The curve is a fit to an exponential background plus Gaussian signal. The fit yields a 3σ effect at 1.861 GeV/c^2 that cannot be discerned by the naked eye because of the magnitude of the statistics. The second plot in fig. 6.18 shows the same data with the background component of the fit subtracted from both the histogram and the fitted curve. An enhancement of 730 ± 230 events can now be seen at about the right position for the D^0. The mass centroid found by the fitter is 1.857 ± .006 GeV/c and the FWHM is .032 ± .016 GeV/c^2.

If the FWHM is fixed at .023 GeV/c^2, the value found for the ΔM constrained signal, we obtain

N = 551 ± 190 events
M = 1.861 ± .006 GeV/c^2

The cross section for D^0 production can be calculated using the same Monte Carlo model used for D*D* production except that the soft pion acceptance of .90 ± .10 must be factored out. The acceptance now becomes .051 ± .011. In addition, we must remove the effect of the $D^{*+} \rightarrow D^0\pi^+$

where Acc1 = $K_S 3\pi$ efficiency .0506 ± .01
Acc2 = $K\pi\pi$ efficiency .046 ± .0092
Corr1 = $K_S\pi\pi$ correction factor .634 ± .11
Corr2 = $K\pi$ correction factor .696 ± .08
ε = efficiency of tight ΔM cut (.70 ± .10)
.34 = branching ratio of $K_0 \rightarrow \pi^+\pi^-$

The above numbers yield R=1.6 ± .7, a value that is bracketed by the only other measurements completed {40} at the time of this writing: 1.8 ± .8 (LGW) and .96 ± .3 (MARK II).

Section E Inclusive D Signal

The evidence we have presented on the D* signal naturally raises the question of whether we can see a $K\pi$ D^0 signal without the ΔM requirement. Fig. 6.18 shows the $K\pi$ mass spectrum subject to no cut save that the K must be identified by the Cerenkov system. The curve is a fit to an exponential background plus Gaussian signal. The fit yields a 3σ effect at 1.861 GeV/c^2 that cannot be discerned by the naked eye because of the magnitude of the statistics. The second plot in fig. 6.18 shows the same data with the background component of the fit subtracted from both the histogram and the fitted curve. An enhancement of 730 ± 230 events can now be seen at about the right position for the D^0. The mass centroid found by the fitter is 1.857 ± .006 GeV/c and the FWHM is .032 ± .016 GeV/c^2.

If the FWHM is fixed at .023 GeV/c^2, the value found for the ΔM constrained signal, we obtain

N = 551 ± 190 events
M = 1.861 ± .006 GeV/c^2

The cross section for D^0 production can be calculated using the same

branching fraction of .60 ± .15 and adjust the track absorption correction by .02 ± .02 to reflect fact that there is one less track in the mass combination. Performing the above operations and using the representative value of 660 ± 230 events for the D^0 inclusive sample, which represents a composite of fits made with different binning schemes and free parameters, we obtain

$$\sigma(\gamma + N \text{ --> } D^0) = 390 \pm 190 \text{ nb/nucleon}$$

The ratio of D^{*+} to D^0 inclusive production can now be computed as

$$\frac{\sigma(\gamma + N \text{ --> } D^{*+})}{\sigma(\gamma + N \text{ --> } D^0)} = .40^{+.22}_{-.11}$$

CHAPTER 7

MODEL DEPENDENCE

Section A The Photon Gluon Fusion Model

We will discuss in this chapter the mass, P_t, energy, etc. distributions of the D* events and compare them to the prediction of two models. The first model, diffractive pair production ("psion" model) was described in the previous chapter in obtaining the cross section. Although it is not a true dynamical model in the sense that it has a field theoretic underpinning, it does offer a convenient parameterization of the production mechanism in terms of physically measurable quantities such as energy, P_t, and mass. By adjusting the distributions of these variables to match the data, we can constrain certain parameters of dynamical models which attempt to predict these distributions.

The second model, photon gluon fusion, was described in chapter 1. The photon is pictured as interacting with a constituent gluon of the nucleon to produce a $c\bar{c}$ pair, as shown in the Feynman diagram of fig. 1.2(b). Each quark in the pair then "dresses" itself with unit probability according to some fragmentation function into either charmed mesons and baryons or cc bound states (ψ, ψ', etc.).

Several simplifying assumptions must be made in order to perform calculations in this model and make comparisons with the data. First, as in most parton model calculations, the photon nucleon cross section into charm is written as a convolution of the gluon distribution inside the nucleon with the elementary QCD process photon + gluon --> $c\bar{c}$, where the gluons are assumed to be free and on their mass shell with spin parity J^P = 1-. The photon gluon cross section can then be taken directly over from the QED process photon + photon --> e+e-, by replacing the electron mass by the quark

mass and putting in appropriate QCD vertex factors.

For the nucleon gluon distribution we take the sea quark-like parameterization discussed in chapter 1, namely

$$G(x) = (n+1)(1-x)^n/16x$$

where x is the fraction of longitudinal momentum carried by the gluon and the normalization factor 1/16 allows the 8 types of gluons to carry 1/2 the total nucleon momentum, as inferred from electroproduction {23}. The value of n has been the subject of some discussion, with n=5 expected from constituent counting rule arguments {24} and n=10 preferred from fits to ep and μp deep inelastic scattering {25}. We can study this issue further by comparing ψ photoproduction data with with the model prediction under the assumption that ψ production takes place in the region $4M_c^2 < M_{c\bar{c}}^2 < 4M_D^2$, where $M_{c\bar{c}}$ is the mass of the $c\bar{c}$ system and M_c and M_D are the c quark and D meson masses respectively. The quantitative comparison of the ψ data with the gluon fusion prediction is shown in fig. 7.1 for n=10 and fig. 7.2 for n=5. The solid curve shown is a fit to the world photoproduction data {43}, and is parameterized by 33nb exp{-37.5/(s-12.15)}, where s is the center of mass energy squared. The rise in cross section with energy appears to be reproduced best by the curves obtained with n=5, while the n=10 curves seem to increase too slowly to their asymptotic values. Selecting M =1.65 GeV as the quark mass gives the best ageement with the absolute cross section, but this comparison should not be taken too seriously because the ψ is expected to take only a fraction of the total bound $c\bar{c}$ cross section. A similar study has been performed by Weiler {32} who obtains n=5.6 ± 1 as the value which best reproduces the shape of the ψ excitation curve.

Secondly, the model assumes that the c quarks dress themselves, without changing direction, into physical mesons or baryons according to some

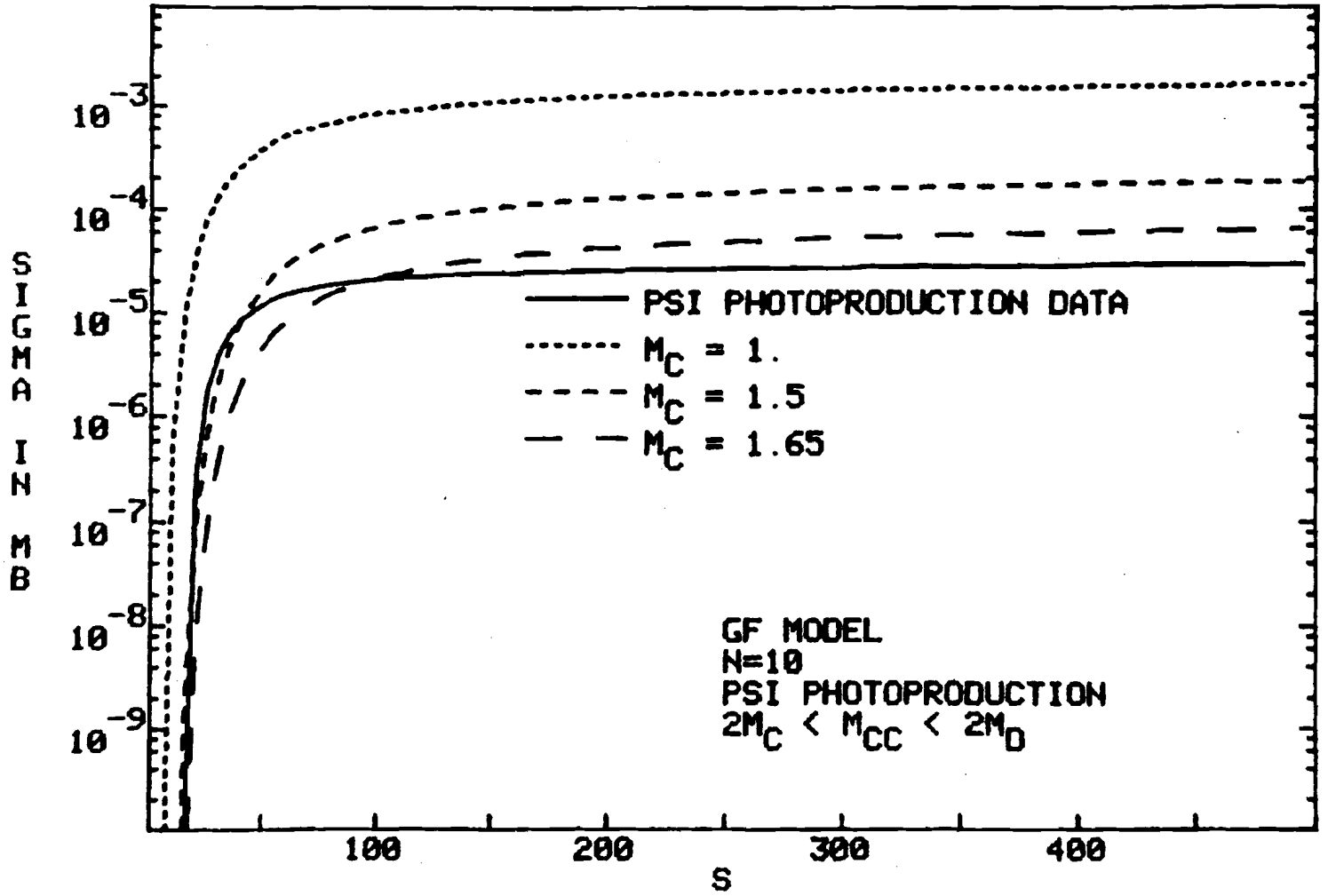

BOUND CHARM PRODUCTION IN GLUON FUSION MODEL

Figure 7.1

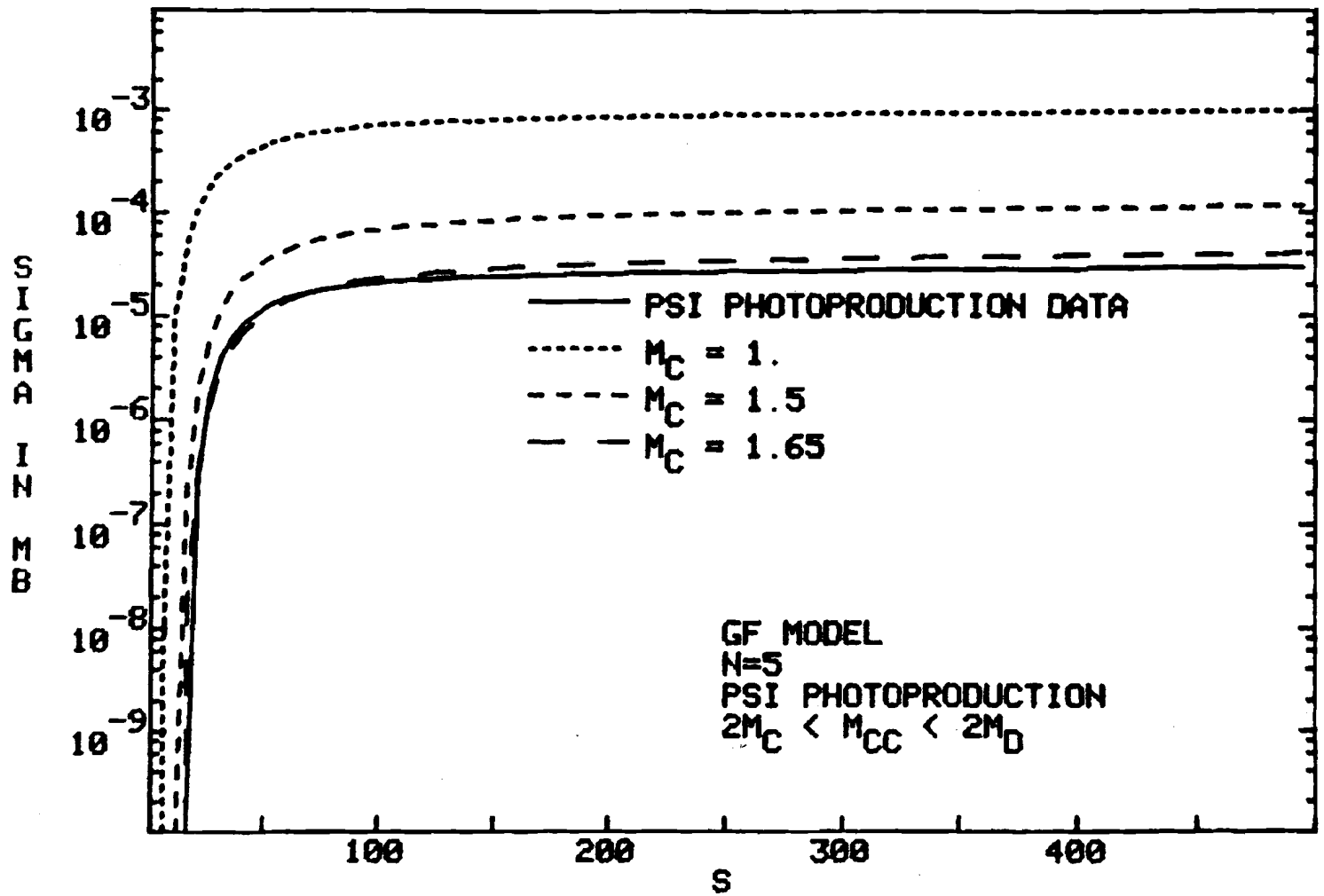

BOUND CHARM PRODUCTION IN GLUON FUSION MODEL

Figure 7.2

fragmentation function D(z), where z is the fraction of c quark energy retained by the charmed hadron in the photon gluon center of mass. As noted in chapter 1, some energy must be shed since the gluon carries an octet of color and physical hadrons must be color singlets. The color is assumed to "leak" off in the form of soft gluons, presumably via interactions with either the target or the other charmed particle.

Recent theoretical attempts {44} to calculate the c quark fragmentation behavior within the context of QCD have predicted fragmentation functions that peak at high z, i.e. the charmed hadron carries off a majority of the c quark energy, in contrast to the measured D(z) distributions for pions and kaons, which fall exponentially with z. Several authors have examined existing data to extract the c quark fragmentation information. Barger, Gottschalk, and Phillips {45} studied di-lepton data ($\mu\mu$, μe) from several neutrino experiments and concluded that that an exponentially falling D(z) distribution fits the positive lepton momentum spectrum and the $\phi(\mu^+,\mu^-)$ distribution somewhat better than a fragmentation function peaked at high z. They assumed that the positive lepton arises from D semi-leptonic decay. Odorico and Roberto {46}, on the other hand, found that a fragmentation peaked at low z is inconsistent with data from the CDHS {47} and Columbia-BNL {48} neutrino collaborations. They prefer a D(z) that is more or less flat in z.

Both of these comparisons to neutrino data suffer from the fact that one is trying to infer a momentum distribution of an unseen (and therefore assumed) D meson through convolutions with the neutrino energy spectrum, lepton energy distribution, and an assumed quark distribution within the nucleon. A more direct measurement of D(z) has been obtained in e+e- annihilation at s=49 GeV {49}. These data indicate that the D fragmentation

function falls like $\exp\{(-5.5 \pm 1.5)z\}$, very similar to the fragmentation of light quarks into pions and kaons.

All of the above studies, although not totally conclusive about the form of the D meson fragmentation functions, nevertheless appear to rule out any behavior where the D takes off almost all of the energy of the c quark. We will have more to say about this issue later in the chapter when we discuss the P_t dependence of the D*.

The original photon gluon fusion model proposed by Jones and Wyld {31} contained no provision for intrinsic gluon transverse momentum. An estimate for the value of this quantity can be determined by studying the P_t dependence of lepton pairs produced in nucleon collisions {50}. These data indicate that the average dilepton P_t increases from .6 GeV/c at M_{ll} = 1 GeV to 1-1.2 GeV/c at M_{ll} > 4 GeV, where M_{ll} is the di-lepton mass. Assuming that this transverse momentum arises from constituent motion, and dividing the dilepton P_t's by $\sqrt{2}$ to account for the fact that two of these particles must interact, we obtain .7-.9 GeV/c as the average transverse momentum of each constituent. In the calculations which follow, we parameterize the gluon transverse momentum as $\exp(-P_t/A)$ and simply add this momentum to the $c\bar{c}$ system.

With these observations, we can write the cross section for charmed pair production as

$$d\sigma = (d\hat{\sigma}/d\hat{t}) \cdot d\hat{t} \cdot G(x) \cdot dx \cdot \delta(M^2 - sx) dM^2$$

or

$$d\sigma = (d\hat{\sigma}/d\hat{t}) \cdot d\hat{t} \cdot G(M^2/s) \cdot dM^2/s$$

where $\hat{t} = (Pc - P_\gamma)^2$ = momentum transfer squared to the c quark
x = fraction of longitudinal momentum carried by the gluon
$G(x)$ = gluon distribution within the nucleon
M = mass of the $c\bar{c}$ system
$d\hat{\sigma}/d\hat{t}$ = the $\gamma g \rightarrow c\bar{c}$ differential cross section

$$d\hat{\sigma}/d\hat{t} = (16/9)(4\pi\alpha\alpha_s)K/M^4$$

and

$$K = \frac{X_1^2 + X_2^2}{2X_1X_2} + \frac{2M_c^2}{M^2}\frac{1}{X_1X_2} - \frac{2M_c^4}{M^4}\frac{1}{X_1^2X_2^2}$$

$$X_1 = (M_c^2-\hat{t})/M^2$$
$$X_2 = 1-X_1$$

If we include the quark fragmentation function D(z) and the gluon transverse momentum distribution $f(P_t)$, we obtain the full cross section formula:

$$d\sigma = (d\hat{\sigma}/d\hat{t})\cdot d\hat{t}\cdot G(M^2/s)\cdot dM^2\cdot D(z1)\cdot dz1\cdot D(z2)\cdot dz2\cdot f(P_t)\cdot dP_t\cdot 1/s$$

where z1 = Energy fraction of c quark retained by D^*
z2 = Energy fraction of c quark retained by D^*
P_t = transverse momentum of gluon

In order to generate events for such a complicated distribution, we employ the following algorithm. The equation above is integrated from threshold over all variables (all but the M integral can be performed analytically) to give a cross section dependent only on s, the square of the center of mass energy. This is folded in with our photon spectrum (fig. 2.2) to yield a distribution of produced events as a function of photon energy and then stored in a lookup table. The function $\hat{\sigma}(M) = \int(d\hat{\sigma}/d\hat{t})d\hat{t}$ must also be tabulated because it falls too rapidly with M for a generation scheme based on rejection to work efficiently.

One might think that a two dimensional table would need to be stored because s and M are linked together in the cross section formula. A glance at the formula, however, shows that the mixing only occurs in the gluon distribution function $G(M^2/s)$. Because of this simplification, we can generate the event in the following sort of "modified rejection" approach. First, a value of s is picked according to the total cross section table

mentioned above. A value of M is then selected according to the mass table and rejection is applied against the function $G(M^2/s)$, normalized to be always less than or equal to 1. If this value of M fails the rejection test, a new one is selected and tested again until the test is passed. Values for $\hat{t}$ are then chosen using a straightforward rejection technique, because the $\hat{t}$ distribution is relatively flat. z1, z2, and P_t are obtained by choosing a random number and analytically inverting the probability distribution function to solve for each variable. The physical event is now defined and the physical 4-vectors can be computed from these quantities. A Lorentz transformation must then be applied twice, once to transform the vectors to the photon-nucleon center of mass, and again to put them in the laboratory system.

Section B Comparison with P_t Distribution

The gloun fusion model has several parameters that are subject to varying degrees of uncertainty. These include: n, describing the gluon distribution function; the fragmentation function D(z); the intrinsic gluon P_t; and the charmed quark mass. Of these, only the quark mass turns out to have completely negligible effects on observable quantities (as seen by Monte Carlo studies), hence we shall fix its value at 1.65 GeV/c^2 {20} and ignore it hereafter. The other 3 parameters have been open to some theoretical debate, but each of them has a "preferred" value as determined from experimental data. These preferred values are: $D(z) = \exp[(-5.5 \pm 1.5)z]$, obtained from SPEAR {49}; n=5 determined from ψ photoproduction data {32}; and gluon P_t = .7-.9, inferred from dilepton production data {50}. In the discussion which follows, we shall try to assess our own sensitivity to each of these parameters by examining the D* P_t distribution.

The D* P_t distribution offers several powerful advantages for studying many D* production features: first, it has a very mild acceptance variation which insulates it from Monte Carlo uncertainties; second, it is independent of the incident photon energy because Lorentz transformations leave transverse momenta intact; third, its shape is sensitive to the threshold dependence of the charm meson joint mass because too broad a mass distribution would give the observed D* an unacceptably high P_t; and fourth, it is sensitive to the t distribution of the $c\bar{c}$ pair.

The data points within the P_t distribution in fig. 7.3 were obtained by fitting the $K\pi$ mass spectrum for each bin of transverse momentum, with the error bars reflecting the statistical uncertainties in the fit. The data used for this analysis were required to satisfy the same fiducial requirements used to obtain the 93 event sample used in the cross section determination. The comparison histograms are Monte Carlo predictions for a diffractive psion model having a D*D* mass dependence parameterized by $M^{-\alpha}$, where α varies from 3 to 12. The data appear to be reasonably described by α's in the range 5-10. No t dependence is included in these Monte Carlo results, although it is clear that any such t distribution would force α to even larger values.

Turning now to the gluon fusion model, we overplot in fig. 7.4 the D* P_t distribution expected for the case where the the D mesons take off all of the c quark energy, i.e. $D(z) = \delta(z-1)$. The comparison with the data shows that values of n of 10 or more are needed to even approximately reproduce the sharply peaked nature of the D* transverse momentum distribution. The addition of primordial P_t, as discussed in the beginning of this chapter, only worsens the discrepancy and we conclude that such "hard" fragmentation is inconsistent with our data.

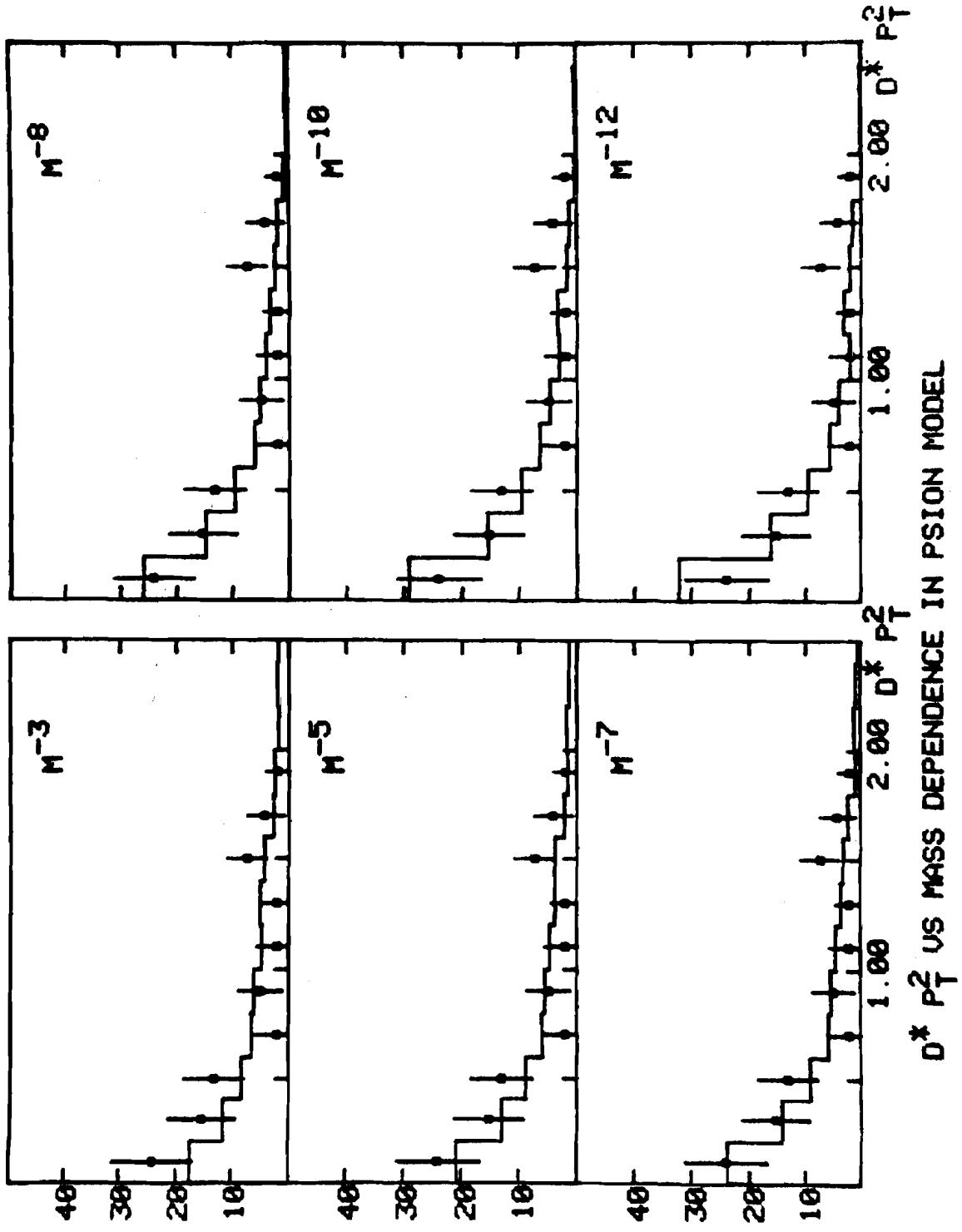
M-3
M-5
M-7
M-8
M-10
M-12
40
30
20
10
1.00
2.00
D* P_T^2
D* P_T^2 US MASS DEPENDENCE IN PSION MODEL

Figure 7.3

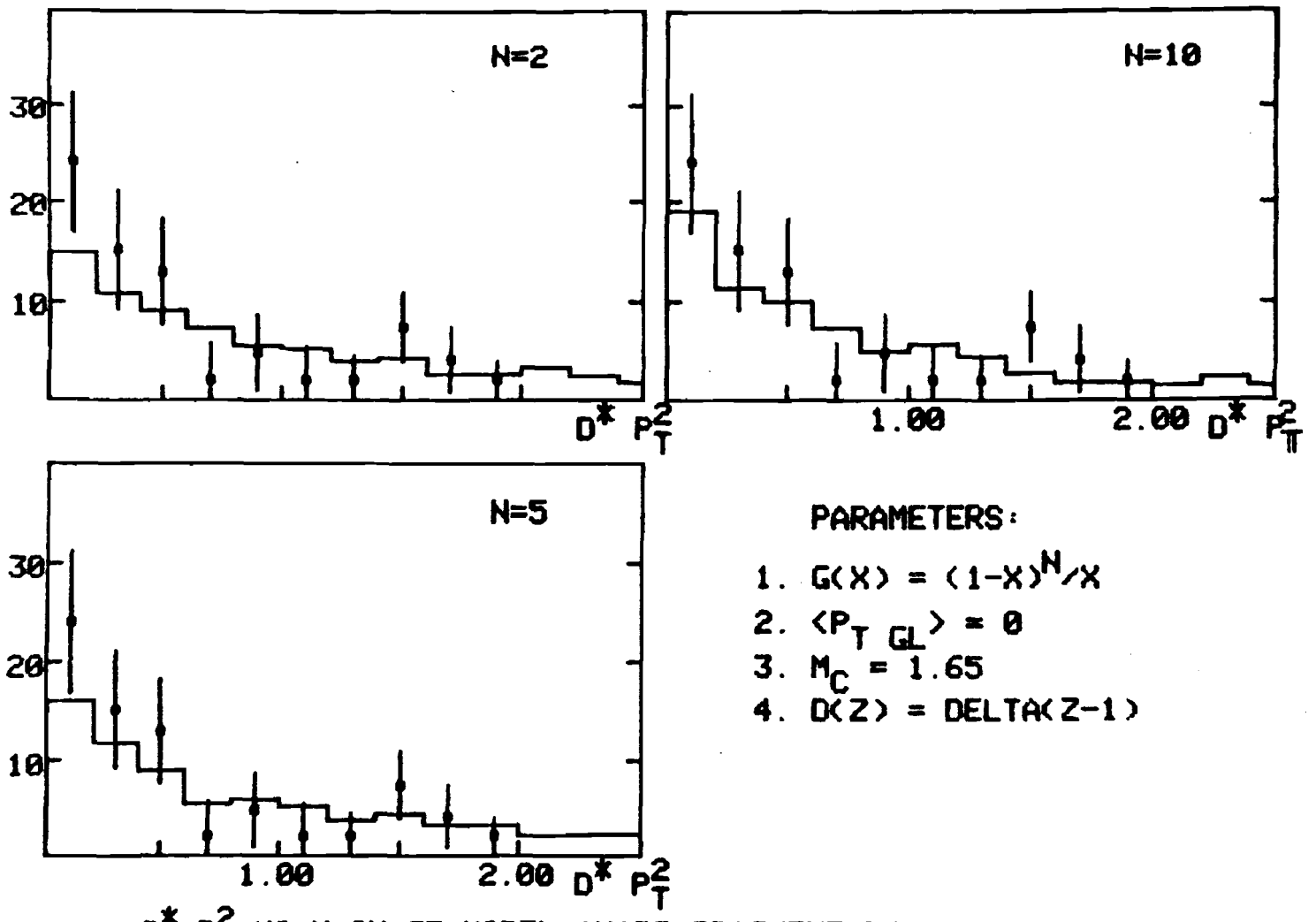

$D^* P_T^2$ VS N IN GF MODEL (HARD FRAGMENTATION)

Figure 7.4

In figs. 7.5-7.7 we compare the D* P_t distribution to gluon fusion predictions for 3 fragmentation functions and 3 values of the average gluon transverse momentum. We parameterize the fragmentation functions as D(z) = exp(Az), where values of A equal to -5.5, 0, and 5.5 are chosen to represent falling, constant, and rising behavior respectively. The value A=-5.5 is especially significant since it corresponds to the fragmentation behavior seen in e+e- annihilation, as discussed in section A. Surprisingly enough, the resulting P_t distributions show little dependence on the form of D(z). This apparent insensitivity is actually due to the fact that a large part of the production cross section takes place near the mass threshold of $4M_{D^*}^2$, hence we are kinematically limited to the high end of the z spectrum (z>.9 for most of the events) where the 3 functions cannot differ significantly from each other.

It is apparent from the comparisons shown in figs. 7.5-7.7 that the relatively large values of gluon transverse momentum inferred from dilepton production (.7-1 GeV/c) are necessary to reproduce the behavior shown by the D* P_t distribution. This extra P_t is needed to offset the effect of the "soft" fragmentation functions (such as the SPEAR parameterization exp(-5.5z) shown in fig. 7.5) described in this section, which tend to limit the phase space avaliable to the D* and thus squeeze the P_t to values near 0.

In choosing soft D(z) functions to represent fragmentation behavior, we also tend to lose some of the sensitivity to the value of n that was seen for the delta function parameterization of fig. 7.4. This is again a result of phase space suppression (due to values of z near threshold), which tends to minimize the variations between different values of n (fig. 7.8).

Within the context of the photon gluon fusion model, it appears that the D* P_t distribution does not support "hard" fragmentation behavior where the

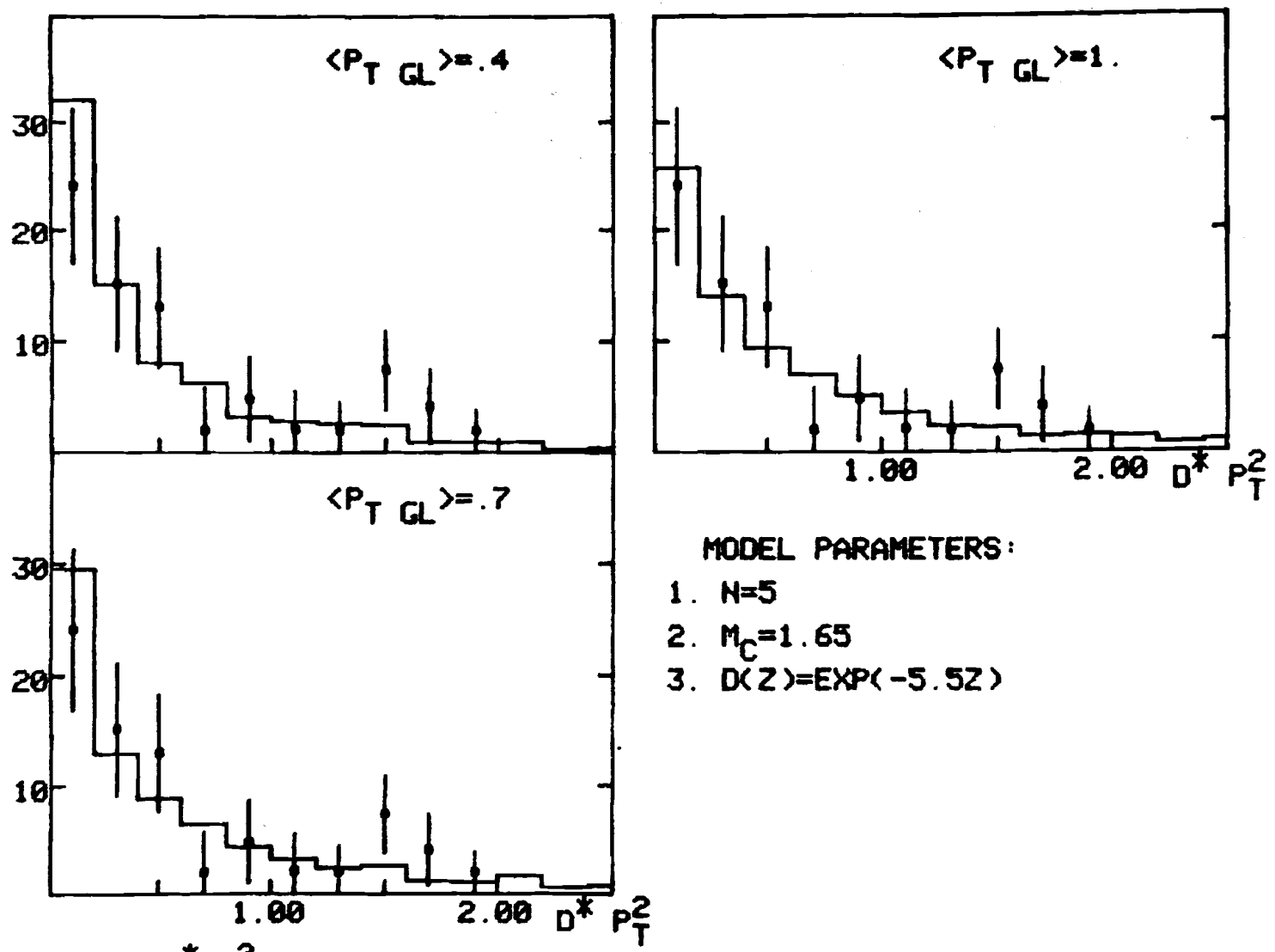

$D^* P_T^2$ DISTRIBUTIONS VS. AVERAGE GLUON P_T

Figure 7.5

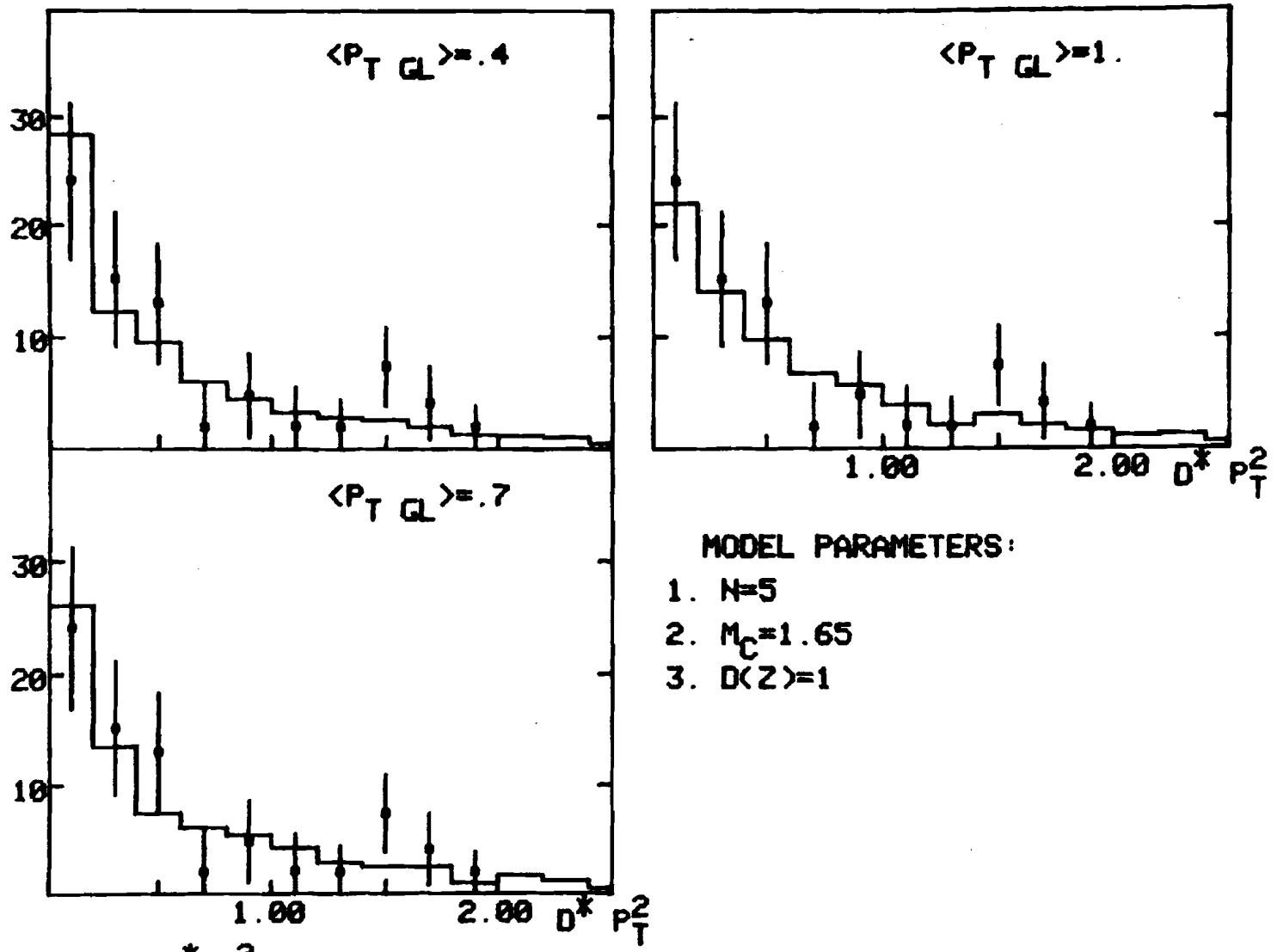

$D^* P_T^2$ DISTRIBUTIONS VS. AVERAGE GLUON P_T

Figure 7.6

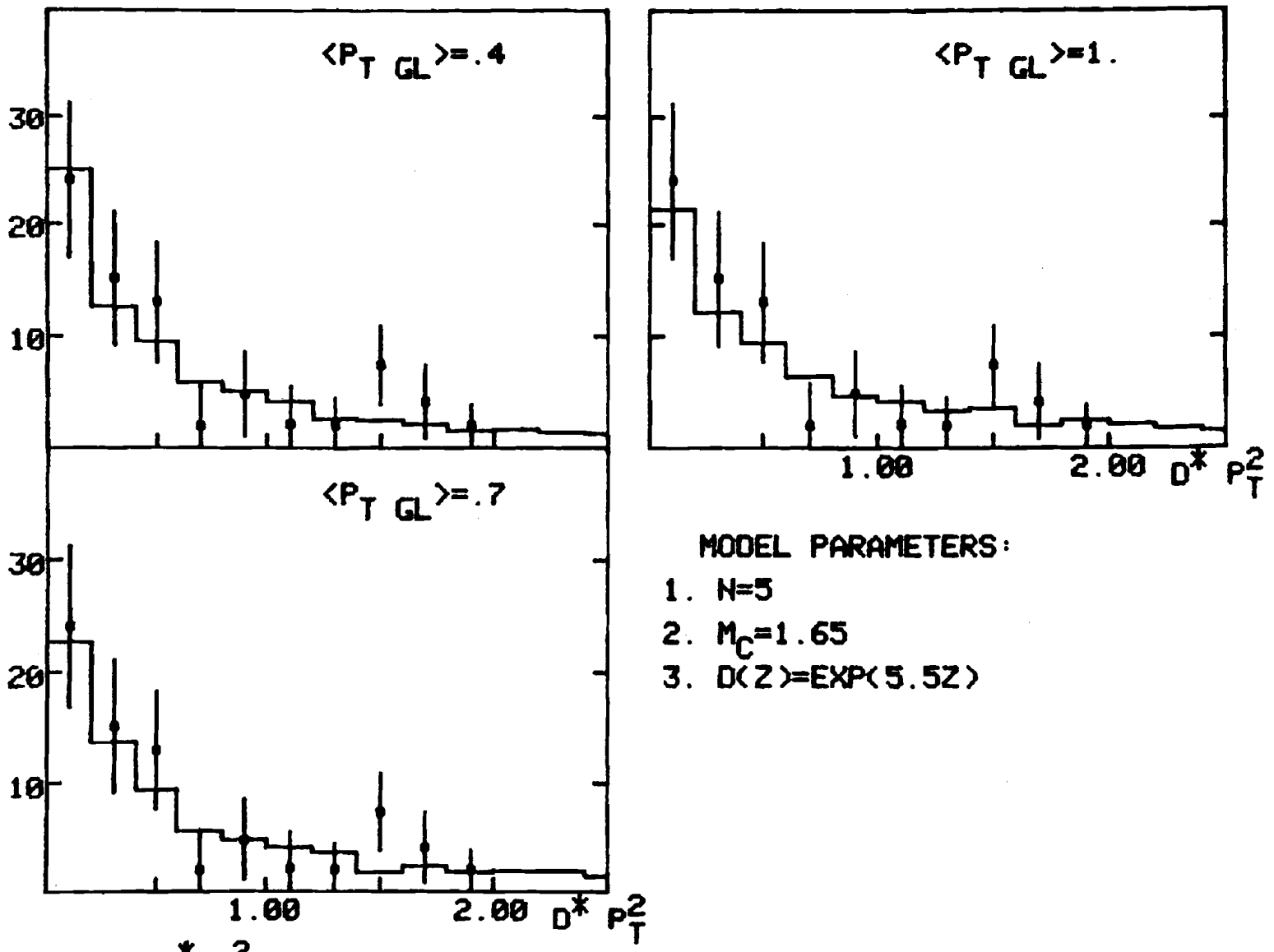

$D^* P_T^2$ DISTRIBUTIONS VS. AVERAGE GLUON P_T

Figure 7.7

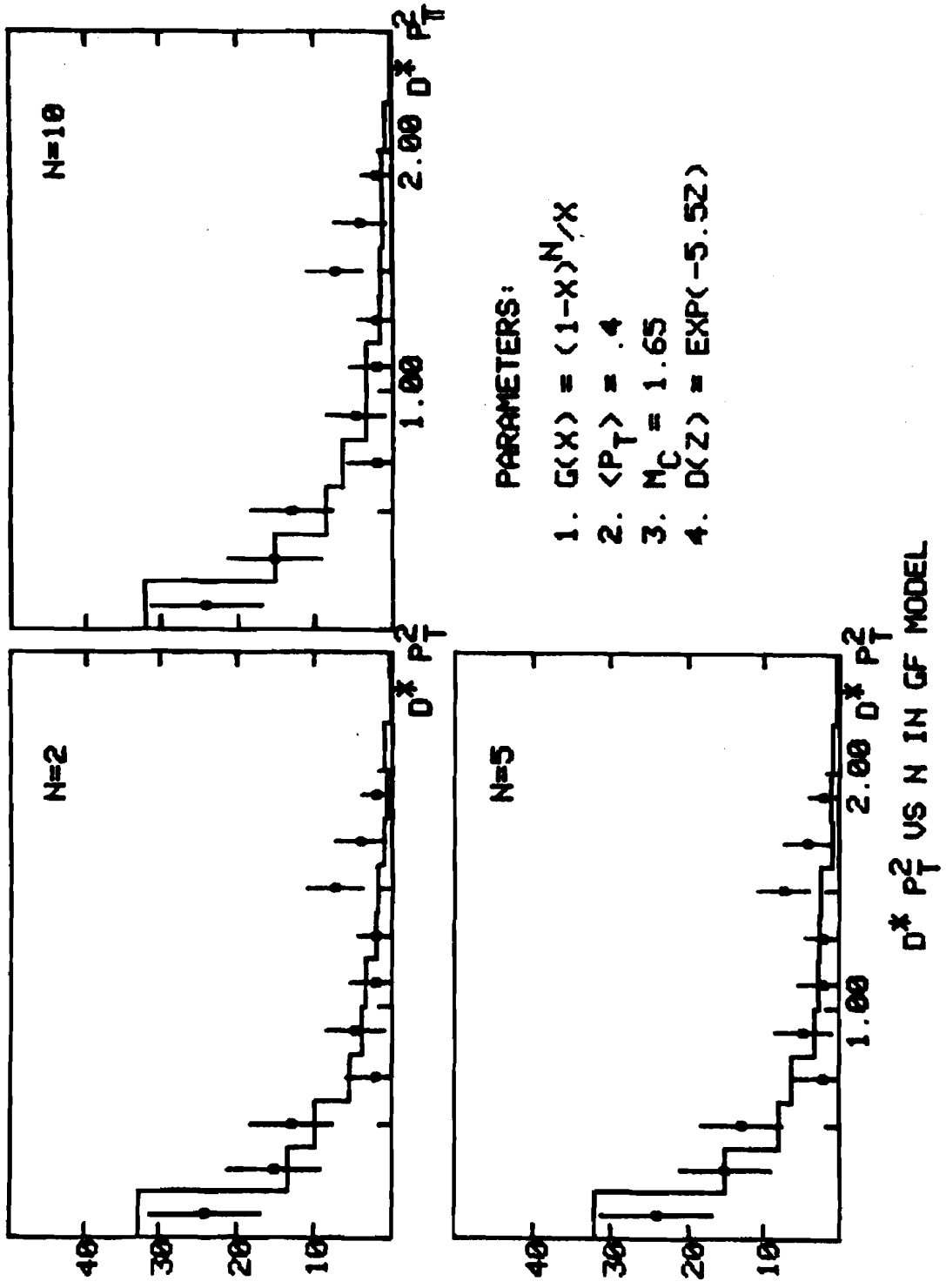
N=10
N=2
N=5
40
30
20
10
1.00
2.00
$D^* P_T^2$
PARAMETERS:
1. $G(X) = (1-X)^N/X$
2. $\langle P_T \rangle = .4$
3. $M_C = 1.65$
4. $D(Z) = EXP(-5.5Z)$
$D^* P_T^2$ VS N IN GF MODEL

Figure 7.8

D* takes almost all of the c quark energy, but prefers "softer" functions similar to those extracted from e+e- and neutrino data. If this smooth behavior holds then the relatively large values of gluon P_t (.7-.9 GeV/c) inferred from dilepton data must be included to adequately reproduce the D* P_t distribution. Beyond this little can be said. Low statistics and the fact that most of D* photoproduction is close to mass threshold prevent us from determining the form of D(z) because of the limited range in z. We also appear to be insensitive to the value of n, describing the gluon distribution inside the nucleon, once a smooth fragmentation function is selected.

Section C Comparison with Other Distributions

The evidence presented in chapter 6 argued strongly for a diffractive mechanism where the D* is accompanied by either a D or another D*. We present here further comparisons of D* distributions with the Monte Carlo predictions of the psion and photon gluon fusion models, using the same 93 event data sample that formed the basis of the P_t study in the last section. As usual, every data point shown is the result of a binned likelihood fit to the Kπ mass spectrum obtained for the appropriate bin of the variable under study, and the error reflects the statistical uncertainty of the fit. The Monte Carlo distributions are always normalized to the total number of events in the sample. Some of the variables studied in this section depend significantly on the detector acceptance, and one should be aware that small differences between the data and the simulation could arise from an imperfect understanding of the detector.

The parameters defining each model were selected to reproduce the observed D* P_t distribution. For the psion model, the joint D*D* mass was thrown as M^{-7}, and t was constrained to be 0. In the case of the gluon

fusion model, we chose n=5 describing the gluon distribution within the nucleon, the SPEAR result $D(z) = \exp(-5.5z)$ parameterizing c quark fragmentation behavior {49}, and $\langle P_t \rangle = 1$ GeV/c describing the net transverse momentum transferred to the $c\bar{c}$ system.

The D* energy dependence, shown in fig. 7.9, appears to be well described by both production mechanisms. These distributions, however, predict an anomalously large number of 6 track events compared to the data, as shown in fig. 7.10, although the overall agreement is reasonable. One must keep in mind that the multiplicity predictions may only mirror the deficiencies of the Quigg-Rosner statistical isospin model {42}, which has a somewhat higher average charged multiplicity than is observed for D's in e+e- annihilation {12}.

The total visible energy distribution in fig. 7.11 shows approximately the same behavior as evinced by the overplotted Monte Carlo distributions, except that the data appears to peak more sharply in the region 80-120 GeV. Actually the agreement is rather good considering that this variable is particularly sensitive to the acceptance cutoff at low photon energies, as well as to uncertainties in the fraction of neutral energy in D decay. This sensitivity can also explain why the distribution for the visible energy fraction retained by the D* (fig. 7.12) is slightly broader than either model prediction, although the data and Monte Carlo distributions peak at the same place. The fact that the peak occurs at energy fraction =.6 rather than .5 reflects our consistent underestimation of the total event energy.

The total visible mass spectrum shown in fig. 7.13 appears to be well represented by the Monte Carlo predictions. The model predictions are slightly narrower than the data, but uncertainties such as those discussed above for the visible energy distribution can easily account for this small

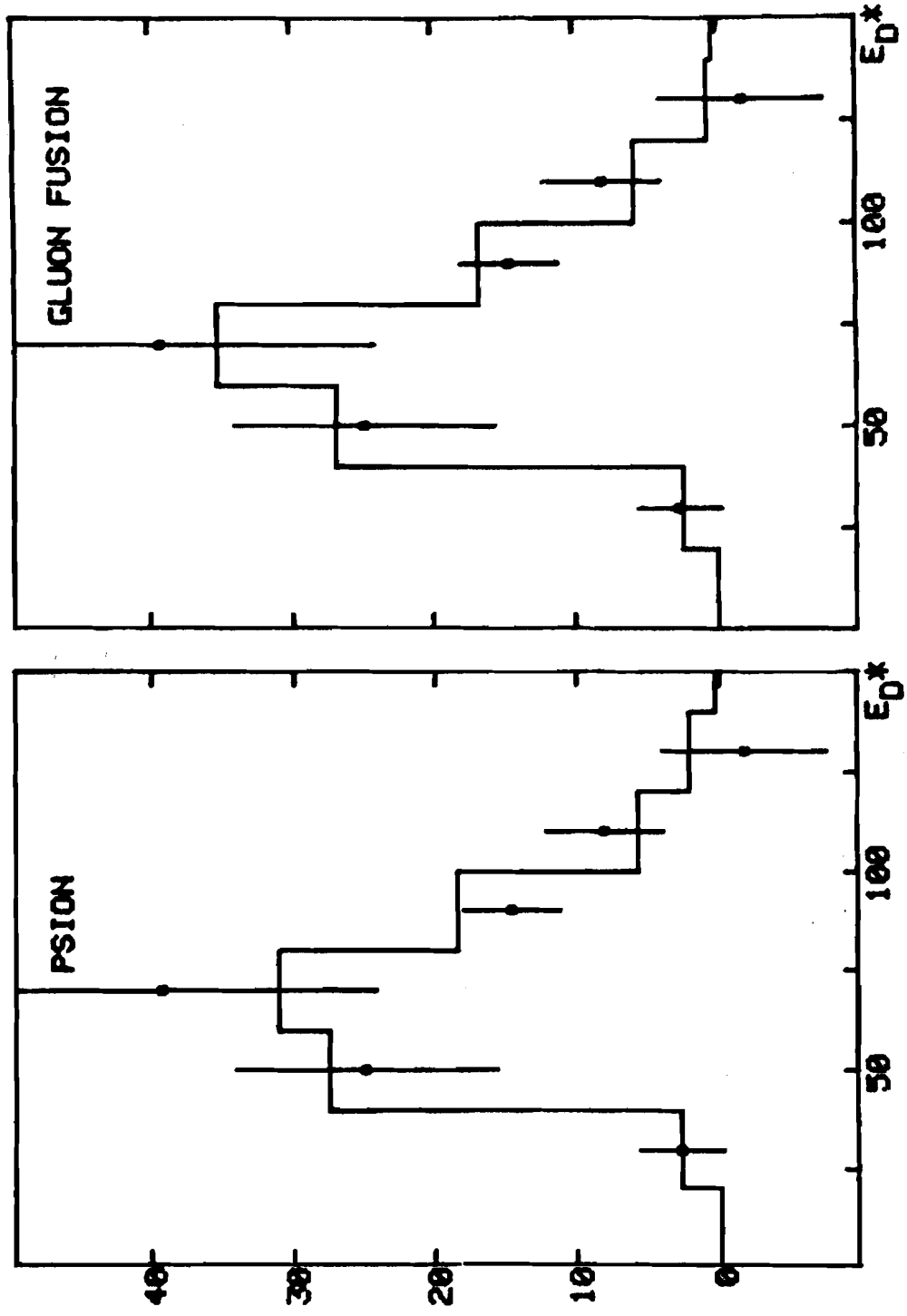
PSION
GLUON FUSION
40
30
20
10
0
50
100
E_D*
COMPARISION OF E_D* FOR PSION AND GF MODELS

Figure 7.9

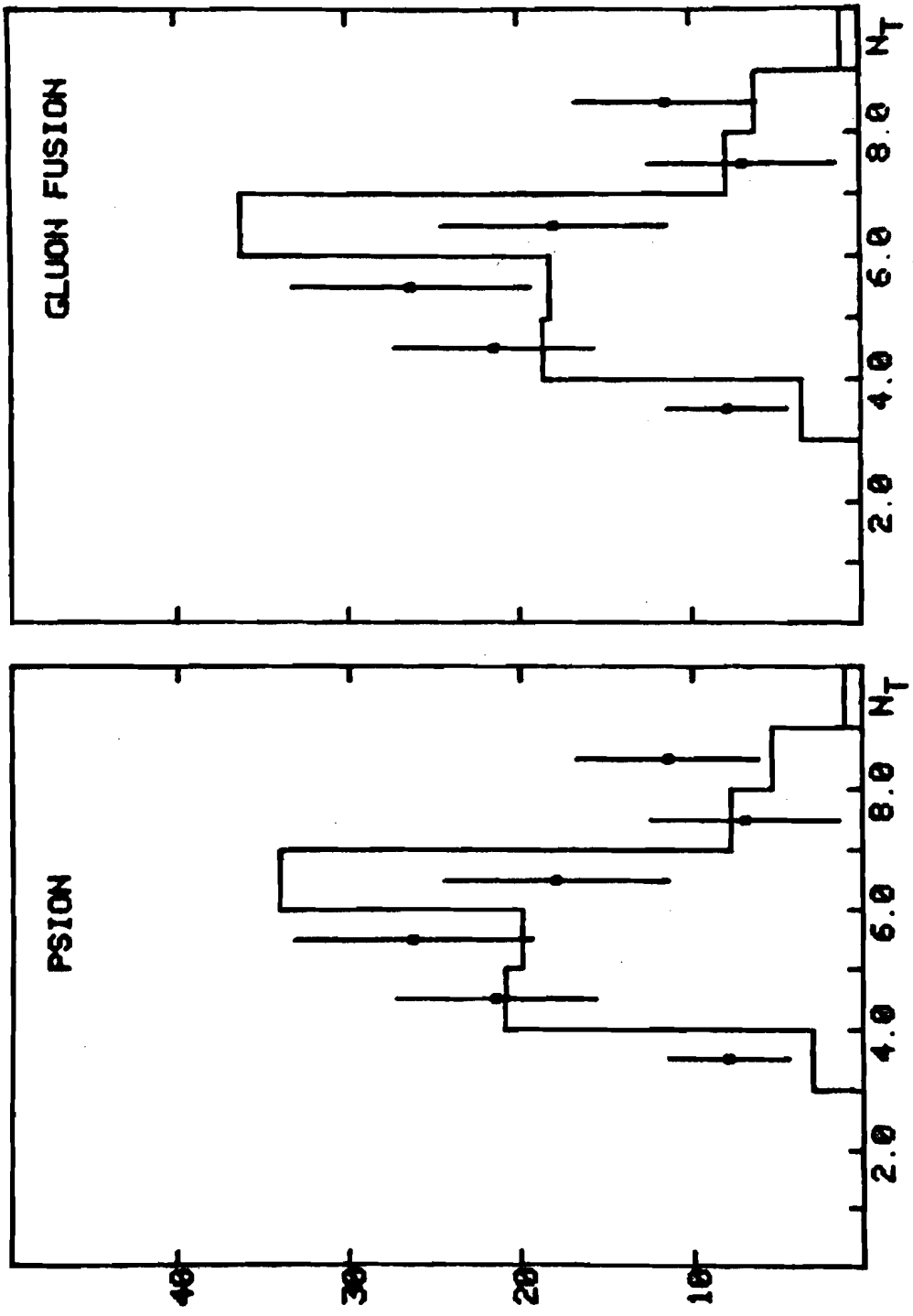

COMPARISON OF N_T FOR PSION AND GF MODELS

Figure 7.10

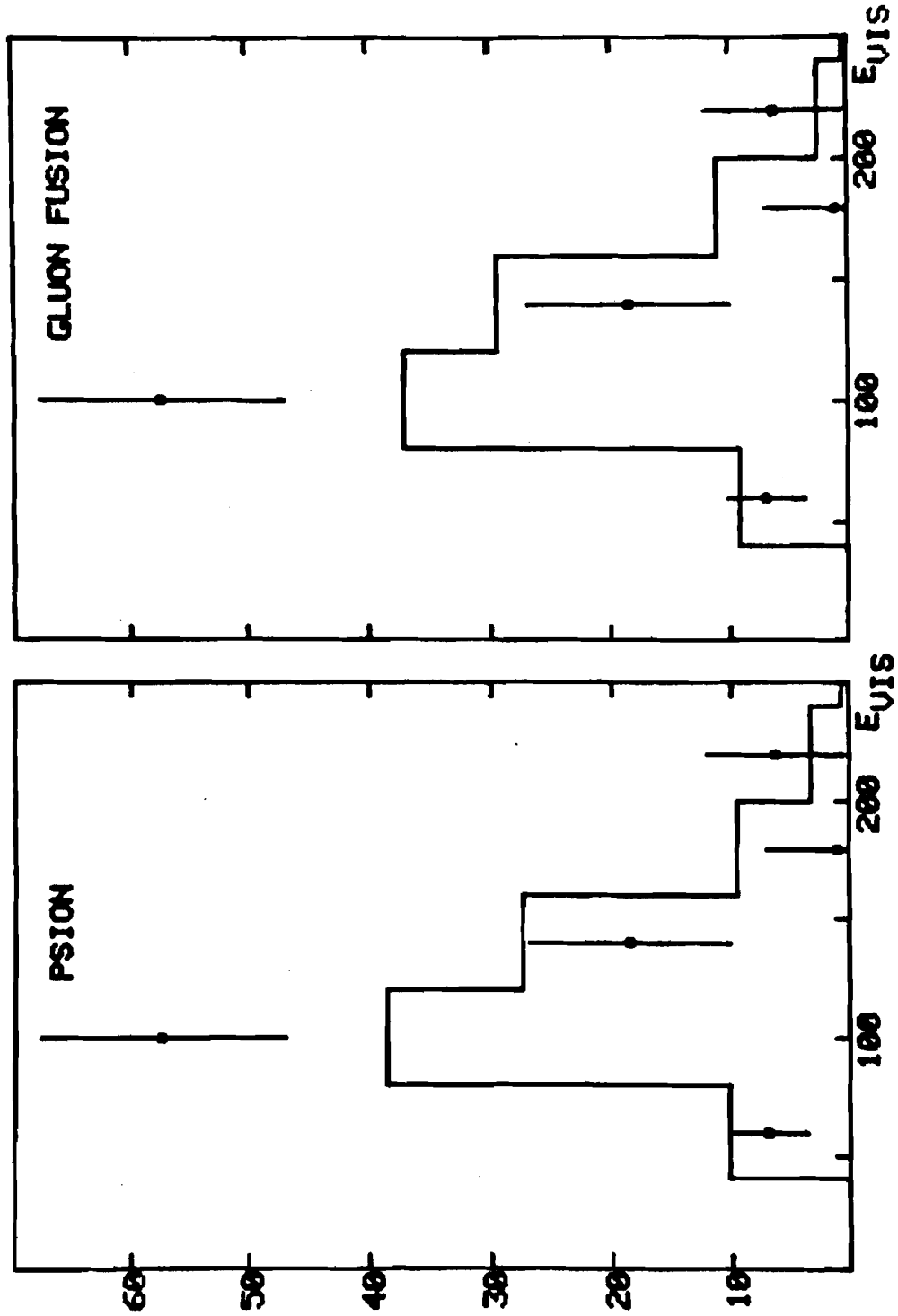

COMPARISON OF E_{VIS} FOR PSION AND GF MODELS

Figure 7.11

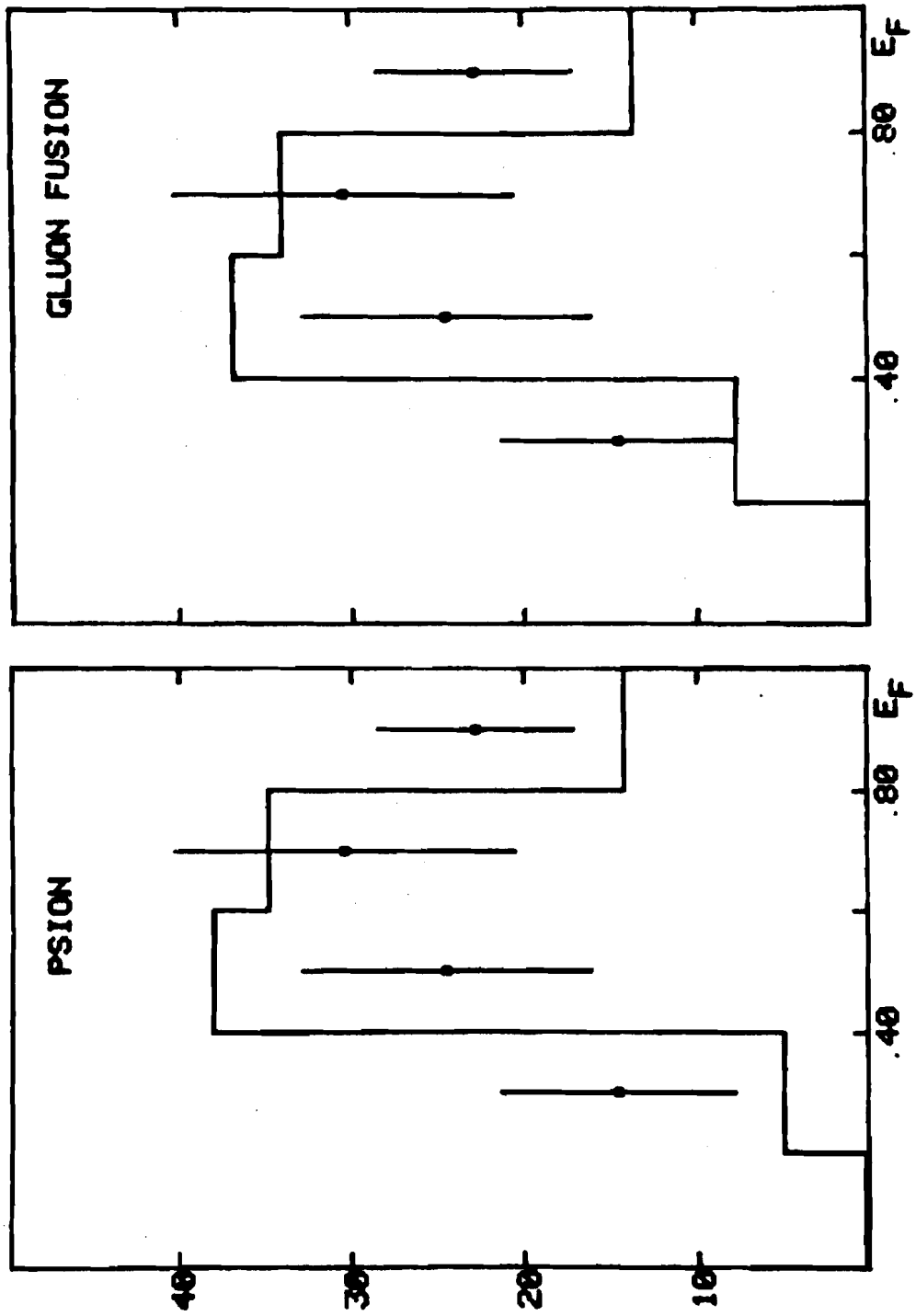

COMPARISON OF $E_F = E_D^*/E_{VIS}$ FOR PSION AND GF MODELS

Figure 7.12

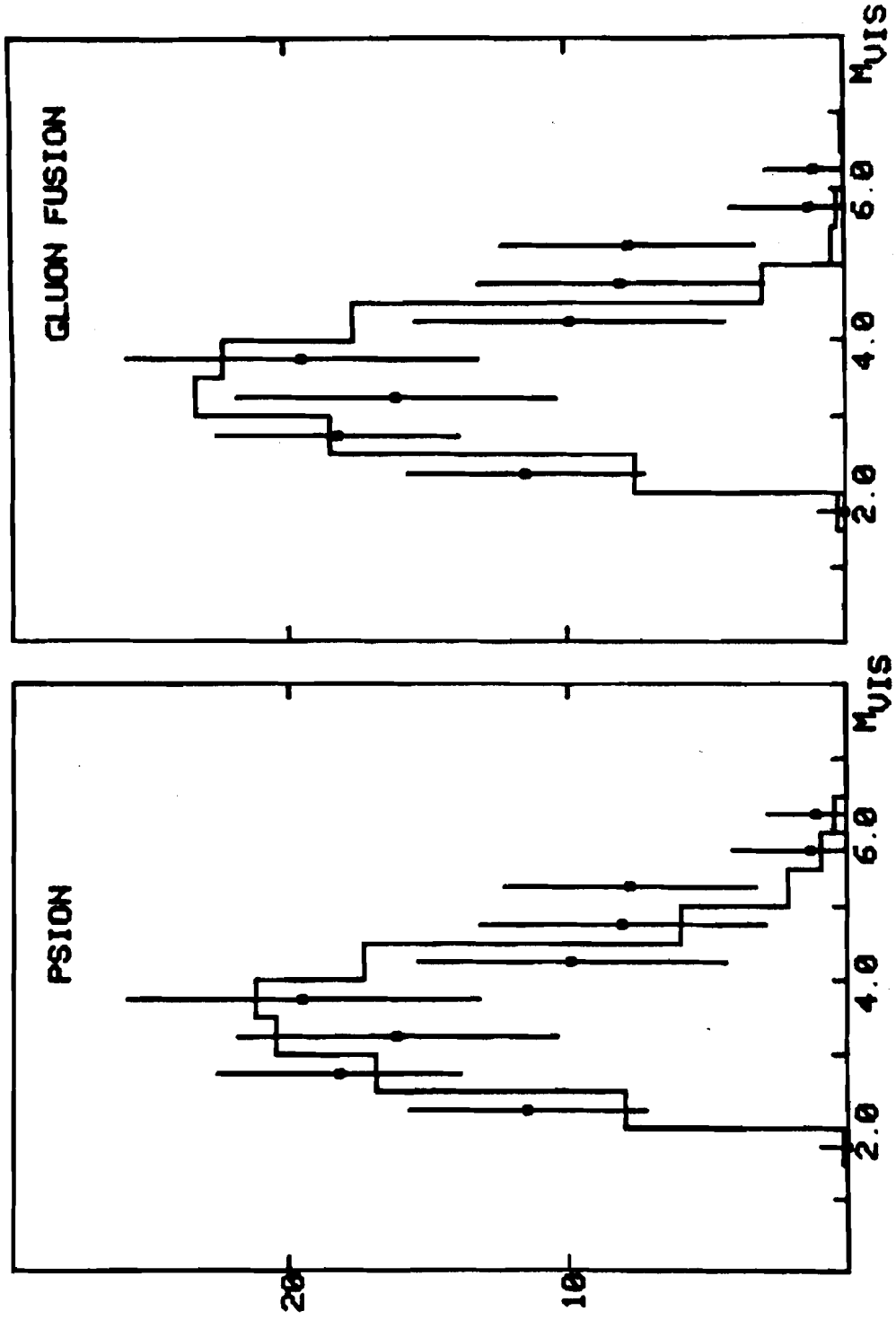

COMPARISON OF M_{VIS} FOR PSION AND GF MODELS

Figure 7.13

difference.

Overall, the agreement between the 2 diffractive models and experiment is very encouraging, if not striking. The low statistics, however, preclude us from preferring either mechanism on the basis of the distributions discussed in this section. One may legitimately question whether the comparisons shown here really imply agreement with diffractive behavior or merely reflect the shaping expected from detector acceptance. We can examine this issue by using background data taken from regions on both sides of the D peak and overplotting their inclusive distributions over those obtained for the D*. The background regions lie in the $K\pi$ mass interval $1.700 < M_{K\pi} < 1.800$ GeV/c^2 or $1.900 < M_{K\pi} < 2.000$ GeV/c^2 and are subject to the same ΔM requirement imposed on the D* signal, namely $.1425 < \Delta M < .148$ GeV/c^2. Some of the background distributions in fig. 7.14 and 7.15, namely the D* P_t^2 and D* energy plots, appear to be indistinguishable from the data, but the multiplicity, total visible energy, and D* energy distributions are sufficiently different from background to allow us to conclude that acceptance limitations do not preclude us from deducing diffractive behavior.

We remarked in chapter 1 that the three charm photoproduction diagrams in fig. 1.2 could be distinguished from each other using the energy dependence of the final state charmed hadrons. The results of this section clearly rule out significant contributions from either the Drell Yan-like graph of fig. 1.2(a), which predicts that the D* should carry a small fraction of the event energy, or the Halzen-Scott diagram of fig. 1.2(c), which predicts that one of the charmed particles should carry almost all of the energy.

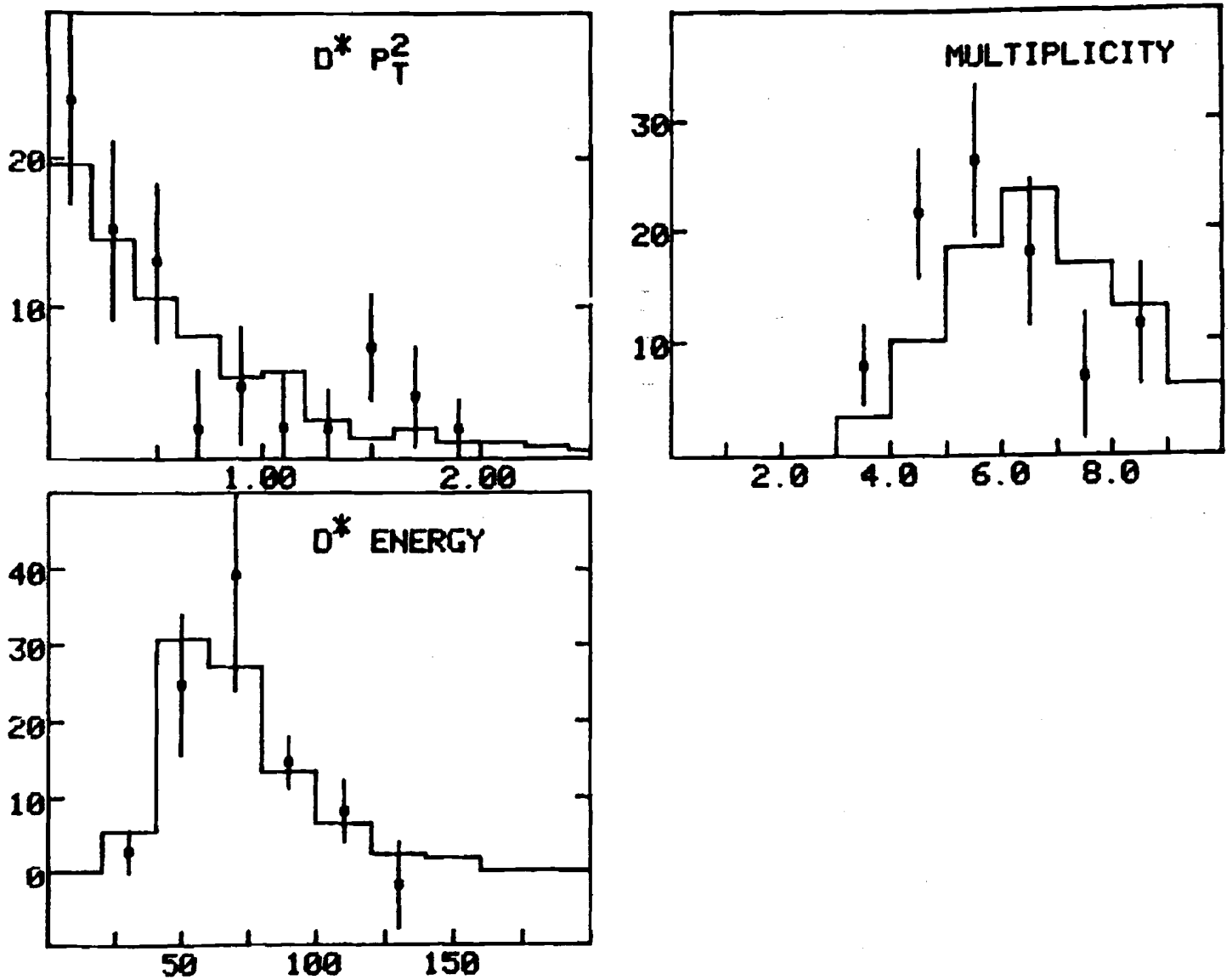

COMPARISON OF SIGNAL AND BACKGROUND INCLUSIVE DISTRIBUTIONS

Figure 7.14

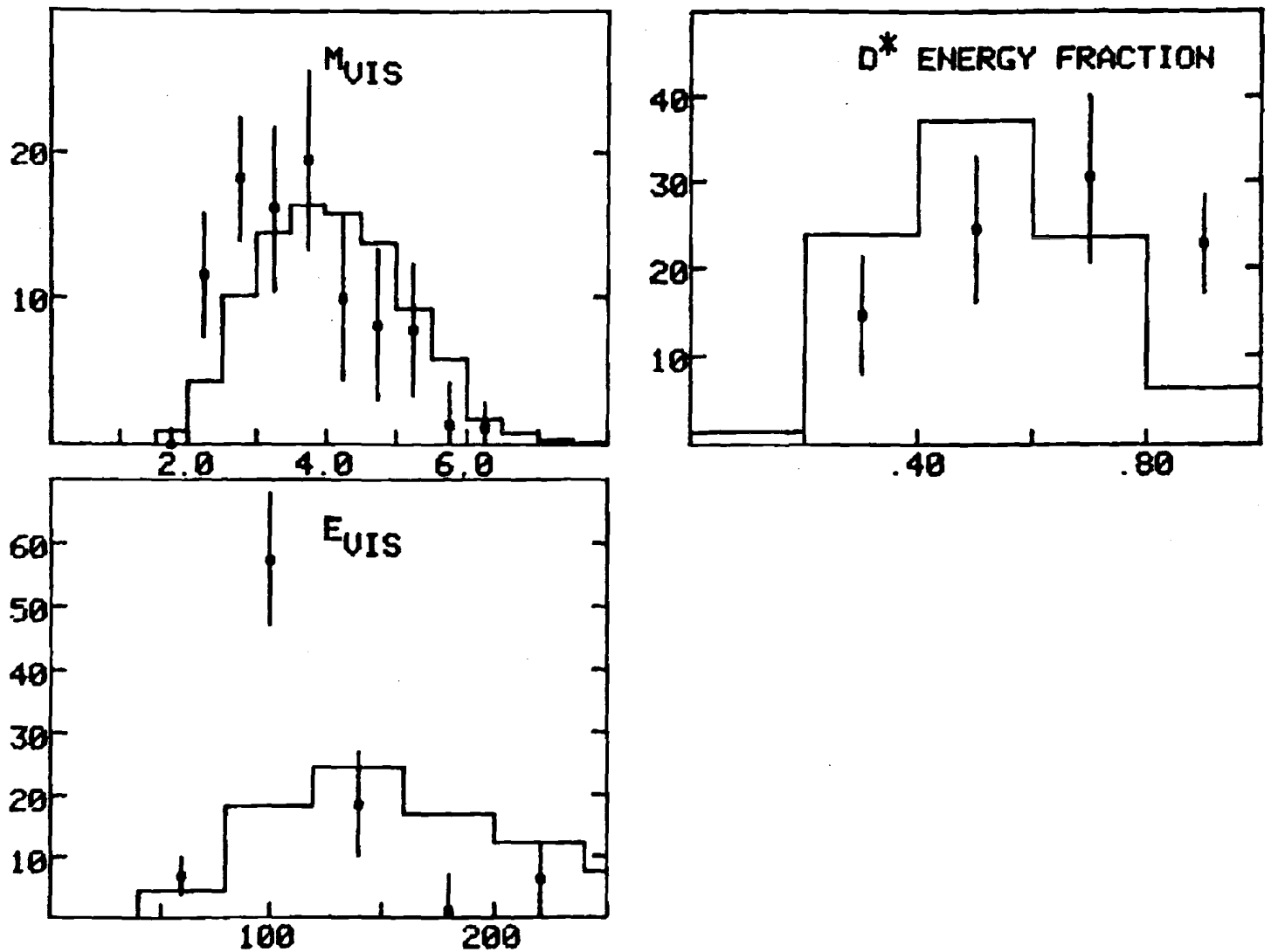

COMPARISON OF SIGNAL AND BACKGROUND INCLUSIVE DISTRIBUTIONS

Figure 7.15

Section D Total Photoproduced Charm Cross Section

The photon gluon fusion mechanism only makes predictions for total charm production, with values of 200-300 nb expected for the photon spectrum shown in fig. 2.2. We can ask how well this calculation agrees with the estimated level of charm production inferred from our data. Such an estimate turns out to be useful for another reason. It has been reported {51} that the total photon nucleon cross section into hadrons is about 2 to 6 μb larger than the value predicted on the basis of vector meson dominance arguments. The authors suggest that this apparent gap could be filled by charm production, which implies a charm production cross section about an order of magnitude larger than that predicted by the gluon fusion mechanism.

We begin by calculating the model dependent D* cross section using the gluon fusion mechanism. The average acceptance now becomes 5.58%, compared to 4.6% for the diffractive psion model used in chapter 6, and we can simply scale that cross section to obtain

$$\sigma(\gamma + N \rightarrow D^{*+}) = 132 \pm 60 \text{ nb}$$
$$\sigma(\gamma + N \rightarrow D^{0}) = 320 \pm 155 \text{ nb}$$

We can obtain an estimate for total charm production by making assumptions concerning isospin and the connection between charm production in e+e- annihilation and photoproduction. If isospin invariance is assumed to hold, then

$$\sigma(D^{+}D^{-}) = \sigma(D^{0}\bar{D}^{0})$$
$$\sigma(D^{*+}D^{*-}) = \sigma(D^{*0}\bar{D}^{*0})$$
$$\sigma(D^{*+}D^{-}) = \sigma(D^{*0}\bar{D}^{0})$$

The D:Λ_c:F ratio has been measured in e+e- annihilation to be very approximately 3:1:1 (The F production value used here is that obtained by the DASP group {11}, but might be too large in light of the fact that MARK II {12} has an upper limit for F production of only 1/2 of this cross section).

If we assume that charmed mesons fragment independently of production mechanism, then we can tie all unbound charm production in our experiment to the D cross section. The only uncertainty is the size of the D^+ cross section relative to the D^0.

The D^+/D^0 ratio can be estimated using the 3 cross section relations determined from isospin invariance. Using a wide range of weighting schemes to relate the DD, DD^*, and D^*D^* cross sections, we find that the D^+/D^0 ratio is typically .35-.60, which is similar to the average value estimated for this ratio in e+e- annihilation (center of mass energies 4 to 6 GeV) of .45 ± .23 {52}. The weighting schemes also predict the D^{*+}/D^0 ratio to be in the range .25-.60, which compares well with the $.40^{+.22}_{-.11}$ measured in our experiment.

If we choose D^+/D^0 = 1/2 as being representative of the charm cross section behavior, then we obtain an estimate of total charm photoproduction of

$$320(D^0)+160(D^+)+160(\Lambda_c)+160(F)+30(\psi)+30(\eta_c) = 860 \text{ nb}$$

where a small η_c contribution equal to that of the ψ has been included.

The apparent disagreement of this "experimental" cross section with the 200 to 300 nb predicted by the gluon fusion model should not be taken too seriously because higher order corrections to the skeleton diagrams of fig. 1.2(b) can easily modify these predictions by factors of 2 or so, although the direction of the change is not clear {53}. These corrections would presumably not alter the diffractive character of charm production. In addition, there is the possibility that the strong coupling constant α_s could be larger than the value .25 used in these calculations. Finally we note that applying the gluon fusion to hadroproduction, via the diagrams in fig. 1.1(b), underestimates the total charm cross section by an order of magnitude

{54}. All of these comments lead us to conclude that the theoretical situation vis à vis the gluon fusion mechanism remains fluid.

The total charmed cross section estimated here for our experiment appears to be far too small to account for the 2-6 μb gap between the measured and predicted (by VMD) total photon cross section.

CHAPTER 8

SUMMARY AND CONCLUSIONS

Using a high luminosity (602 evts/nb) high energy photon beam, we have observed the process $D^{*+} \rightarrow D^0\pi^+$, where $D^0 \rightarrow K^-\pi^+$ or $K_S\pi^+\pi^-$. As discussed in chapter 6, this observation depended crucially on the the small Q value of the $D^{*+} \rightarrow D^0\pi^+$ decay, which allows a very precise (1 MeV) determination of the D^{*+}-D^0 mass difference ΔM histogrammed in fig. 6.1. By plotting the $K\pi$ mass distribution subject to the very tight requirement $.1425 < \Delta M < .148$ GeV/c^2, we were able to reduce the combinatoric background from 11000 events/bin to about 60 events/bin, enough to uncover the D^0 peak shown in fig. 6.2(a). A fit of this distribution to a Gaussian signal plus exponentially falling background yielded a signal of 143 ± 20 events at a mass of 1.861 ± .002 GeV/c^2 with a width consistent with our resolution.

By imposing a multiplicity cut demanding 7 or fewer tracks, and a tight ΔM requirement of $.1445 < \Delta M < .1465$ GeV/c^2 we obtained the $K_S\pi^+\pi^-$ peak shown in fig. 6.2(b). This signal of 35±11 events was consistent in position and width with the $K\pi$ signal.

We eliminated the possibility that the D* signal could be produced by the hadron component of our beam by plotting the mass difference ΔM for data taken with 6 radiation lengths of lead in the beam (to eliminate photons). No signal was observed and it was found that almost all of the background in the vicinity of the mass difference peak could be attributed to this hadron contamination.

The strength of the D* signal can be used to determine a limit on possible D^0-$\bar{D}^0$ mixing. If the mixing is parameterized by the fraction of time A that a D^0 decays like a $\bar{D}^0$, then $A < .11$ at the 90% confidence level, which is similar to the .16 upper bound obtained by the MARK I group at

SPEAR {8}.

Various methods of attack were developed in chapter 6 for studying the D* production mechanism. Before discussing these, it is worthwhile to examine the data of the CERN WA4 group, who report {39} a D^0 signal in the $K^+\pi^-$ (but not the $K^-\pi^+$) mass distribution for incident photon energies between 40 and 70 GeV. They claim that their signal (fig. 8.1) is enhanced by requiring a same sign proton (ambiguous with a K in the momentum region covered by their Cerenkov counter) and obtain a cross section of approximately 500 nb/nucleon for inclusive D^0 production. To account for their effect, they argue for a production mechanism in which some sort of charm meson exchange takes place in the t channel to produce an anti-charmed meson and a relatively slow charmed baryon, which would then presumably decay to a final state containing a proton.

Our own data do not support such an interpretation in terms of "associated" production. Instead, we believe that we have accumulated strong evidence in favor of a mechanism in which the D* is diffractively produced against either a D or another D*. The following observations support this hypothesis. First, we observe almost equal production of D^{*+} and D^{*-} (61 ± 14 and 65 ± 15 events respectively). Second, 35 ± 9% of all D* production takes place with an oppositely charged K (opposite to the charge of the decay K) recoiling against the D*, whereas no signal is seen for events containing a same sign K or P. This observation, coupled with the first, strongly implies that a D or a D* is produced in association with the D*. Third, the average fraction of visible energy retained by the D* is approximately 1/2 (this is discussed in chapters 6 and 7), which is suggestive of a diffractive pair production mechanism. Fourth, we have presented evidence in chapter 6 that 45 ± 25% of all D* production takes

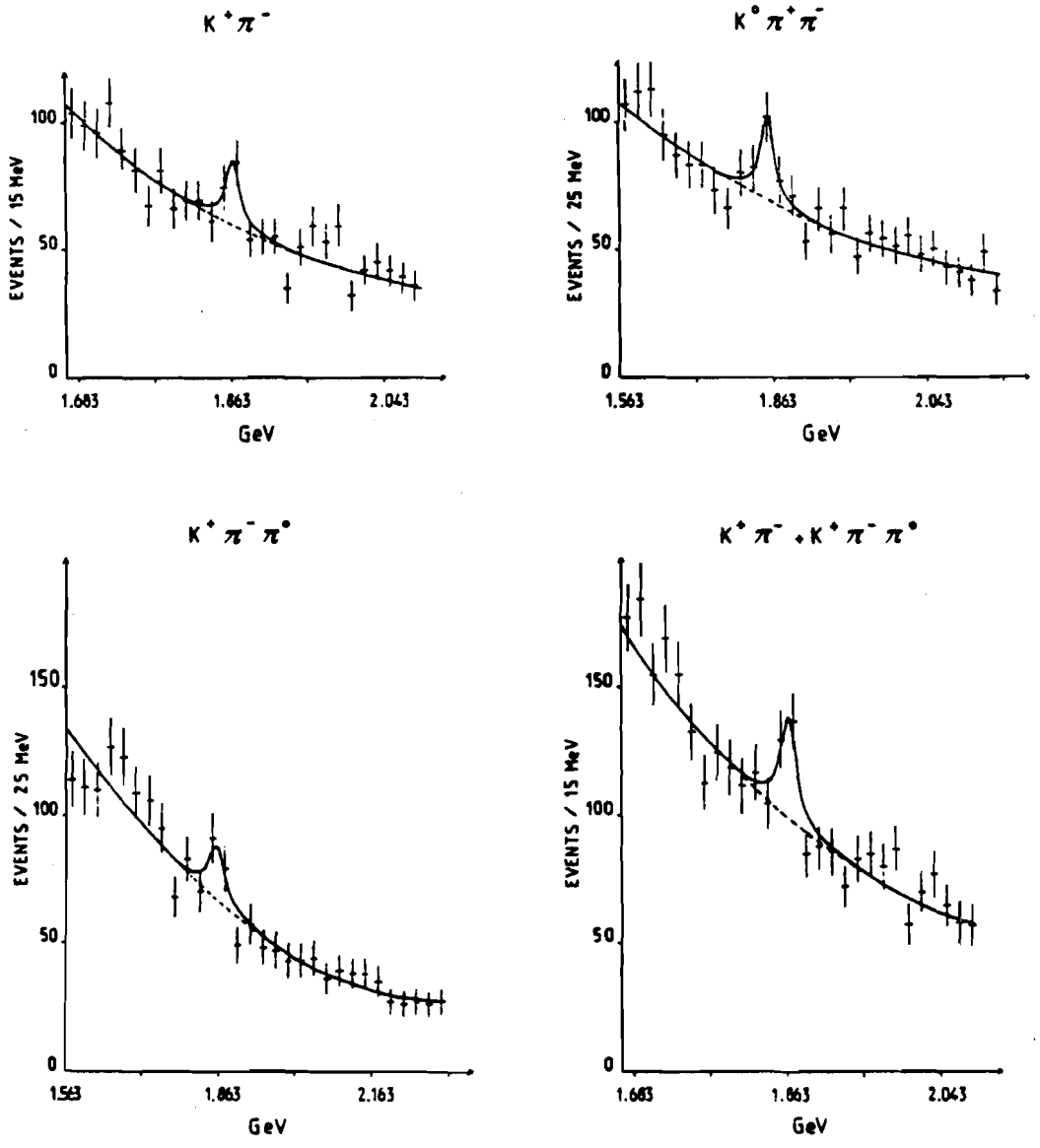

Signals obtained by the CERN WA4 group. These distributions require the presence of an additional K^+ (or P^+) in the event. The data argue for associated charmed baryon production.

Figure 8.1

place as $D^{*+}D^{*-}$. That analysis relied on the use of the second cascade pion to tag the D^{*-}.

Because the incident photon energies for the two experiments differ so much (40-70 GeV for WA4, 60-200 GeV for E-87A), it is possible to imagine a production mechanism in which associated baryon production and diffractive pair production would dominate in their respective energy regimes. This hypothesis seems very unlikely due to the fact that both experiments report signals for photon energies far above charm threshold. Further evidence against this interpretation can be obtained from the ψ photoproduction cross section, which reaches 63% of its asymptotic value by 50 GeV. This has a bearing on charm production since optical theorem and VMD arguments link the the ψ cross section with charm photoproduction in general.

Another handle on the recoil state is provided by the average recoil charged multiplicity of 2.31 ± .45 observed for the D* events. When corrected for acceptance, this becomes 2.91 ± .45, a multiplicity that is inconsistent by 1.7 standard deviations with 100% $D^{*+}D^{-}$ production (2.16 ± .16 predicted) but agrees with the 2.92 ± .22 expected from 100% $D^{*+}D^{*-}$ production.

The observed multiplicity rules out significant production of several extra pions with the D meson pair. However, if the incident photon is in a pure I=0 state, then any amount of single pion production can be accomodated because the cross section for $D^{*+}D^{0}\pi^{-}$ (mult. 3.46 ± .14) is forced to be twice that of $D^{*+}D^{-}\pi^{0}$ (mult. 2.16 ± .16), which allows the two processes to add compensating contributions to the recoil multiplicity in such a way as to maintain the observed multiplicity within the error bars of the measurement. A similar statement holds for the processes $D^{*+}D^{*-}\pi^{0}$ (mult. 2.92 ± .22) and $D^{*+}D^{*0}\pi^{-}$ (mult. 3.46 ± .14). This extra pion production might be needed to

explain the fact that 16 ± 5% of our observed D* events have charged recoil masses greater than the D* mass, even when the pion mass is assigned to each recoil particle. A Monte Carlo simulation shows that the process $D^{*+}D^{0}\pi^{-}$ can account at least qualitatively for the effect. We believe that possible factors such as stray muons produced upstream of our detector or fake tracks generated by the reconstruction program are just too small to account for the relatively large fraction of events with large recoil mass.

A diffractive pair production model (psion model) involving a massive parent decaying into $D^{*+}D^{*-}$ was used to estimate the D^{*+} production cross section. The mass dependence of the parent state was generated as M^{-7} in order to reproduce the observed D* transverse momentum behavior (fig. 7.3). The average acceptance was found to be 4.6%, which implies a D^{*+} production cross section of 160 ± 70 nb. The relative branching ratio of $D^{0} \dashrightarrow K_{S}\pi^{+}\pi^{-}$ to $D^{0} \dashrightarrow K^{-}\pi^{+}$ was determined to be 1.6 ± .7, which is bracketed by the LGW measurement of 1.8 ± .8 and the MARK II value of .9 ± .3 {40}.

A weak inclusive D^{0} signal was observed in the raw $K\pi$ mass distribution. The signal represents about a 3 standard deviation effect, containing 660 ± 230 events (FWHM fixed at .023 GeV/c^{2}) over a background of 30000 combinations. The cross section obtained from the 660 event sample was calculated to be 390 ± 190 nb, using the same kind of diffractive Monte Carlo as that employed for the D^{*+} cross section. The ratio of D^{*+} to D^{0} production then becomes $.40^{+.22}_{-.11}$.

The photon gluon fusion mechanism was discussed at length in chapters 1 and 7 because it offers an attractive theoretical interpretation of charm photoproduction, in contrast to the ad hoc "psion" model described above and in chapter 6. The model appears to describe the ψ photoproduction excitation curve rather well {32} in spite of crude assumptions regarding the fraction

of bound charm cross section tied up with ψ production. We obtained good agreement with all inclusive measurements of D* photoproduction, once certain modifications were incorporated to bring the model more into line with experimental data.

In particular, we found that the fragmentation function $D(z)=\delta(z-1)$, where the D^* takes off all of the charmed quark energy, is not consistent with the D* P distribution, especially if realistic gluon transverse momentum {50} is included. However, the P_t distribution can be reproduced by using smooth fragmentation distributions, of the type measured in neutrino and e+e- data {45,46,49}, but only if the gluon transverse momentum inferred from dilepton data {50} (.7-1. Gev/c) is also added.

The diffractive energy dependence found for the D* data was used in chapter 7 to rule out sizeable contributions from either the Drell Yan-like mechanism of fig. 1.2(a), which predicts slow moving charm, or the Halzen-Scott diagram in fig. 1.2(c), which predicts one slow and one fast charmed particle. The energy behavior is, however, in complete accord with that expected from the gluon fusion mechanism, as seen in fig. 7.11.

It is possible to make a rough estimate of total photon induced charm production using the values of D* and D^0 production observed in our experiment. If charm is produced from the I=0 part of the photon, and we take over the 3:1:1 relative ratio of $D:\Lambda_c:F$ as seen in e+e- annihilation, then we obtain a crude estimate of the total photon induced charm cross section of approximately 860 nb, averaged over our photon spectrum.

This estimate is about a factor 2-3 larger than the 200-300 nb expected from gluon fusion, but uncertainties in the model are expected to be large enough to cover this discrepancy {53}. However, the cross section appears to be too small to account for the 2-6 μb "gap" between the measured and

predicted (by VMD) total photon cross section {51}. It has been tempting in the past to ascribe this extra cross section to charm production.

The Future

Although we have conclusively shown that D^{*+} mesons are created by photons via some sort of diffractive pair production mechanism, further experiments need to be performed in order to understand the underlying dynamics of such a model. Tagged photon experiments would be especially useful because, as we saw in chapter 6, a relatively background free D^* signal could be obtained by exploiting the small D^{*+}-D^0 mass difference to identify events containing charm. In addition, the energy range of current tagged photon experiments lies in the range 30-80 GeV, which would allow a measurement of the energy dependence of the charm cross section in a region where this cross section is expected to be varying most rapidly. The shape of this excitation curve would also provide a test of the photon gluon fusion model and allow a determination of the gluon distribution within the nucleon. It is easy to think of other topics that require study. These include: (1) the ratio of D^{*+} to D^0 and D^{*0} to D^{*+} production; (2) the fraction of events that are produced with extra pions; (3) what fraction of events are produced as DD, DD^*, or D^*D^*; (4) the correlation in spin between the two D^* mesons; and (5) the mass dependence of the parent decaying into the final state charmed mesons.

Unfortunately, matters are not as straightforward as indicated above because tagged beams in general have intensities about a factor of ten lower than our broad band beam. This requires the use of long running periods and good acceptance to acquire the statistics necessary to study the production mechanism in sufficient detail to improve our understanding of

charm production. Given the rapid rate of technological progress in High Energy physics, such high intensities should be within reach in a few years.

References

1. J.D. Bjorken and S.L. Glashow , Phys. Lett. 11,255(1964)

2. A. Benvenuti et al, Phys. Rev. Lett. 32,800(1974)

3. S.L. Glashow, J. Illiopoulos, and L. Maiani, Phys. Rev. D2,1285(1970)

4. J.E. Augustin et al, Phys. Rev. Lett. 33,1406(1974)

5. J.J. Aubert et al, Phys. Rev. Lett. 33,1404(1974)

6. G. Goldhaber et al, Phys. Rev. Lett. 37,255(1976)

7. J.E. Wiss, Ph.D thesis, University of California, Berkeley (1977)

8. G. Feldman et al, Phys. Rev. Lett. 38,1313(1977)

9. E.D. Bloom, Talk given in Proceedings of the 1979 International Symposium on Lepton and Photon Interactions at High Energies, FNAL (1979)

10. E.D. Bloom, talk given in Proceedings of the Sixth International Conference on Experimental Meson Spectroscopy, Brookhaven, N.Y., 1980

11. R. Brandelik et al, Phys. Lett. 80B,412(1979)

12. V. Luth, talk given at FNAL conference, p.78, 1979 (ref.9)

13. F. Richard, talk given at FNAL conference, p.469, 1979 (ref.9)

14. B. Knapp et al, Phys. Rev. Lett. 37,882(1976)

15. D. Drijard et al, Phys. Lett. 85B,452(1979)

16. W. Lockman et al, Phys. Lett. 85B,443(1979)

17. K. Giboni at al, Phys. Lett. 85B,437(1979)

18. G.S. Abrams et al, Phys. Rev. Lett. 44,10(1980)

19. J.J. Russell, Ph.D thesis, University of Illinois, 1980

20. A. DeRujula, H.Georgi, and S.L. Glashow, Phys. Rev. D12,147(1975)

21. S.D. Drell and T.-M. Yan, Phys. Rev. Lett. 25,316(1970)

22. M.B. Einhorn and S.D. Ellis, Phys. Rev. D10,2007(1975)

23. D.H. Perkins, in Proceedings of the Fifth Hawaii Topical Conference on Particle Physics, Honolulu, Hawaii, 1973 (University of Hawaii Press, Honolulu, Hawaii, 1974)

24. G. Farrar, Nuc. Phys. B77,429(1974)

25. A.J. Buras and K.J.F. Gaemers, Nuc. Phys. B132,249(1978)

26. M. Gluck, J.F. Owens, and E. Reya, Phys. Rev. D17,2324(1978)

27. C.E. Carlson and R. Suaya, Phys. Rev. D14,3115(1976)
Phys. Rev. D15,1416(1977)
Phys. Rev. Lett. 39,908(1977)
Phys. Lett. 81B,329(1979)

28. C. Kourkomelis et al, Phys. Lett. 81B,405(1979)
A.G. Clark et al, Nuc. Phys. B162,29(1978)
T.B.W. Kirk et al, Phys. Rev. Lett. 42,619(1979)
Y. Lemoigne et al, talk given at FNAL conference, p.524, 1979 (ref.9)

29. H. Wachsmuth, talk given at FNAL Conference, p.541, 1979 (ref.9)

30. H. Fritzsch and K.-H. Streng , Phys. Lett. 72B,385(1978)

31. L.M. Jones and H.W. Wyld, Phys. Rev. D10,759(1978)

32. T. Weiler, Phys. Rev. Lett. 44,304(1980)

33. F. Halzen and D.M. Scott, Phys. Lett. 72B,404(1978)

34. M.C. Goodman, Ph.D thesis, University of Illinois, 1979

35. M.S. Atiya, Ph.D thesis, Columbia University, 1980

36. W. Wisniewski, Ph.D thesis, Columbia University, 1980

37. R. Egloff, Ph.D Thesis, University of Toronto, 1978

38. M.K. Gaillard, B. Lee, and J. Rosner, Rev. Mod. Phys. 47,277(1975)

39. D. Aston et al, Submitted to Phys. Lett. (1980)

40. J. Kirkby, talk given at FNAL Conference, p. 107, 1979 (ref.9)

41. M. Suzuki, Phys. Rev. Lett. 37,1164(1976)

42. C. Quigg and J. Rosner, Phys. Rev. D17,239(1978)

43. A.R. Clark et al, Phys. Rev. Lett. 43,187(1979)

44. M. Suzuki, Phys. Lett. 68B,164(1977)
J.D. Bjorken, Phys. Rev. D17,171(1978)

45. V. Barger, T. Gottschalk, and R.J.N. Phillips, Phys. Lett. 70B,51(1977)

46. R. Odorico and V. Roberto, Nuc. Phys. B136,333(1977)

47. M. Holder et al, Phys. Lett. 69B,377(1977)

48. C. Baltay et al, Phys. Rev. Lett. 39,62(1977)

49. G. Feldman, in Proceedings of the Nineteenth International Conference on High Energy Physics, Tokyo, 1978 (p. 777)

50. J.E. Pilcher, talk given at FNAL conference, p. 185, 1979 (ref.9)

51. T. Nash et al, Phys. Rev. Lett. 40,1222(1978)

52. P. Rapidis, Ph.D Thesis, Stanford University, 1978

53. L.M. Jones, private communication

54. L.M. Jones and H.W. Wyld, Ill-(TH)-77-32 (1979) (Unpublished)

VITA

Paul Avery was born in 1951 in Ithaca, N.Y.. He attended West Seneca High School in Buffalo, N.Y., graduating in 1969 with only a rudimentary knowledge of what was to befall him. He received his B.S. in Physics from Canisius College in 1973, having attained some measure of fame as a weightlifter during his stay there. Moving on to the University of Illinois for graduate school, he received his M.S. in Physics in 1975 and held several teaching and research appointments in the Physics department. The rest, of course, is history.